Bistatic Synthetic Aperture Radar Imaging Using Fourier Methods

Gavin Halcrow

A thesis submitted for the degree of Doctor of Philosophy.
The University of Edinburgh.
January 2009

Abstract

Fourier imaging provides a method of forming synthetic aperture radar (SAR) images from collected radar data which does not demand the same computational load associated with other imaging methods such as matched filtering (MF) and convolution-back projection (CBP), due to use of the fast Fourier transform (FFT). In particular the polar format algorithm (PFA) provides a simple framework for image formation for spotlight SAR, limited however by the plane wave approximation.

This thesis presents the results of applying mapping methods to allow Fourier imaging using the PFA from irregularly sampled data sets. For example data collected from manoeuvring platforms, bistatic SAR and nonlinear 3D flight paths used to generate 3D SAR imagery.

Three different methods for nonlinear mapping of k-space samples to a uniform rectangular grid in a domain where the 2D irregular to regular resampling required by the PFA becomes separable in two dimensions and allows the use of the same interpolation filter for all data samples, are presented along with a comparison of their performance.

Image formation from nonplanar data surfaces typical of data collected from nonlinear curved 3D flight paths is examined. Scene reconstruction from this type of data has been discussed in the literature, however the algorithms used are computationally intensive. This thesis presents a 3D scene reconstruction method using Fourier imaging techniques.

The 3D Fourier reconstruction is a more complicated problem than the 2D case. The 3D case can be characterised by two distinct problems, the resampling from irregular to regularly spaced samples as in the 2D case, and additionally resampling to points off the data surface.

A 3D equivalent to the PFA is developed, where the resampling process is a 3D application of one of the methods developed for the 2D mapping method study, using results from a 2D simulation capturing the extra feature of the nonplanar data.

Simulated results using this method are compared to results obtained from the same data using a simple nearest neighbour based interpolation approach. Simulation results show that Fourier imaging methods can provide a less computationally intensive alternative for 3D SAR scene reconstruction than the methods discussed in the literature.

Declaration of originality

I hereby declare that the research recorded in this thesis and the thesis itself was composed and originated entirely by myself in the Department of Electronics and Electrical Engineering at The University of Edinburgh.

With the following exceptions:

- Figures 2.11 and 2.11 are adapted from [1].
- Figures 2.14 and 2.15 are from [2].
- Figures 2.17, 2.18 and 2.19 are adapted from [3].
- Figure 2.23 is from [1].
- Figure 2.25 is from [4].

Acknowledgements

I would like to thank Prof. Bernard Mulgrew for all his advice, guidance and academic support during the course of this work, and Dr. Dave Laurenson for his feedback in his role of second supervisor.

I would also like to thank the engineering and physical sciences research council (EPSRC), BAE Systems and SELEX Sensors and Airborne Systems Ltd for funding this research. In addition I would also like to thank Mike Lowe, Iain Scott, Peter Fielding and Jim McBride for their constructive criticism and practical guidance at timely intervals throughout the duration of the project, and Iain McColl, Dave Greig and Neville Ramsey for their continued support while completing this thesis.

I am grateful to Chin Heng Lim, Amit Kumar Mishra, Georgos Kavaritis, Elias Aboutanios, Sharad Nagappa and Nick Johnson for making the lab a more friendly and relaxed place to work and for all the little bits of help they've provided over time.

And lastly thanks to my family and friends for all their encouragement and for politely listening to me talk about this work for more than 3 years

Contents

List of figures

List of tables

Acronyms and abbreviations

1D	one dimensional
2D	two dimensional
3D	three dimensional
ATR	automatic target recognition
CBP	convolution back-projection
CW	continuous wave
CSA	chirp scaling algorithm
CSAR	curvilinear SAR
dB	decibells
ECM	electronic counter measures
EM	electro-magnetic
FT	Fourier transform
FFT	fast Fourier transform
FT	Fourier Transform
ICA	independent component analysis
IDF	image display frame
IFT	inverse Fourier transform
IFFT	inverse fast Fourier transform
IFT	inverse Fourier Transform
IFP	image formation processor
IFSAR	interferometric SAR
ISAR	inverse synthetic aperture radar
LFM	linear frequency modulated
LOS	line of sight
MF	matched filtering
MLE	maximum likelihood estimator
MTRC	motion through range cells
PCA	principle component analysis
PFA	polar format algorithm

PGA	phase gradient autofocus
PRF	pulse repetition frequency
PRI	pulse repetition interval
radar	radio detection and ranging
RCS	radar cross section
RFA	rectangular format algorithm
RMA	range migration algorithm
rms error	root mean square error
RVP	residual video phase
SAR	synthetic aperture radar
SNR	signal to noise ratio
UAV	unmanned aerial vehicle

Nomenclature

β	bistatic angle
δ_r	resolution in the range direction
δ_{cr}	resolution in the cross-range direction
δ_{vcr}	resolution in the vertical cross-range direction
$\delta(t)$	Dirac delta function
δ_x	resolution in the x direction
δ_y	resolution in the y direction
δ_z	resolution in the z direction
Δt	sample spacing
Δx	sample spacing of polar region in k-space in k_x direction
ΔX	extent of polar region in k-space in k_x direction
Δy	sample spacing of polar region in k-space in k_y direction
ΔY	extent of polar region in k-space in k_y direction
Δz	sample spacing of polar region in k-space in k_z direction
ΔZ	extent of polar region in k-space in k_z direction
$\mathbf{\Lambda}$	PCA stretch component
$\mathbf{V}$	PCA rotate/reflect component
ω	frequency
ω_1	start of radar bandwidth
ω_2	end of radar bandwidth
ω_j	frequency of *j*th sample
ω_{bp}	filter band pass edge
θ	bistatic look angle
θ_i	apparent look angle of *i*th pulse
μ	chirp rate
λ	radar wavelength
σ	complex reflectivity coefficient
ϕ	signal phase
ϕ_{MF}	matched filter phase

ϕ_ϵ	phase error function
$\hat{\phi}_\epsilon$	estimated phase error function
$\Delta\phi_\epsilon$	gradient of phase error
ψ	slant angle
$\Delta\psi$	variation in slant angle
a	Volterra mapping coefficient
$\mathbf{a}$	matrix of Volterra mapping coefficients
A	amplitude
A_t	transmitted amplitude
A_0	reference amplitude
$\mathbf{A}$	matrix of known sample values
$\mathbf{a}_t$	transmit platform acceleration
$\mathbf{a}_r$	receive platform acceleration
B	bandwidth
B_{3dB}	3dB beamwidth
B_{SAR}	synthetic aperture beamwidth
c	speed of light
$\mathbf{C}$	covariance
C_{fft}	computational cost of a power of 2 FFT
C_p	computational cost of interpolation
D	scene size
D_x	scene size in the x direction
D_y	scene size in the y direction
D_z	scene size in the z direction
DSR	down sample rate
E_t	energy transmitted
$f(\mathbf{k})$	a function of the k-space vector
$f^{-1}(\mathbf{k})$	inverse of function of the k-space vector
$\mathbf{f}()$	nonlinear mapping function
f_c	radar centre frequency
f_{max}	maximum frequency
f_s	sample frequency
$g(r,\psi)$	CBP reconstructed image of g(x,y) at polar coordinates in the (x,y) plane

$g(x, y)$	complex reflectivity function of the scene of interest
$G(\omega, \theta)$	2D FT of g(x,y) on polar coordinates in slant plane
G	filter gain term
$h(n)$	space invariant blurring function
i	pulse number
i_{new}	noninteger pulse number
j	sample number
J	least squares cost function
$\mathbf{k}$	k-space vector
$\mathbf{k}_i$	k-space vector for the *i*th pulse
k_r	component of the k-space vector in the range direction
k_x	x-component of the k-space vector
k_y	y-component of the k-space vector
k_z	z-component of the k-space vector
k_{xi}	k_x coordinate of *i*th sample
k_{yi}	k_y coordinate of *i*th sample
$\mathbf{k}^{'}$	mapped k-space vector
$\mathbf{k}'_{affine}$	affine mapped k-space vector
$\mathbf{k}_i^{'}$	mapped k-space vector of the *i*th pulse
$\mathbf{k}_x^{'}$	x-component of the k-space vector
$\mathbf{k}_{ij}^{'}$	k-space location of the *j*th sample on the *i*th pulse
$\mathbf{K}$	matrix of Volterra series terms
$\mathbf{K'}_x$	matrix of known k_x coordinates of samples in mapped k-space
$\mathbf{K'}_y$	matrix of known k_y coordinates of samples in mapped k-space
l_0	round trip distance from transmitter via scatterer to receiver
l_1	round trip distance from transmitter via scene centre to receiver
l_s	round trip distance from transmitter via line through scene centre to receiver
$L_{antenna}$	length of radar antenna
L_f	length of interpolation function
L_{SAR}	length of synthetic aperture
L_x	length of synthetic aperture in the x direction
L_z	length of synthetic aperture in the z direction
$L_{x,y}$	resolution cell at (x,y) of scene of interest g(x,y)

$\mathbf{m}$	mean
M	number of samples per pulse
M_d	number of desired samples
N	number of pulses
N_d	number of desired pulses
N_p	number of pulses
N_s	number of samples
N_{stored}	number of samples stored
O_x, y	output image pixel at x,y coordinate
P	power
$P_\theta(\omega)$	slice through 2D FT of the scene at angle θ
PRI	pulse repetition interval
$Q(t)$	filtered projection of pulse
$\mathbf{r}_n$	position of nth scatterer in scene
r_{0t}	range to transmit platform
r_{0r}	range to receive platform
r_t	range from transmitter to scatterer
r_r	range from receiver to scatterer
r_{st}	range to line through scene centre from transmitter
r_{sr}	range to line through scene centre from receiver
R_0	range to scene centre
R_{over}	over-sampling rate
rect()	rect function
s_{tx}	transmitted signal
s_{rx}	received signal
s_{sc}	dechirp reference signal delay to scene centre
s_{line}	dechirp reference signal delayed to a line through scene centre
$s_{dechirp}$	dechirped signal
s_{RVP}	RVP compensation term
s	dechirped RVP compensated received signal
s_ϵ	image domain data including phase error function
$\bar{s}_c$	corrected frequency domain data
t	(slow) time

$\hat{t}$	fast-time
T_p	pulse width
$\mathbf{u}$	bistatic look direction vector
$\hat{\mathbf{u}}$	unit vector in the direction of $\mathbf{u}$
$\mathbf{u}_x$	x component of bistatic look direction vector
$\mathbf{u}_y$	y component of bistatic look direction vector
$\hat{\mathbf{u}}_t$	unit vector in the direction of transmit platform
$\hat{\mathbf{u}}_r$	unit vector in the direction of receive platform
$\mathbf{v}_t$	transmit platform velocity
$\mathbf{v}_r$	receive platform velocity
$\mathbf{x}_t$	transmit platform position
$\mathbf{x}_{t0}$	transmit platform initial position
$\mathbf{x}_{tnew}$	position of the transmit platform for noninteger pulse number
$\mathbf{x}_r$	receive platform position
$\mathbf{x}_s$	position of scatterer within scene
$\mathbf{x}_{r0}$	receive platform initial position
$\mathbf{x}_{ac}$	aperture centre position
$\mathbf{X}$	matrix of sample spacings in the x direction
$\mathbf{Y}$	matrix of sample spacings in the y direction
$\mathbf{Z}$	matrix of interpolated desired sample values

Chapter 1
Introduction

Ever since the discovery of radio detection and ranging (radar) in 1935 by Sir Robert Watson-Watt and its successful use during the second world war for detection of incoming enemy aircraft, following the invention of the cavity magnetron, radar systems have been used for a wide variety of purposes and in many different operational modes. These modes include topographic mapping of planet surfaces, assisted aircraft landing, targeting, reconnaissance imaging, terrain classification and oceanography [5, 6].

Radar has many advantages over similar optical techniques since radar can be used to form images at night, in adverse weather conditions, through foliage and is often used in subterranean imaging. All of these applications/conditions are unsuitable for optical imaging systems.

Early radar systems worked in a bistatic mode of operation, typically with the transmitting and receiving antenna being located in separate fixed position ground based radar placements, this was the model for the chain home defence system used during the second world war. However in the 1950s improving radar technology meant that it was feasible for the transmitter and receiver to be co-located (using the same antenna) with obvious financial benefits, operating in a monostatic mode. As a result monostatic radar algorithms are well established and account for a significant proportion of the radar literature [5].

In conventional radar modes the ability to resolve a target, that is to be able to identify two closely spaced targets as separate, scales with radar antenna size. Therefore to be able to resolve two targets separated in azimuth by one metre in a conventional radar mode would require a radar antenna much larger than can be mounted on a single pilot aircraft [7]. Signal processing techniques can be used to gain high resolution using a suitably sized radar antenna by synthesising a large antenna, this is termed synthetic aperture radar (SAR). Where many radar pulses are emitted and the returns from a scene of interest are collected as the aircraft flies along its path. Using such a scheme the achievable azimuth resolution can be shown to be dependent on the period of time over which the radar returns are collected, and not purely based on the physical size of the antenna used [1, 7].

1.1 Motivation

There has been an increase in interest in bistatic radar systems in recent years. There are many reasons behind this renewed interest in the bistatic mode of operation: developments in unmanned aerial vehicles (UAVs) have lead to interest in pairing a cheap receiving antenna on a UAV with a more expensive transmitting antenna which could be located at a safe distance further away from any enemy. Stealth aircraft are designed to minimise the radar returns in the direction of incoming radar energy in an effort to reduce the aircraft's radar cross section (RCS) limiting the enemy's ability to spot or target the aircraft, however some of the incoming energy is still reflected in other directions, this means it is feasible that a bistatic radar system may be able to provide a counter stealth capability. However the increased survivability of the receiving platform due to operating in a passive receive only mode is a primary reason for the increase in bistatic radar research [8–10].

The monostatic mode of operation is in fact a subset of the bistatic mode. This fact has been used to demonstrate the applicability of many SAR image formation algorithms developed for monostatic operation in the bistatic case [11–14]. However since the bistatic geometry is a more general case of the monostatic geometry it provides (in general) a more complicated problem to solve. With this increased generality of problem and desirable increase in radar platform survivability in mind, bistatic SAR provides a relevant and interesting series of problems to be investigated.

One of the particular features of most SAR image formation algorithms is the assumption that the radar platform flies along a straight and level flight path while transmitting and receiving pulses [1,2,7]. This inflexible data collection geometry reduces the radar platform survivability, therefore investigating which bistatic SAR algorithms are amenable to data collection whilst the radar platform manoeuvres is pertinent. In particular Fourier based imaging algorithms provide a computationally efficient method for SAR image formation, so a study of methods allowing Fourier imaging techniques to be applied to a wider range of scenarios than previously considered provides the motivation for the research presented in this thesis.

1.2 Contribution to knowledge

Motivated by the issues discussed in the previous section research in this area was undertaken. The major contributions arising from the result of this research are discussed in this section.

Three methods for performing a nonlinear mapping of SAR sample points in k-space into another domain where these points form a regularly sampled rectangular grid are developed. These methods are: Volterra series based mapping, analytic mapping and semi-analytic mapping. This mapping is performed so that the 2D resampling operation which forms the core of the polar format algorithm (PFA) can be viewed as two separable 1D resampling operations in this new domain. The mapping methods developed have been applied to simulated bistatic SAR data and their performance in terms of mapping accuracy and computational complexity has been analysed and compared to the standard keystone resampling method by means of a mathematical simulation of the bistatic SAR scenario which was implemented in MATLAB. This forms the first contribution of the work presented in this thesis along with the analysis of the performance of both the aforementioned techniques for a bistatic SAR scenario with a manoeuvring receive platform.

The second contribution of the research presented in this thesis is the development of a computationally efficient method of forming 3D SAR images using Fourier techniques, operating on data collected from a platform flying a curved 3D flight path. This development consists of two main stages, firstly characterising the problem with the nonplanar 2D data collection surface which is the result of the chosen flight path and demonstrating that it is possible to form an image from this type of data. This stage is performed via a simple simulated 2D problem which has the same properties as the more complex 3D case, results from this 2D demonstrator are presented for three cases: an orthogonal data set, a complete circular data set and a curved arc with a limited angular extent. The complete 3D image formation algorithm is an extension of one of the 2D mapping methods developed for the PFA.

1.3 Thesis organisation

The thesis is organised in the following way:

Chapter 2 details the necessary background theory relevant to understanding the rest of the work contained in the thesis and the result of the literature study performed at the start of the research.

Firstly focusing on the main SAR modes of operation and detailing the most prominent image formation algorithms in the open literature. Then consideration is given to what changes for a manoeuvring radar platform and what advantages/disadvantages can be expected. The last part of this chapter deals with how to retain the full 3D content of the imaged scene using methods such as interferometric SAR (IFSAR).

Chapter 3 describes the work performed on applying mapping concepts to the interpolation process required by the PFA. The theory of each of the three methods developed is presented along with results detailing the performance of the methods. Consideration is given to how the interpolation should be performed when the mapping is complete. The result of simulating the mapping and interpolation method developed for a variety of manoeuvring bistatic SAR scenarios is presented. Lastly the simulated results of applying the mapping and interpolation method to data collected with a manoeuvring bistatic receive platform are compared to the performance achieved using the keystone method.

Chapter 4 details the important differences between the 2D and 3D imaging modes and characterises the problem of 3D image formation from data collected from a curved 3D flight path. Image formation from this type of data is demonstrated using a simple 2D illustrative simulation. One of the mapping methods described in the previous chapter is extended to cover this 3D case and used to implement a 3D version of the PFA capable of resolving scatterers in 3D.

Chapter 5 summarises the work that has been presented and details the conclusions that can be drawn, along with a discussion of future work that could continue research in this area.

Chapter 2
Background Theory and Literature Review

This chapter covers the necessary principles and radar signal processing theory required to understand the work presented in this thesis, along with a review of the most important work performed within the radar research community in the area of synthetic aperture radar (SAR) image formation processing algorithms. This serves two purposes, firstly to give the reader suitable grounding to understand the radar signal processing described in the rest of this thesis and secondly to place the contribution of the work presented in this thesis in context. The first section of this chapter will present the background of radar and 'the basics' of radar signal processing including what type of waveforms are typically used and why. The second section will consider SAR and details some of the most common modes of operation along with discussion of the relative merits of each. Next the geometry of the bistatic SAR system is described along with a mathematical signal model used throughout this thesis. Then the most prevalent image formation processors (IFPs) in the open literature are presented and a basic introduction to the interpolation and resampling operations that are necessary for practical sampled data signal processing is given. Lastly the advantages that are offered when a manoeuvring radar platform is introduced, particularly with the intention of forming a 3D SAR image, are discussed and the main methods in the open literature are presented.

2.1 Background

Christian Hulsmeyer was the first person to demonstrate the use of radio waves to detect distant objects. In 1904 he received patents in both the UK and Germany for the telemobiloscope, a primitive ship based radar system that was designed to detect other ships in dense fog to aid with collision avoidance. The simple device used a multipole antenna to transmit electromagnetic (EM) radiation and when the small reflected signal was received at a separate antenna a bell would ring to indicate the presence of the other ship, the telemobiloscope was demonstrated to detect ships at a range of 3 km. However this invention was not a commercial success due to

a general lack of interest from the naval industry and hence is not often recognised as the first radar system, instead this is usually reserved for Robert Watson-Watt [6].

During the second world war the British air ministry asked Watson-Watt to develop a 'death-ray' in response to rumour that the Germans had developed such a weapon. Watson-Watt concluded that the power necessary to operate a 'death-ray' was prohibitive, however in the course of his experiments he noted that a small amount of energy was reflected from the target and could be collected to indicate the presence of a target. This concept was demonstrated in the Daventry experiment in 1935 where a bomber aircraft was detected at 8 miles range using the BBC Daventry shortwave radio transmitter [5, 15].

The Chain home radar early warning system was built using similar technology and was completed in time for the battle of Britain and was key to enabling the limited forces of the royal air force to be deployed effectively to repell German long range bombers. The Chain home system was a series of 100 m tall steel towers with antenna suspended from wires between the towers, the receiving antenna were mounted on smaller wooden towers. A single Chain home station consisted of two tall steel towers and a single smaller wooden tower. A Chain home station was capable of detecting bomber aircraft out to a range of 120 miles and used 12 m wavelength radiowaves around 20 MHz [6].

During the course of the second world war it was clear that radar was a very important part of a modern airforce and air defence system. The physics behind the radar signal detection were well understood and the need to develop longer range systems required waveforms in the 10 cm wavelength or 3 GHz range. With this in mind German scientists were reluctant to further develop the resonant-cavity magnetron as a method for generating the large amounts of power for transmitted waveforms, due to the lack of coherence of the output, instead preferring the lower power klystron for its favourable coherence properties. However British scientists worked round the problem by sampling the transmitted waveform and used this to synchronise the receiver, this approach allowed British aircraft to outclass German fighter planes in night time conditions [6].

The importance of radar during the course of the battle of Britain has lead to radar continuing to be a prominent sensor system in all manor of airborne applications. Modern radar systems are used in many diverse fields including meteorology where radar systems are used to detect and classify cloud formations, geology where ground penetrating and ground mapping radar systems are used, military uses include fire control radars and battlefield surveillance and there

is an increasing interest in ultra-wideband radar systems for through-wall detection systems [5].

2.1.1 Resolution

The basic principle behind radar is that measuring the time of flight, that is the total time taken for transmitted EM radiation to reflect off a surface and return to be collected by a receiving antenna, provides the range from the transmitter/receiver to the reflecting object or scatterer. The transmission of the EM energy is typically pulsed so that returns from several reflecting surfaces along the direction of transmission can be detected. However should two reflecting surfaces be sufficiently close so that the length of the transmitted pulse is greater than the difference in the time of flight between the two reflectors, the energy will return to the receiver as a stretched pulse rather than as two discrete pulses, therefore the receiver is unable to resolve the two reflectors. Resolution is a measure of the ability of a radar system to distinguish two closely spaced reflectors [16].

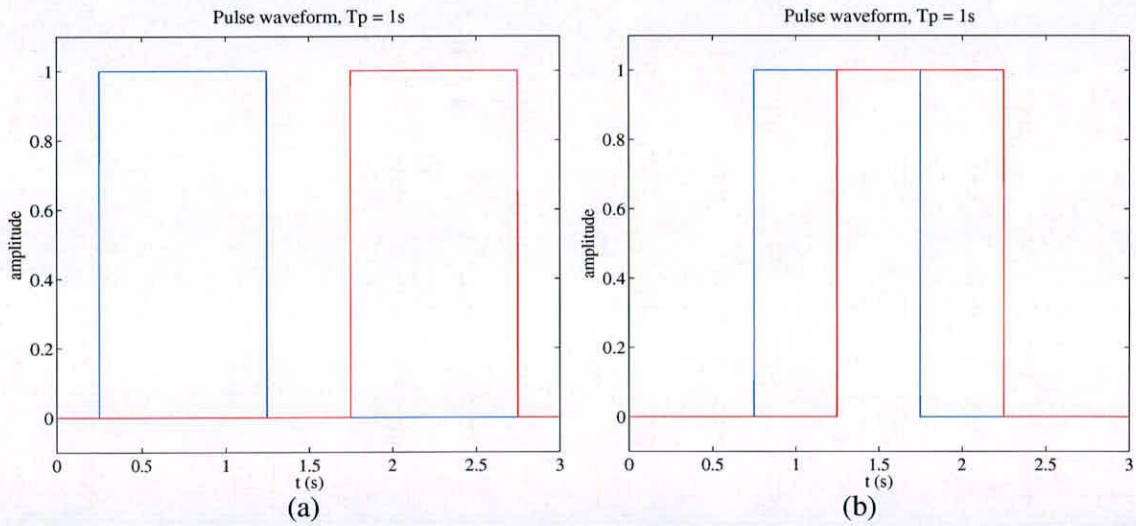

Figure 2.1: *Return pulses from closely spaced scatterers. (a) resolvable scatterers. (b) unresolvable scatterers.*

To improve the resolution of the system a narrower pulse width allows reflectors or targets to be closer together while still resulting in discrete pulses at the receiver.

$$\delta_r = \frac{cT_p}{2} \tag{2.1}$$

where δ_r is the resolution in the range direction and T_p is the pulse length. However this narrowing of the transmitted pulse has a practical limit and cannot provide indefinitely improved

resolution. The power necessary to produce the transmitted pulse is given by

$$P = \frac{E_t}{T_p} \tag{2.2}$$

where E_t is the total transmitted energy in the pulse. Therefore since the transmitted energy must remain high enough that the returned pulse at the receiver is strong enough to be noticeable above system noise, reducing the pulse width increases the required power. However there are other ways to increase the resolution in the range direction without the need for small pulse widths. Transmitting chirped sinusoidal waveforms is a commonly used method for improving the range resolution of radar systems. A chirped sinusoidal waveform is a sinusoid with linearly increasing (or decreasing) frequency. A linear frequency modulated (LFM) chirp is given by

$$x(t) = A.\text{rect}\left(\frac{t}{T_p}\right) e^{j2\pi\left(f_c t + \mu t^2\right)} \tag{2.3}$$

where the rect function denotes the pulsed nature of the waveform, with pulse width T_p and amplitude A, centre frequency f_c and chirp rate μ.

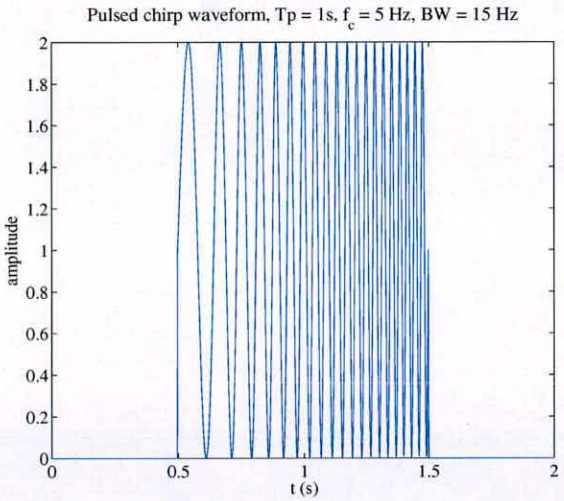

Figure 2.2: *Pulsed chirp waveform.*

When using this type of waveform in the system previously considered, the returns from two closely spaced targets can be identified as being from different targets since the frequency of the sinusoid will be different for each scatterer, ie. the end of the return from the closest target will have a higher frequency than the start of the return from the second further away target [1,2,7].

Instead of range resolution depending upon the pulse length T_p the ability to resolve two closely

spaced targets depends upon the bandwidth of the transmitted waveform, B. This improvement in range resolution is achieved by implementing a matched filter (as discussed in section 2.4.5), in the case of the chirp waveform discussed here this can be implemented as a two stage dechirp and inverse fast Fourier tansform (IFFT) process. Where the received chirp signal is mixed down with a reference chirp, usually delayed by the time of flight to a point at the centre of the scene illuminated by the beam. This results in the compression of the reflected chirp waveform providing improved resolution compared to a simple pulsed system, as shown in Figure 2.4, where the resolution is improved from 15km to 1m by using a 150 MHz chirp bandwidth.

$$B = T_p \mu \tag{2.4}$$

$$\delta_r = \frac{c}{2B} \tag{2.5}$$

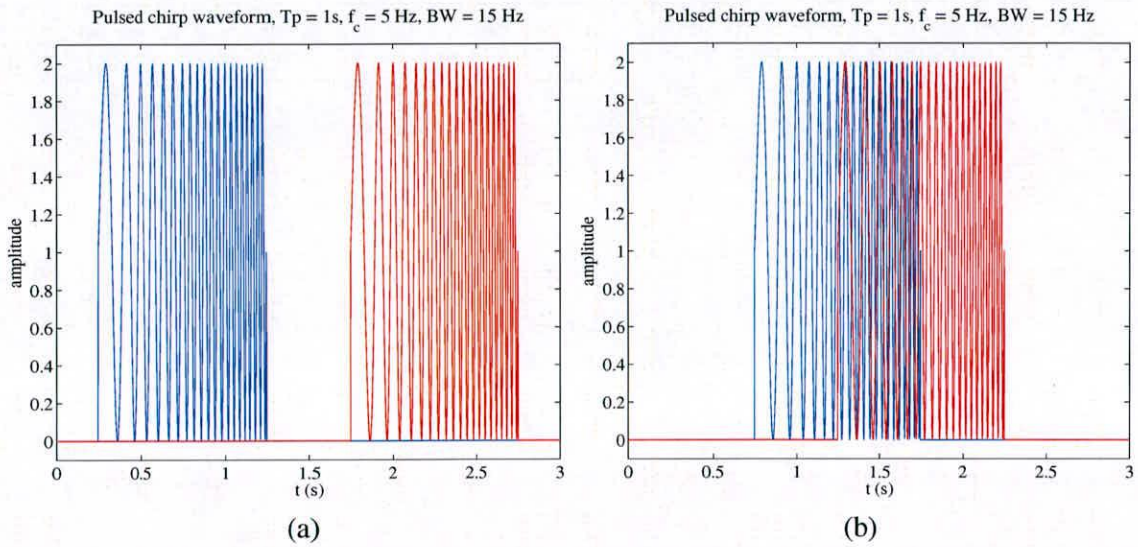

(a) (b)

Figure 2.3: *Return pulsed chirps from closely spaced scatterers. (a) resolvable scatterers. (b) previously unresolvable scatterers.*

This type of chirped signal is just one of a whole family of coded waveforms that can be used to improve the range resolution of radar systems including binary/poly phase coded waveforms and many others, with a large amount of research on this subject available in the open literature. As an alternative to the pulsed mode of operation it is possible to use continuous waveform (CW) signals to perform radar range measurements, using the autocorrelation properties of the transmitted waveform to differentiate between returns from different scatterers [7]. Pulsed LFM waveforms like that given in equation (2.3) will be used for the rest of the work presented in

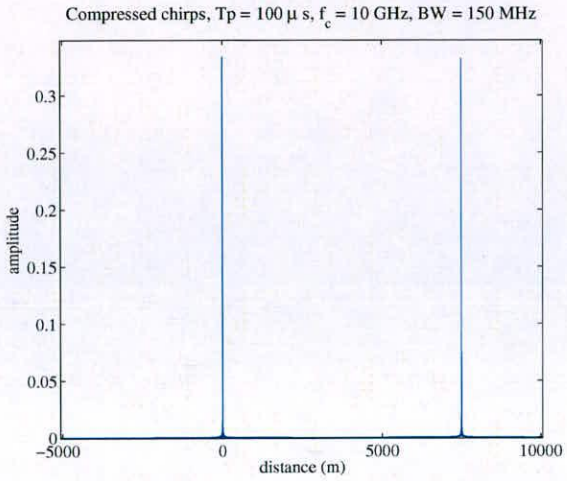

Figure 2.4: *Compressed chirped signal showing improved resolution of chirp over simple pulsed waveform.*

this thesis.

The one dimensional treatment used to illustrate the utility of chirped waveforms for improving the resolution of targets in the range direction is quite limited however, since the transmitted signal doesn't propagate only along a line in the direction of transmission. Instead the beamwidth of the transmitting antenna determines the area of space illuminated by the transmitted signal. As a result returns from targets located in physically different positions within the beamwidth, but with the same return time of flight will appear indistinguishable to the radar receiver. Therefore for the receiver to be able to determine the difference between two closely spaced targets in the cross range direction, that is the direction perpendicular to the range direction, they must be separated by the 3dB beamwidth ie. the width of the radar beam at which returns at the receiver are half as strong as returns at the centre of the beam [7]. The minimum separation distance resolvable by the receiver is given by

$$\delta_{cr} = \frac{R_0 \lambda}{L_{antenna}} \tag{2.6}$$

where R_0 is the range from the antenna to the target, λ is the wavelength of the transmitted radar signal and $L_{antenna}$ is the physical length of the antenna.

However, as equation (2.6) shows this separation distance is dependant upon the range from the antenna to the target and with a typical antenna length of around 1 m, transmitting in the

X-band eg. 10 GHz the minimum resolvable separation achievable at 10 km range is 300 m. This range dependence of cross range resolution of traditional radar prevents it being used as a high resolution imaging system for operation at large distances [1,2,7].

2.2 Synthetic aperture radar

As discussed in the previous section the cross range resolution dependence upon range from antenna to target limits the use of this traditional radar mode for high resolution image formation. However it is possible to use signal processing to synthesise a larger radar antenna or aperture instead of requiring a very large physical antenna for high resolution imaging. To do so the radar platform traverses a linear flight path intermittently transmitting and receiving radar pulses, when these returns are coherently integrated the synthesised aperture improves the dependence of cross range resolution on range to the target. The apparent beamwidth of the synthetic aperture is given by [7]

$$\begin{aligned} B_{SAR} &= \frac{\lambda}{2L_{SAR}} \\ &= \frac{L_{antenna}}{2R_0} \end{aligned} \tag{2.7}$$

where L_{SAR} is the length of the synthetic aperture, which is determined by the size of the 3dB beamwidth on the ground at range R_0

$$L_{SAR} = R_0 B_{3dB} \tag{2.8}$$

therefore the maximum achievable cross range resolution is given by [7]

$$\begin{aligned} \delta_{cr} &= R_0 B_{SAR} \\ &= \frac{L_{antenna}}{2} \end{aligned} \tag{2.9}$$

Notice how this is no longer dependant upon the range to the target, as the extra time spent with the target in the beam cancels exactly with the beamwidth on the ground being wider at longer ranges. However this is the maximum achievable resolution and is not necessarily needed for the application considered therefore an alternative form of equation (2.9) is

$$\delta_{cr} = \frac{R_0 \lambda}{2L_{SAR}} \tag{2.10}$$

therefore the achievable resolution is dependent upon the length of the synthetic aperture [1, 2, 7].

2.2.1 Modes of operation

There are several different modes of SAR operation [1, 2, 7], as demonstrated by the previous derivation the range from radar platform to the target contributes to both the time the target spends within the radar beam and also the beam width on the ground, with the net effect of cancelling the dependence upon range to the target. The conventional SAR imaging mode of operation is to point the radar antenna perpendicular to the direction of flight for the duration of the synthetic aperture, this mode is termed strip-map SAR. This is due to the strip of the ground that the beam covers on the ground which can be used for ground mapping applications. Strip-map SAR provides relatively high resolution imagery (approx. 5 - 10m) and is capable of covering extremely large swathes of the ground (approx. 5 - 10km), this is the mode most commonly used for terrain classification and other applications where the objects of interest are much larger than the achievable resolution afforded by strip-map SAR and vast areas of the ground are to be imaged.

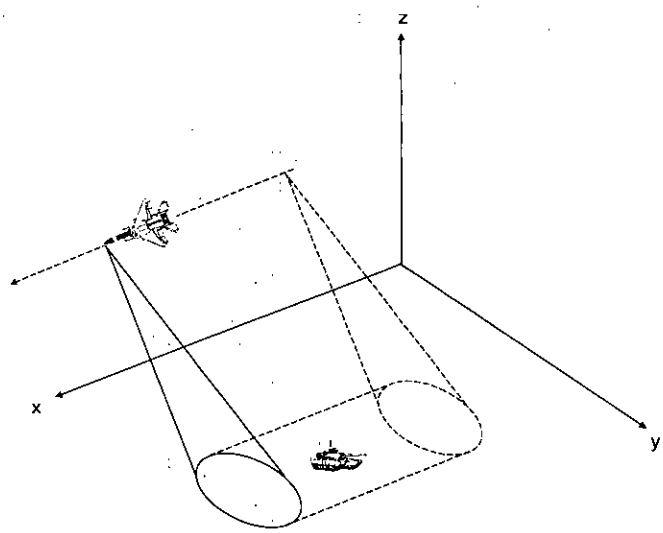

Figure 2.5: *Stripmap SAR mode.*

Alternatively if the area to be imaged is relatively small then the radar antenna can be steered to point at a single point on the ground for the duration of the data collection period, this is termed

spotlight SAR mode. In spotlight SAR because targets are illuminated for even longer than in strip-map mode even better cross range resolution is possible (approx. 0.3 - 2m). However since the beam must be pointed at the same point on the ground over the whole synthetic aperture time the area of coverage on the ground is significantly smaller than for strip-map SAR (approx. 100m - 1km). If a high resolution map of a large area of ground is desired then it is often achieved by using several spotlight SAR images 'stitched' together to form a larger image than achievable using a single spot, but at a higher resolution than can be achieved using stripmap SAR.

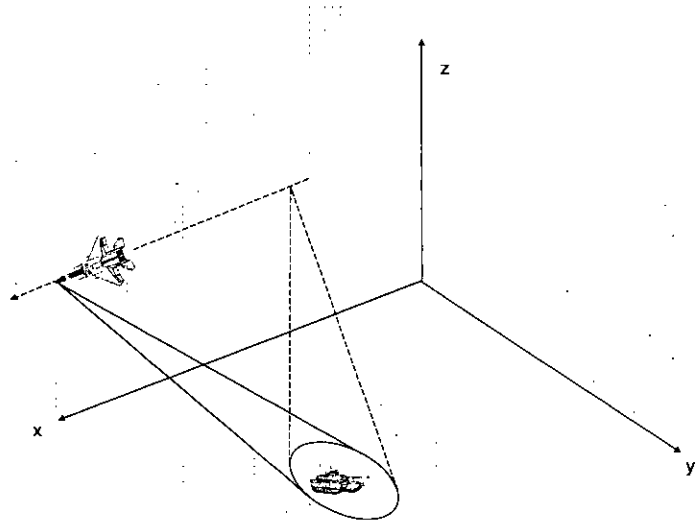

Figure 2.6: *Spotlight SAR mode.*

In addition to strip-map and spotlight SAR modes there is another common SAR mode which utilises a different view of the data collection geometry. Inverse SAR (ISAR) doesn't deal with a moving radar platform synthesising a larger aperture, instead ISAR uses the motion of a target relative to a stationary radar platform to synthesise the aperture. This works on the same principle as spotlight SAR with the roles reversed, the radar beam is steered to be pointing at the target during the whole data collection period and in the same way as for spotlight SAR this can be considered equivalent to the target being stationary and the radar platform following the flight path determined by the target's motion.

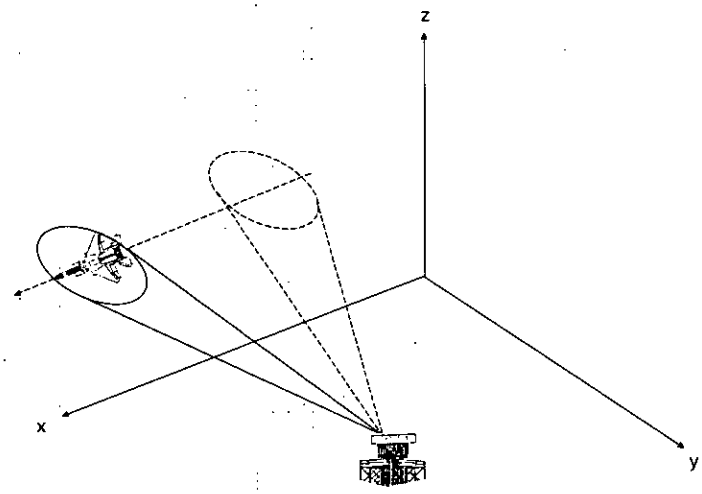

Figure 2.7: *Inverse SAR mode.*

2.2.2 Bistatic SAR

Most radar systems work in a monostatic mode of operation, that is to say that the same antenna is used both to transmit and to receive the radar signal. The main reason for this is the convenience and economic benefit of only requiring a single radar antenna. However this is not the only mode of operation available, monostatic radar is in fact a special case of the more general bistatic radar geometry. In the bistatic setup the transmitting and receiving antennas are distinct and are often located on different platforms. For instance the transmitting antenna and receiving antenna may be mounted on two separate fighter jets, or even the transmitter mounted on the fighter jet and a receiver on-board a missile, in this way radar signals can be used to guide missiles onto their target. Monostatic radar is a special case of the bistatic geometry where the transmit and receive antenna happen to use the same physical hardware. It should also be noted for completeness that the bistatic geometry is itself part of a more general setup. Bistatic radar is a subset of the multistatic setup, where there is typically (though not limited to) a single radar transmitter teamed with several receiving antennas, each receiving platform normally operates independently of the other receiving platforms and therefore can be considered part of a bistatic system since the presence of the other receiving antennas has no effect on this single receiver [16].

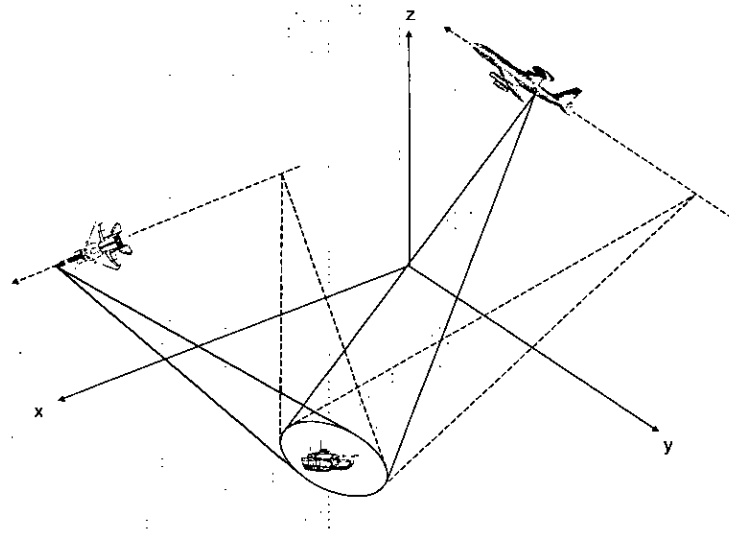

Figure 2.8: *Bistatic spotlight SAR mode.*

Bistatic radar systems can be made to work in all of the modes of operations discussed in the previous section (stripmap, spotlight, ISAR), however this is normally more involved than for the monostatic setup [17–22]. The first example of this additional difficulty is requiring the two separate radar antenna to have their main beams pointed at the same patch of the ground, thus the receiving platform must know the pointing direction of the transmitting antenna at all times when data collection is to be performed. In addition the receiver radar antenna must be tuned to the same centre frequency as the transmitter in order to receive the reflected signals. One of the most significant challenges in implementing an operational bistatic SAR system is the clock coherence requirement. In monostatic SAR the same physical hardware is used both to generate and process the radar signal so the same clock source is used, this is not the case for bistatic SAR systems and therefore the two clocks used must be not only extremely accurate but they must keep the same time to an extremely demanding level. Clock coherence during the data collection interval and phase noise are the biggest barriers to practical implementation of bistatic SAR and are discussed in the literature [23–25].

However despite these difficulties in implementing a bistatic SAR system there are advantages of bistatic SAR over monostatic SAR [9]. The main advantage a bistatic SAR system has over a monostatic system is increased survivability. Bistatic SAR systems offer improved survivability since the receiving platform is operating in a passive receive only mode, therefore not betraying

its location to the enemy. A result of this is that the receive platform may operate closer to the target than would be considered safe for an active transmitting SAR system. A side effect of the receiver operating closer to the scene of interest is that the transmitting platform may operate at a greater stand-off range, possibly out of range of enemy defences. Also since the transmitter may operate at a safe stand off range a more expensive transmitter may be coupled with a cheaper receiver for instance on-board an unmanned aerial vehicle (UAV).

In addition to the improved survivability of bistatic SAR systems a less threatening side effect of the active nature of the transmitting platform than the threat of attack is the potential for directional jamming from the target. It is a commonly used electronic counter measure (ECM) employed to attempt to jam the radar receiver. One way of doing this is to transmit another noise like radar signal of greater power than any reflection that the receiver will detect. Since the target can detect the direction of the transmitted radar signal an effective method of performing this jamming is to steer a high power transmitter in the direction of the enemy transmitter. However since in the bistatic scenario the receiver lies in a different direction and operates in a passive mode this type of directional jamming would require another method of determining the direction of the receiver.

Another opportunity that may be realised with a bistatic SAR system is the potential to image stealthy targets. Many modern aircraft are designed to be stealthy in the presence of radar signals, ie. they are designed to have an extremely low radar cross section (RCS). RCS is a measure of how much radar energy is presented to a radar receiver when the aircraft is illuminated by a radar. Stealthy targets achieve this low RCS in two main ways, firstly they are made of materials designed to absorb energy in the frequency range of radar signals thus reducing the total energy they reflect. Secondly stealthy targets are shaped in such a way as to minimise the radar reflections back in the direction of the incoming beam, however the incoming energy is reflected in other directions. A result of this is that for monostatic systems stealthy targets provide a low RCS, but since bistatic receiver systems are generally not located close to the transmitter some of this scattered energy may be collected limiting the effect of the stealth design [8, 10].

Lastly radar shadows can be considered either a disadvantage or an advantage depending on the application being considered. Shadows can obscure target features making identification more difficult, however algorithms have been developed which use shadows in images to detect the location of moving targets [26]. Radar images suffer shadows in areas behind obstacles which

block the transmitted radar energy in the same way as optical images experience shadows. However in the bistatic configuration the shadows in images are present not only where the line of sight from the transmitter is blocked but also where the line of sight to the receiver is blocked. Hence bistatic SAR images show significantly more shadowed regions than in monostatic SAR images. This is usually interpreted as a disadvantage of bistatic SAR imaging, however it has been proposed that the information about a target that is used for classification and recognition using automatic target recognition (ATR) algorithms depends not only upon the bright returns from the edges of the target but also from the shadows that the target creates on the ground [27]. From this point of view the increased amount of shadowing experienced in bistatic SAR images may actually enable improved ATR performance.

2.3 SAR signal model

The general bistatic SAR system geometry is shown in Figure 2.9 where the transmitting platform traverses a linear flight path with velocity $\mathbf{v}_t$ and instantaneous position given by $\mathbf{x}_t$, likewise the receiving platform follows a linear flight path (not restricted to be in the same direction as the transmitter) with velocity $\mathbf{v}_r$ and instantaneous position given by $\mathbf{x}_r$, where both radar antennae are pointed at the centre of the scene of interest which is located at the origin of the cartesian coordinate set. The vector $\mathbf{u}$ points in the direction of the instantaneous monostatic equivalent position, this is the position of monostatic system that would be the closest equivalent to the bistatic geometry, given by

$$\mathbf{u} = \frac{\mathbf{x}_t + \mathbf{x}_r}{2} \tag{2.11}$$

This vector is in a direction given by θ and bisects the bistatic angle β.

$$\theta = \tan^{-1}\left(\frac{\mathbf{u}_x}{\mathbf{u}_y}\right) \tag{2.12}$$

The mid-pulse angle is the angle θ for the middle pulse position on the synthetic aperture. The scene is considered to be made up of discrete perfectly reflecting point scatterers located at positions $\mathbf{r}_n$ in the x-y plane, commonly referred to as the ground plane or image display frame (IDF) in radar signal processing.

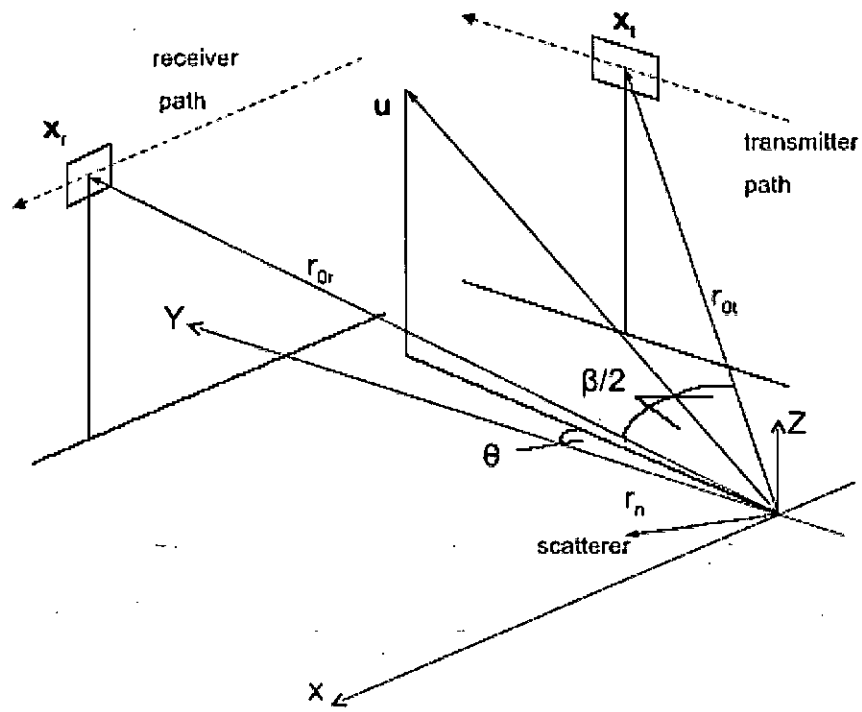

Figure 2.9: *Bistatic SAR system geometry.*

The transmitter antenna transmits a LFM chirp waveform in the direction of the scene

$$s_{tx}(t,\hat{t}) = A_t.\text{rect}\left(\frac{\hat{t}}{T_p}\right)e^{2\pi j\left(f_c t+\mu\hat{t}^2\right)} \tag{2.13}$$

where t is referred to as slow time and $\hat{t}$ is referred to as fast time. The radar platforms are assumed to be stationary during the time of flight of each pulse, since v_t and $v_r << c$, therefore $t = i.PRI$ where PRI is the pulse repetition interval and i is the pulse number.

The pulse is reflected by each scatterer within the scene and is collected by the receiving antenna

$$s_{rx}(t,\hat{t}) = A_t.\sigma.\text{rect}\left(\frac{\hat{t}-\frac{r_t+r_r}{c}}{T_p}\right)e^{2\pi j\left(f_c\left(t-\frac{r_t+r_r}{c}\right)+\mu\left(\hat{t}-\frac{r_t+r_r}{c}\right)^2\right)} \tag{2.14}$$

where r_t and r_r are the ranges from the transmitting and receiving antenna to a scatterer in the scene [1, 2, 28] and σ is the complex reflectivity coefficient of the scatterer.

2.4 Image formation

The purpose of the IFP is to take the signal that arrives at the receiving antenna and use signal processing techniques to form an image. There are many different IFPs in the open literature each with its own particular advantages and disadvantages. The task of a radar system engineer is to make a choice of the most suitable algorithm for the tasks specific to the radar being designed. The main trade off in radar system design is between algorithm complexity, which translates in to hardware complexity and normally the speed with which an image can be formed, and the desired image quality. If the engineer is willing to make certain compromises in the size of scene to be imaged, the achievable resolution and image uniformity/distortion then simpler processing algorithms may be used which are less computationally complex. In this section we shall discuss the most important algorithms in the open literature. Most of these algorithms were originally designed to be implemented in monostatic SAR systems but over time papers have been published demonstrating their applicability to bistatic SAR.

2.4.1 Rectangular format

One of the most simple SAR image reconstruction algorithms in the literature is the rectangular format algorithm (RFA). The RFA as presented in [1, 2, 29] is performed by de-chirping the radar signal collected by the receiving antenna. This dechirp processing can be performed either in hardware as part of a deramp-on-receive system or the dechirp operation can be performed digitally. However most practical systems perform some kind of deramp-on-receive processing to allow the digitiser frequency to be lower than would be required to adequately sample the full bandwidth of the LFM chirp. The reference signal used to perform the dechirp operation is given by [1,2]

$$s_{sc}(t,\hat{t}) = A_0.\text{rect}\left(\frac{\hat{t}-\left(\frac{r_{0t}+r_{0r}}{c}\right)}{T_p}\right).e^{-j2\pi\left(f_c\left(t-\frac{r_{0t}+r_{0r}}{c}\right)+\mu\left(\hat{t}-\frac{r_{0t}+r_{0r}}{c}\right)^2\right)} \tag{2.15}$$

Therefore

$$\begin{aligned} s_{dechirp}(t,\hat{t}) &= s_{rx}(t,\hat{t}).s_{sc}(t,\hat{t}) \\ s_{dechirp}(t,\hat{t}) &= (A_t.A_0).\sigma.\text{rect}\left(\frac{\hat{t}-\left(\frac{r_t+r_r}{c}\right)}{T_p}\right) \\ &\quad .e^{\frac{-j2\pi}{c}\left(f_c+2\mu\left(\hat{t}-\frac{r_{0t}+r_{0r}}{c}\right)\right)(r_t+r_r-r_{0t}-r_{0r})}.e^{\frac{j\pi}{c^2}(r_t+r_r-r_{0t}-r_{0r})^2} \end{aligned} \tag{2.16}$$

where r_{0t} and r_{0r} are the ranges from the transmit and receive platforms to the scene centre respectively, at each pulse position [1, 2]. Alternatively this may be rewritten with round trip distances $l_1 = r_t + r_r$ and $l_0 = r_{0t} + r_{0r}$

$$s_{dechirp}(t, \hat{t}) = (A_t.A_0) \, .\sigma.\text{rect}\left(\frac{\hat{t} - \left(\frac{l_1}{c}\right)}{T_p}\right) .e^{\frac{-j2\pi}{c}\left(f_c + 2\mu\left(\hat{t} - \frac{l_0}{c}\right)\right)(l_1 - l_0)} .e^{\frac{j\pi}{c^2}(l_1 - l_0)^2} \quad (2.17)$$

The term $\frac{l_1 - l_2}{2}$ is the position of the scatterer with respect to the scene centre point. The first phase term in equation (2.17) shows that the signal $s_{dechirp}(t, \hat{t})$ now takes the form of a scaled, rectangular windowed sinusoidal waveform where the frequency of the sinusoid varies with the position of the scatterer within the scene. The second phase term is referred to as residual video phase (RVP) which varies with the scatterer position squared, this term can be ignored for small scene sizes. However for larger scenes this term results in a space varying defocus of each scatterer and further signal processing is required to compensate for this term. To remove the RVP term the signal is passed through a dispersive filter. Equation (2.17) is Fourier transformed and then multiplied with an RVP compensation term given by

$$S_{RVP}(f) = e^{\frac{j4\pi f_s}{\mu}} \quad (2.18)$$

and then inverse Fourier transformed. The result of the dechirp processing after RVP compensation is given by

$$s(t, \hat{t}) = (A_t.A_0) \, .\sigma.\text{rect}\left(\frac{\hat{t} - \left(\frac{l_0}{c}\right)}{T_p}\right) .e^{\frac{-j2\pi}{c}\left(f_c + 2\mu\left(\hat{t} - \frac{l_0}{c}\right)\right)(l_1 - l_0)} \quad (2.19)$$

using a binomial expansion and retaining only the linear terms as shown in appendix A, we can approximate

$$(l_1 - l_0) \approx \frac{(\mathbf{x}_t + \mathbf{x}_r)\, \mathbf{r}_n}{l_0} = \mathbf{x} \quad (2.20)$$

where $\mathbf{r}_n$ is the position vector for the scatterer relative to the scene centre, so that equation (2.19) can be written as

$$S(\mathbf{k}) = \int_{-\infty}^{\infty} (A_t.A_0) \, .\sigma.\text{rect}\left(\frac{\hat{t} - \left(\frac{l_0}{c}\right)}{T_p}\right) .e^{j\mathbf{k}.\mathbf{x}} d\hat{t} \quad (2.21)$$

where

$$\mathbf{k}(t,\hat{t}) = \frac{-2\pi}{c}\left(f_c + 2\mu\left(\hat{t} - \frac{l_0}{c}\right)\right). \tag{2.22}$$

Re-writing equation (2.19) in this way it can be seen to take the form of the Fourier transform of the scene and $\mathbf{k}$ is said to be the Fourier kernel. The result of this dechirp processing is that the scene can be reconstructed by taking a 2D inverse Fourier transform (IFT), this can be implemented efficiently using the fast Fourier transform (FFT). This algorithm is referred to as the rectangular format algorithm since the data is stored in a rectangular matrix format for use in the FFT used to reconstruct the scene. With the summed returns for each pulse forming a row within this matrix. Therefore to perform the IFT the FFT processor simply performs two separate 1D IFT operations, one along the rows of the matrix and the second down each column.

Since a linear approximation was used in this derivation the result is not exact. The linear approximation is only valid for small scenes relative to the round trip distance l_1 and for large chirp carrier frequencies with low reconstructed image azimuth resolutions, $f_c = 10$ GHz and $\delta_{cr} = 0.5$ m for example. For scenarios where this is not the case the approximation will result in space variant defocus of scatterers in the reconstructed scene, ie. scatterers will be defocused by an amount dependant upon their position within the scene. Scatterers displaced in the range direction will be blurred in the azimuth direction and scatterers displaced in the azimuth direction will be blurred in both range and azimuth directions. The further a scatterer is from the scene centre the greater the degree of defocus [1, 2].

For acceptable image quality the phase error for a scatterer near the scene edge is usually limited to $\frac{\pi}{2}$ and the resulting limit on the size of scene that can be imaged is given by [1, 2]

$$|x| \leq \frac{2\delta_r \delta_{cr}}{\lambda}, \qquad |y| \leq \frac{2\delta_{cr}^2}{\lambda} \tag{2.23}$$

Assuming 0.5 m resolution in both the range and cross range directions and a 10 GHz centre frequency, the maximum scene size which can be processed using the RFA with no noticeable defocus is a 33.33m x 33.33m square. This small scene size makes rectangular format processing unsuitable for most high resolution SAR applications, however the RFA is simple to understand and implement and as a result requires little computation power compared to many SAR IFPs [1, 2].

2.4.2 Polar format

The polar format algorithm (PFA) as discussed in [1, 2, 30–33] is a commonly used method in SAR image reconstruction since it is relatively simple, building on the theory of the RFA, yet achieves high quality images while being computationally efficient to implement. The PFA recognises that the errors in the RFA are introduced due to the rectangular data storage format. The PFA can be explained in terms of the projection slice theorem [1, 30–32], the transmitted chirp pulses form slices of the target scene in the Fourier domain. A consequence of this is that the location of the obtained area in this domain referred to as k-space, is a polar arc offset from the polar origin by the chirp carrier frequency and the bistatic look direction, as illustrated in Figure 2.10. The area collected along this line centred around the carrier frequency is determined by the chirp bandwidth.

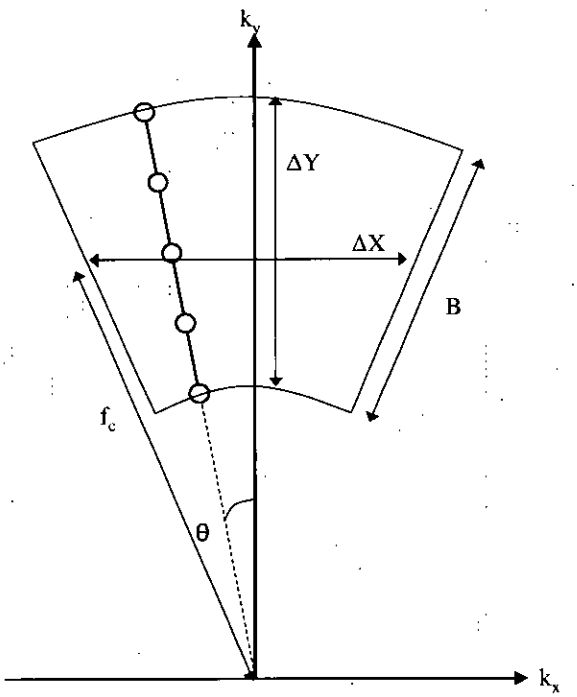

Figure 2.10: *Polar format sampled area of k-space.*

$$\mathbf{k} = k.\hat{\mathbf{u}} \tag{2.24}$$

where

$$k(t,\hat{t}) = \frac{-2\pi}{c}\left(f_c + 2\mu\left(\hat{t} - \frac{l_0}{c}\right)\right). \tag{2.25}$$

$$\hat{\mathbf{u}} = \frac{\hat{\mathbf{u}}_t + \hat{\mathbf{u}}_r}{2} \tag{2.26}$$

$$\begin{aligned}\hat{\mathbf{u}}_t &= \frac{x_t}{|x_t|}\\ \hat{\mathbf{u}}_r &= \frac{x_r}{|x_r|}\end{aligned} \tag{2.27}$$

$$\theta = \tan\left(\frac{\hat{\mathbf{u}}_x}{\hat{\mathbf{u}}_y}\right) \tag{2.28}$$

The result of storing the data in this polar format can be seen in Figure 2.11 where the figure shows the result of equation (2.19) for a single scatterer displaced in the range direction beyond the maximum allowable scene size for the RFA. This results in a single sinewave being present in the complex signal collected, this single frequency when IFT'd will result in the location of the scatterer within the scene. However as a result of the collection grid being on polar axes the peaks and troughs of the sinewave are curved, when processed using the RFA this spread of frequencies results in defocus. Careful examination of Figure 2.11(a) shows slight curvature of the dark bands which is most noticeable at the top and bottom of the plot where a horizontal line is present providing a reference. When the data is correctly stored in the polar format this defocus is not present, as shown in Figure 2.11(b).

Similarly the magnitude of the collected complex radar signal for a single scatterer displaced in the cross range direction, stored in rectangular and polar formats is shown in Figure 2.12. The effect of the polar distortion can be seen in Figure 2.12(a) at the left and right edges of the plot where the slope of the dark bands are visible, this effect has been removed by using the polar storage format as shown in Figure 2.12(b).

In order to make use of the FFT to form the reconstructed image the sampled phase history which lies on points on a polar grid needs to be resampled onto a regular rectangular grid. Since this is the required data format for the most efficient FFT algorithms, however FFT algorithms which use other sample grids for input data do exist [34–36]. This resampling or interpolation process is a potential source of errors for the PFA since resampling near the data boundary is error prone, hence window functions are often employed to reduce the significance of these points in the FFT resulting in lower scatterer sidelobe levels. Resampling in the PFA is often

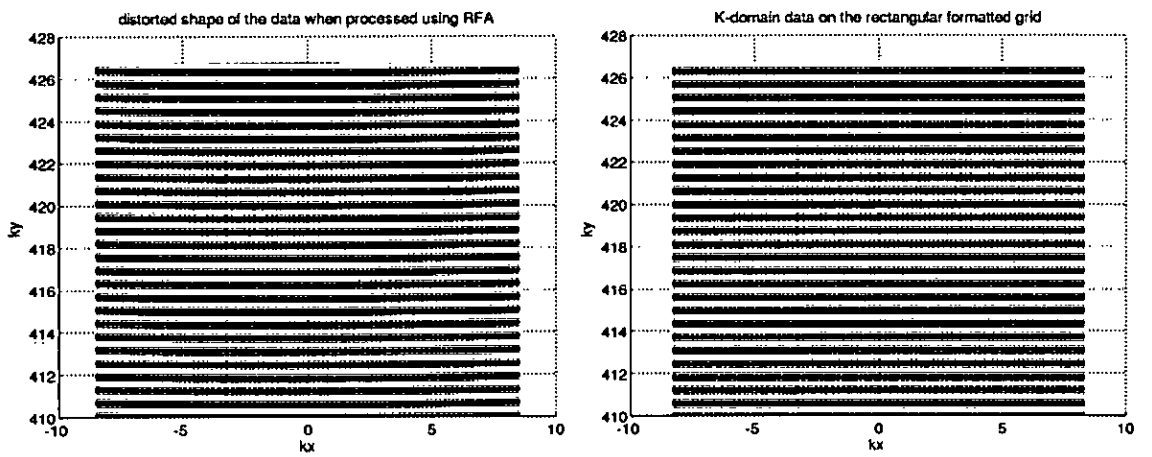

Figure 2.11: *Shape of sinusoidal waveform due to a scatterer displaced in the range direction beyond the maximum scene size for RFA, in different storage formats. (a) RFA. (b) PFA. Figure adapted from [1].*

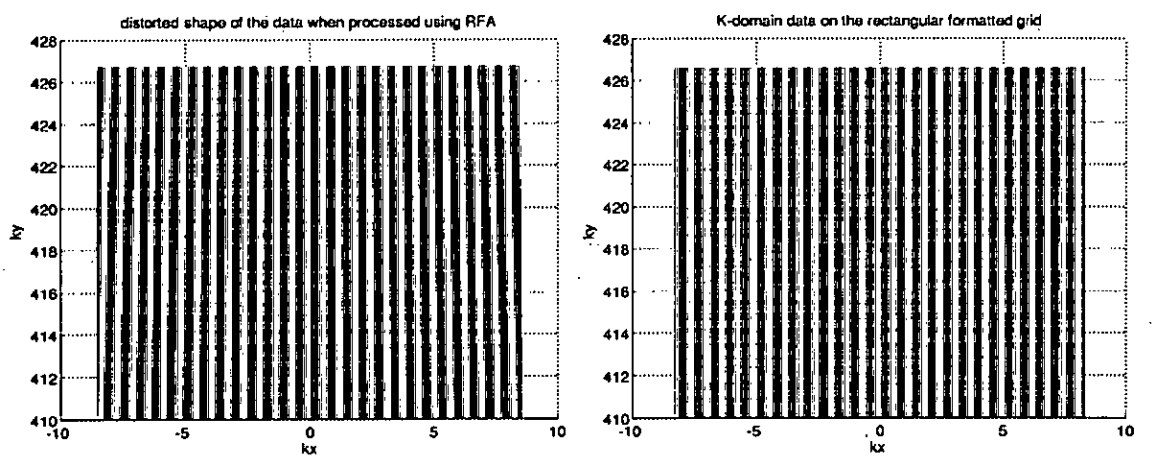

Figure 2.12: *Shape of sinusoidal waveform due to a scatterer displaced in the cross range direction beyond the maximum scene size for RFA, in different storage formats. (a) RFA. (b) PFA. Figure adapted from [1].*

performed using the keystone interpolation method [1,2] where the 2D resampling operation is performed as 2 separate 1D resampling operations, this is discussed further in Section 2.5.

The resolution achievable using the PFA is dependent upon the extent of the sampled area of k-space as shown in Figure 2.10. The greater the extent of this area, the finer resolution can be achieved using the PFA IFP due to the image forming 2D IFT.

$$\delta_r = \frac{2\pi}{\Delta X} \tag{2.29}$$

$$\delta_{cr} = \frac{2\pi}{\Delta Y} \tag{2.30}$$

The PFA corrects for the linear component of migration through range cells (MTRC) [37–39] which arises as a result of the varying range from the radar platform to the each scatterer during the SAR data collection interval. As the radar platform traverses the synthetic aperture, at each pulse repetition interval the range to each scatterer in the scene varies, when this variation in range is greater than the range resolution of the system the scatterer is said to migrate into another range cell. If MTRC is not compensated for then the spread of scatterer energy over different resolution cells causes image defocus. Different SAR IFPs compensate for varying orders of MTRC with improved image quality for IFPs which implement more complete compensation for MTRC. RFA compensates only for the linear terms in slow time and scatterer position within the scene of MTRC. PFA compensates for the full slow time variation in range but only compensates for the linear component of scatterer position within the scene. Algorithms are present in the literature that overcome this weakness of the PFA, for instance the image defocus due to uncompensated MTRC can be corrected using a spatially varying filter for every pixel in the SAR image [40–42]. However this type of processing requires additional computational load which makes implementing the version of the PFA described less appealing when compared to other IFPs based on a more complete mathematical solution to the problem.

However the PFA is based on the plane wave approximation and hence still leads to blurring errors when the target scene size is comparable to the stand-off range. In a similar manner to the RFA the uncorrected phase errors, which are the result of the uncorrected components of MTRC, result in a defocusing in images of large scenes at high resolutions particularly at close stand-off ranges. The limit on the maximum scene size that can be processed using the PFA

while keeping the uncompensated phase error below $\frac{\pi}{2}$ is given by

$$|x| = |y| = \delta_x \sqrt{\frac{2R_0}{\lambda}} \tag{2.31}$$

For a 10 GHz, 0.5 m resolution SAR system operating at a stand-off range of 20km this results in a maximum allowable scene size of approx. 1155 m x 1155 m to ensure minimal defocusing of scatterers within the scene due to approximations inherent in the PFA.

The PFA is the main algorithm used throughout this thesis for image reconstruction for the reasons stated previously.

2.4.3 Range migration

The range migration algorithm (RMA) as discussed in [2, 14, 43–45] is a Fourier imaging method like the RFA and PFA, however it does not rely on the plane wave approximation that is implicit in these two algorithms. In addition the RMA compensates completely for the MTRC problem, therefore the RMA does not demonstrate the same spatially variant scatterer defocus seen in SAR images formed using the RFA or PFA..

The first stage of processing in the PFA is to deramp the received LFM chirp signal with a reference signal based on the time of flight to the scene centre which varies on a pulse to pulse basis, this process deramps the received LFM chirp in both the range and azimuth directions. Whereas the deramp processing in the RMA is performed using a reference signal which is based on the time of flight to a line through the scene centre parallel to the flight path of the platform.

$$s_{line}(t,\hat{t}) = A_0.\text{rect}\left(\frac{\hat{t} - \left(\frac{r_{st}+r_{sr}}{c}\right)}{T_p}\right).e^{-j2\pi\left(f_c\left(t-\frac{r_{st}+r_{sr}}{c}\right)+\mu\left(\hat{t}-\frac{r_{st}+r_{sr}}{c}\right)^2\right)} \tag{2.32}$$

where r_{st} and r_{sr} are the distance to the line through the scene from the transmit and receive platforms respectively. Therefore

$$s_{dechirp}(t,\hat{t}) = (A_t.A_0).\sigma.\text{rect}\left(\frac{\hat{t} - \left(\frac{l_1}{c}\right)}{T_p}\right).e^{\frac{-j2\pi}{c}\left(f_c+2\mu\left(\hat{t}-\frac{l_s}{c}\right)\right)(l_1-l_s)}.e^{\frac{j\pi}{c^2}(l_1-l_s)^2} \tag{2.33}$$

where $l_1 = r_t + r_r$ and $l_s = r_{st} + r_{sr}$. After RVP processing the input to the RMA algorithm is given by

$$s(t,\hat{t}) = (A_t.A_0)\,.\sigma.\text{rect}\left(\frac{\hat{t}-\left(\frac{l_s}{c}\right)}{T_p}\right).e^{\frac{-j2\pi}{c}\left(f_c+2\mu\left(\hat{t}-\frac{l_s}{c}\right)\right)(l_1-l_s)} \tag{2.34}$$

The first stage of the RMA is to perform an azimuth Fourier transform, this brings the signal phase history into the frequency (in range) - spatial-frequency (in azimuth) domain which is called the $\omega - k$ domain, in fact the RMA is often referred to as the $\omega - k$ algorithm [2, 43]. This azimuth Fourier transform can't be performed analytically and analysis using the principle of stationary phase is performed to determine the result of the azimuth Fourier transform.

$$s_{rma}(X_a,k_r) = (A_t.A_0)\,.\sigma.\text{rect}\left(\frac{\left(\left(\frac{\mathbf{x}_t+\mathbf{x}_r}{2}\right)-\mathbf{x}_{ac}\right)}{L_{SAR}}\right) rect\left(\frac{\hat{t}-\frac{l_s}{c}}{T_p}\right) e^{-jk_r(r_t-r_s)} \tag{2.35}$$

where

$$k_r = \frac{4\pi\mu}{c}\left(\frac{f_c}{\mu}+\hat{t}-\frac{l_s}{c}\right) \tag{2.36}$$

In the $\omega - k$ domain equation (2.35) is multiplied by a 2D matched filter to remove the range curvature for the scene centre scatterer. The 2D matched filter is given by

$$\phi_{MF}(k_x,k_r) = -\frac{l_s}{2}k_r + \frac{l_s}{2}\sqrt{k_r^2-k_x^2} \tag{2.37}$$

Since the range curvature correction is only exact for the scene centre, the residual range curvature is removed by Stolt interpolation. This interpolation from k_x, k_r to k_x, k_y is performed by a change of variables

$$k_y = \sqrt{k_r^2-k_x^2} \tag{2.38}$$

Before the Stolt interpolation the samples in k_x, k_r lay on uniform sample points defined by lines of constant k_r and k_x, which translate into points lying on circles is k_x, k_y sampled uniformly in the k_x direction. After the Stolt interpolation the sample points lie on uniformly spaced points on a rectangular grid in k_x, k_y within the boundary of the region of k-space.

At this stage all that needs to be done to form an image of the scene is to perform a 2D FFT on the regularly sampled data. However in the RMA different scatterers occupy different areas of k-space as shown in Figure 2.13, therefore to ensure all scatterers have a common point spread function it is common to use only a rectangular region of the data which has contributions from

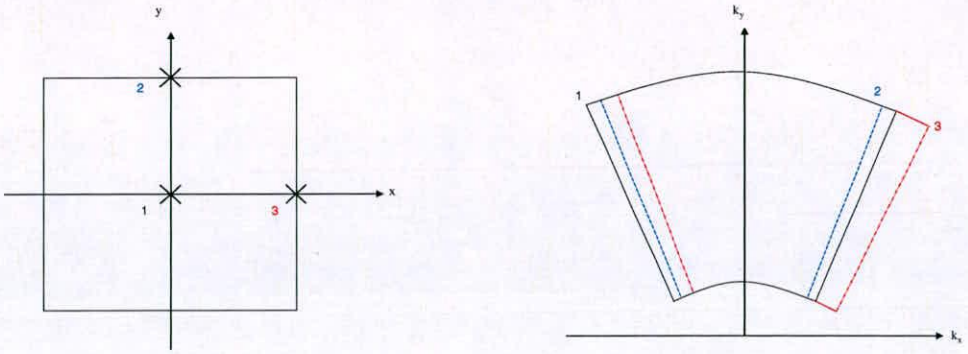

(a) (b)

Figure 2.13: *Areas of k-space for different scatterers within a scene of interest when using RMA (a) location of scatterers within scene. (b) sampled areas of k-space for each scatterer.*

all the scatterers in the scene when performing the FFT, in a similar fashion to the PFA. The choice of the area of k-space to use for the RMA is non-trivial and comes down to application specific preferences, for instance since using a limited region of the data lowers the achievable resolution it may be preferable to have the full resolution allowed at the expense of having a different psf for each scatterer. In addition to this issue, the RMA requires data which is not dechirped in the azimuth direction. This means that the input data to the IFP must have a higher azimuth sample frequency than would be necessary for a deramp on receive system.

The RMA is a more complicated IFP than the RFA or the PFA and as such is more difficult to implement in an actual radar system. However the RMA is a more general solution to the SAR IFP problem since it does not rely upon the plane wave assumption. Hence RMA does not suffer the image quality degradation or the image distortion experienced using PFA for large scene sizes imaged at low stand-off ranges.

2.4.4 Chirp scaling

The chirp scaling algorithm (CSA) as discussed in [2,13,46] is a computationally efficient variation of the RMA which only requires FFTs and complex multiplications, no interpolations are necessary. CSA approximates the Stolt interpolation of the RMA by an FFT and multiplication, due to this approximation the CSA doesn't completely compensate for MTRC and hence experiences image degradation and distortion in a similar way to the PFA for large scene sizes [2]. The CSA operates on chirped data in the range direction and azimuth motion compensation is performed to a line, in the same way as the RMA this means that the azimuth chirp is still

present on the input data. The CSA is a wavenumber domain algorithm since it operates mostly in the wavenumber or spatial-frequency domain.

1. Azimuth FFT
2. 1st phase correction - Chirp scaling operator
3. Range FFT
4. 2nd phase correction - Range matched filter
5. Range IFFT
6. 3rd phase correction - 2D phase compensation
7. Azimuth IFFT

After range compression each scatterer follows a hyperbolic path through the scene due to the variation in range over the aperture length. The nonlinear component of each scatterer's path is range curvature and the variation in range curvature across the scene is differential range curvature. The CSA is designed to equalise the range curvature of all the scatterers in the scene such that a space-invariant matched filter focuses all scatterers.

2.4.5 Matched filtering

In the Fourier based IFPs considered so far in this chapter the image formation FFT has been used as a computationally efficient method of performing the matched filter operation require to form the SAR image from the collected radar returns. Matched filtering (MF) is the mathematically ideal method of image formation, as a maximum likelihood estimator (MLE) for the complex reflectivity function, $\sigma_n(x, y)$ [1, 2, 28].

$$s(t, \hat{t}) = \sum_n \sigma_n . e^{j\phi(t,\hat{t})} \tag{2.39}$$

where

$$\phi(t, \hat{t}) = -2\pi \left(f_c \left(\hat{t} - \left(\frac{r_{0t} + r_{0r}}{c} \right) \right) + \mu . \left(\hat{t} - \left(\frac{r_{0t} + r_{0r}}{c} \right) \right)^2 \right) \tag{2.40}$$

as in equation (2.14)), omitting the pulse envelope and signal amplitudes for simplicity.

Assume a uniform grid of image pixels, analysing each pixel at a time assuming that there is a scatterer present at each pixel location, (x, y). The value of the pixel being interrogated is computed as a MLE of the complex reflectivity function. The MLE of the value of the pixel results in a least squares cost function

$$J = \sum_{i=1}^{N_p} \sum_{j=1}^{N_s} \left| s(t, \hat{t}) - \sigma_n(x, y).e^{j\phi_{x,y}(t,\hat{t})} \right|^2 \tag{2.41}$$

where

$$\phi_{x,y} = \phi(t, \hat{t}) \tag{2.42}$$

for a scatterer at $\mathbf{r}_n = (x, y)$.

Differentiating equation(2.41) with respect to the real and imaginary parts of σ_n gives

$$\delta J = 2 \sum_{i=1}^{N_p} \sum_{j=1}^{N_s} \sigma_n(x, y) - s(t, \hat{t}) e^{-j\phi_{x,y}(t,\hat{t})} \tag{2.43}$$

which when set to zero allows a solution for the least squares estimate of the pixel value to be found.

$$\sigma(x, y) = \frac{1}{N_p N_s} \sum_{i=1}^{N_p} \sum_{j=1}^{N_s} s(t, \hat{t}) e^{-j\phi_{x,y}(t,\hat{t})} \tag{2.44}$$

This is repeated for all pixel locations in the image. Calculating this least squares estimate requires a total of $O(N_p N_s)$ computations per pixel and assuming that there are N^2 pixels in the image, then this leads to a computational load of $O(N^2 N_p N_s)$ or $O(N^4)$ if we assume that $N_p = N_s = N$. However MF can be implemented in a more efficient manner using a convolution back-projection algorithm, as discussed in section 2.4.6.

If far field or planar wave approximations are valid then the MF can be implemented in a computationally efficient manner using the FFT, since the approximations linearise the phase of the matched filter kernel. This approach is used in both the RFA and PFA algorithms covered in sections 2.4.1 and 2.4.2 respectively.

2.4.6 Convolution back-projection

The convolution back-projection (CBP) algorithm is an entirely spatial domain imaging technique, which achieves the image formation matched filtering without using FTs, yet is more

computationally efficient than the approach described in the previous section. The algorithms discussed in [2,47,48] are based on the tomographic back-projection algorithm.
The received radar returns are dechirped with a reference chirp delayed to the scene centre so that the return from each scatterer is a sinusoid with frequency proportional to the differential range $(r_t - r_0)$. As per the projection slice theorem [1,30], a Fourier transform (FT) of a 1D projection of a 2D function $g(x, y)$ made at an angle θ_n is a slice through $G(\omega, \theta)$ the 2D FT of the scene $g(x, y)$ at θ_n, and is given by $P_\theta(\omega)$.

$$P_\theta(\omega) = \int P_\theta(t) e^{-j\omega t} dt \tag{2.45}$$

So the scatterers all project perpendicularly to the radar line of sight to form the collected data which is a slice through the 2D FT of the whole scene. Note that scatterers will project into different range bins depending on the angle of the radar line of sight. A single pulse only resolves scatterers in range so that many scatterers occupy the same range bin as shown in Figure 2.14.

Tomographic reconstruction generates an image by projecting the range only FT of each radar line of sight slice individually back onto the 2D grid of image pixels, hence back-projection. The SAR image reconstruction is performed via the following equations. Calculating $P_\theta(\omega)$ for every pulse angle θ by integrating over the radar bandwidth ω_1 to ω_2, gives Q(t) termed the filtered projection. Then the SAR image reconstruction is achieved by integrating Q(t) over the look angle θ, where $t = r\cos(\phi - \theta)$ and (r, ϕ) are the projection of (ω, θ) in the (x,y) plane.

$$Q(t) = \int_{\omega 1}^{\omega 2} P_\theta(\omega) |\omega| e^{-j\omega t} d\omega \tag{2.46}$$

$$g(r, \psi) = \int_{-(\theta_m/2)}^{(\theta_m/2)} Q_\theta(r cos(\psi - \theta)) d\theta \tag{2.47}$$

This process can be summarised as follows:

1. Place image grid over (x,y) plane.
2. IFT P_n and place result on (x,y) plane at angle θ_n.
3. For every image pixel $O_{x,y}$ determine the input value of the resolution cell $L_{x,y}$ by projecting perpendicularly and interpolating.

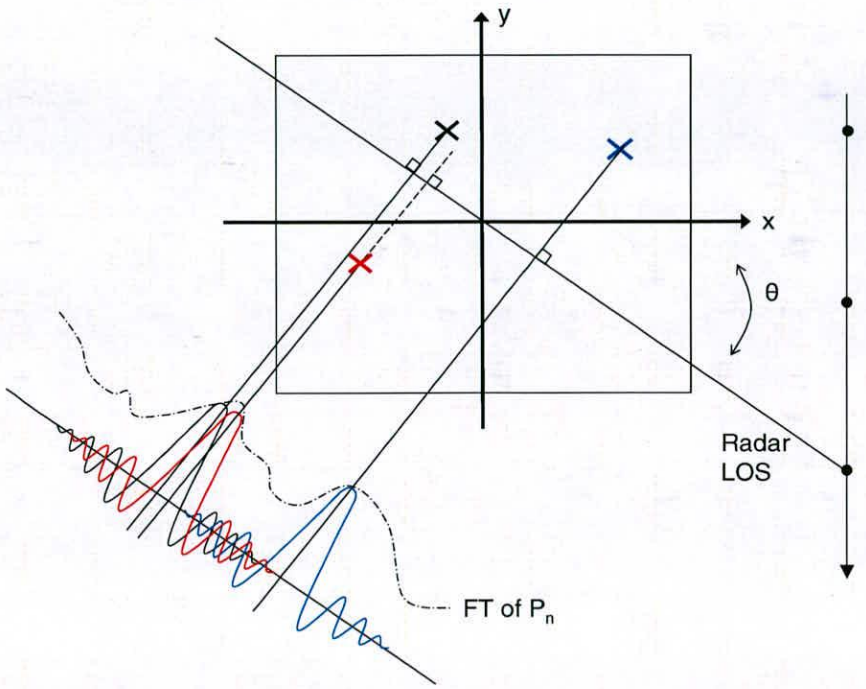

Figure 2.14: *Illustration of the tomographic projection slice theorem. Each pulse contains data from all points in the scene projected onto the radar line of sight [2].*

4. Add this value to the existing value of $O_{x,y}$.

5. Repeat for all P_n.

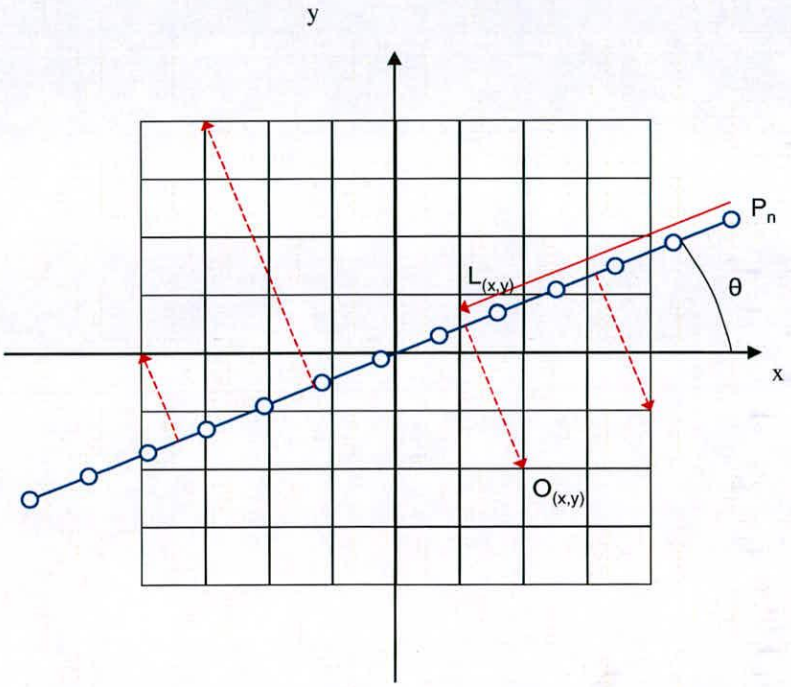

Figure 2.15: *Image formation using the CBP algorithm. For each pulse interpolate the value of FT of P_n and project to the position of each image pixel in $O_{(x,y)}$ [2].*

CBP is very similar to image formation using the MF approach and as such CBP is much more computationally expensive than many of the Fourier domain algorithms and isn't immediately compatible with the most common autofocus algorithms, yet it has the advantage that it doesn't rely on the plane wave approximation, and as no 2D Fourier transform of the data is used to form the SAR image all the data does not need to be collected before image formation begins. This allows an image to be 'grown' as more and more pulses are used to form the image the resolution improves, it could be desirable to start forming a low resolution image and then use target detection software to determine if there are any targets of interest present before proceeding to form a more accurate image [48].

Fast back-projection algorithms are proposed in [49, 50], which have computational efficiency

gains. The idea is that back-projecting the data for four sub-images, each a quarter of the size of the original image only requires an eighth of the computation. Resulting in an overall computational saving of a factor of two over the standard back-projection algorithm. Recursively splitting the image like this means that drastic computational savings can be achieved. For CBP the computational cost of forming an N x N image is $O\left(N^3\right)$ where as the proposed fast CBP algorithm achieves the result in $O\left(N^2 log_2 N\right)$ operations.

2.5 Interpolation and resampling

Modern radar systems are built using digital microprocessors rather than the analogue components that were used in the early radar systems during the second world war. As a result all of the signal processing is performed on digital sampled versions of the continuous time signals used in the mathematics in the previous sections. A discrete sampled digital representation of an infinite length continuous time function takes the form

$$x(t) = \sum_{n=-\infty}^{\infty} x(n\Delta t)\delta(t - n\Delta t) \tag{2.48}$$

where $\delta(t)$ is the Dirac delta function and Δt is the sampling interval. As shown in Figure 2.16. Early information theory tells us that there is a lower limit on the number of samples that can be used to adequately represent the continuous time function. The Nyquist criterion dictates that this lower limit is reached when the digital sampling frequency is equal to twice the highest frequency component present in the continuous time function.

$$f_s \geq 2f_{max} \tag{2.49}$$

Provided that this minimum sampling frequency limit is observed then there is enough information present to evaluate samples $x(n\Delta t)$ at any value of $n\Delta t$ [51]. If the resulting resampling operation increases the number of samples of $x(t)$ then this process is referred to as interpolation, whereas if the resampling results in fewer samples of $x(t)$ then the process is referred to as decimation [3].

The process of interpolating a function $f(x)$ by an arbitrary factor L is illustrated in Figures 2.17 - 2.18 adapted from [3].

The original sampled signal is shown in Figure 2.17(a) and the FT of the signal in Figure

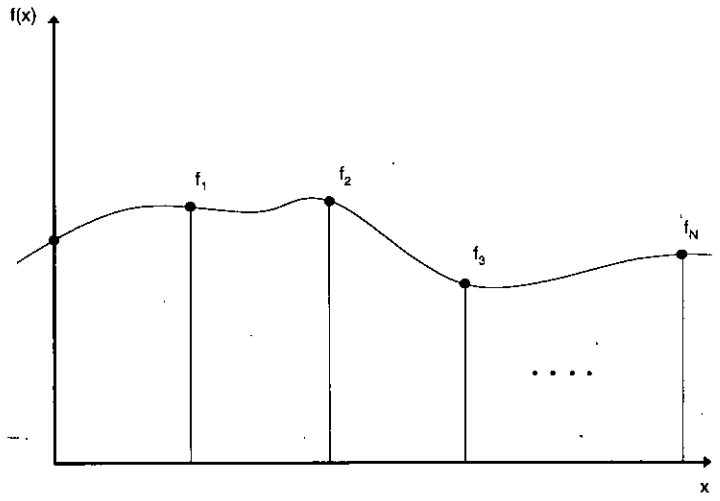

Figure 2.16: *Discrete sampled digital representation of a continuous time function.*

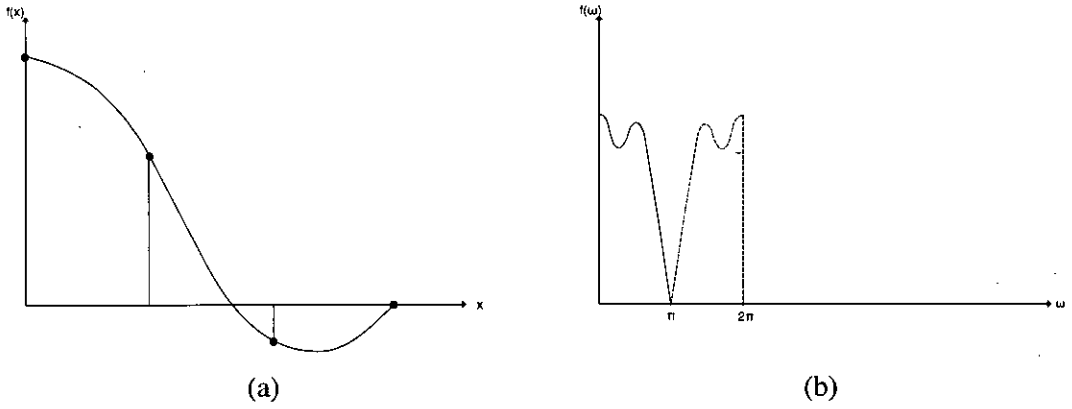

Figure 2.17: *(a) Sampled digital signal representation ,$f(x)$, and (b) Fourier Tranform, ω. Figure adapted from [3].*

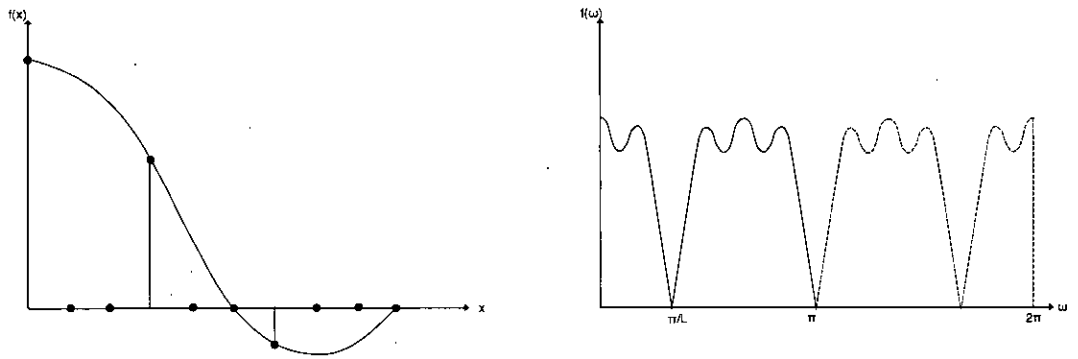

(a) (b)

Figure 2.18: *(a) Zero padded version of the sampled digital signal and (b) Fourier Transform. Figure adapted from [3].*

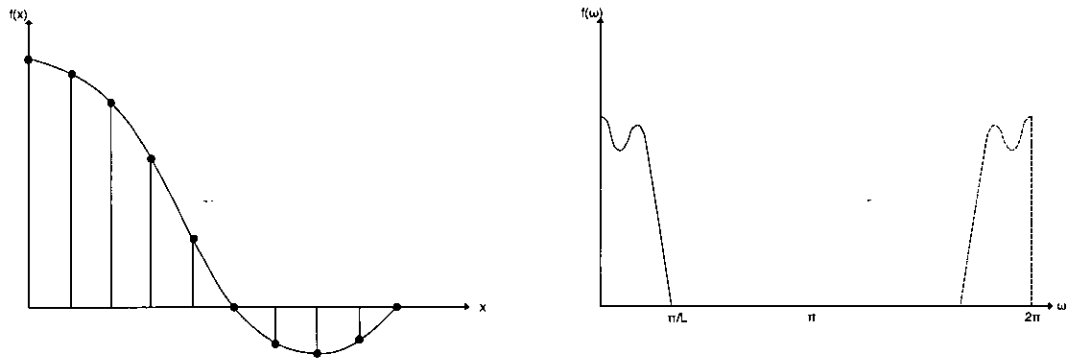

(a) (b)

Figure 2.19: *(a) Interpolated sampled digital signal and (b) Ideal low pass filtered Fourier transform. Figure adapted from [3].*

2.17(b). The desired increased sample frequency sampled signal is shown in Figure 2.18(a) where the unknown sample values are set to zero, this process is referred to as zero padding. The result of this zero padding can be seen in the frequency domain in Figure 2.18(b) where ambiguous copies of the signal occupy the spectrum. An ideal low pass filter is implemented around the desired part of the spectrum to remove the undesirable ambiguous copies of the signal as seen in Figure 2.19(b). When the IFT of the filtered signal is evaluated the result is as shown in Figure 2.19(a), the value of continuous time signal at each of the previously unknown desired sample locations has been obtained.

The ideal low pass filter can be implemented in the time domain as the sum of scaled $\mathrm{sinc}(x)$ (or $\frac{\sin(x)}{x}$) functions placed at each of the known sample points [52, 53]. The multiplication of the FT of $f(x)$ by the ideal low pass filter in the frequency domain can instead be implemented as a convolution of $f(x)$ with the FT of the ideal low pass filter. The FT of the low pass filter is a $\mathrm{sinc}(x)$ function.

$$x(t) \approx \sum_{n=a}^{b} G.x(n\Delta t)\phi_n(t) \tag{2.50}$$

where

$$\phi_n(t) = \frac{\omega_{bp}\Delta t}{\pi} \frac{\sin\left(\omega_{bp}\left(t - n\Delta t\right)\right)}{\omega_{bp}\left(t - n\Delta t\right)} \tag{2.51}$$

where G is the filter gain term and ω_{bp} is the pass band edge of the ideal low pass filter to be implemented. This time domain implementation of interpolation is illustrated in Figure 2.20.

For computational efficiency and applications where the spectral purity of the interpolated signal is of less importance, the interpolation is often performed by other simpler means. Examples of these methods are illustrated in Figure 2.21. Some of the methods used to perform computationally cheap interpolation are fitting a limited order polynomial through the known points and using the value of the polynomial at the desired sample locations to provide an estimate of the continuous time signal. Linear interpolation involves simply fitting a straight line between each pair of know sample values and using the value of this line at the unknown sample locations to estimate the value of the continuous time signal. Alternatively the simplest method would be to use the value of the nearest known sample as the value of the desired sample, known as nearest neighbour interpolation.

The cases considered thus far have dealt with interpolation from uniformly sampled signals to uniform desired sample locations. Interpolation from uniformly sampled signals to nonuniform desired sample locations is not significantly different from the methods described already, how-

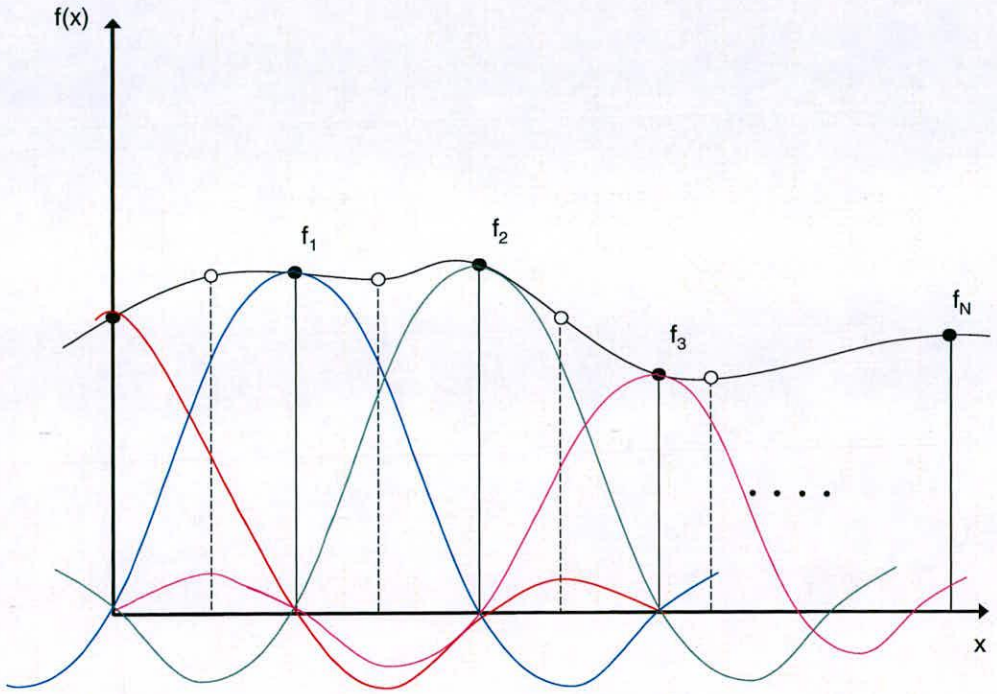

Figure 2.20: *Sinc(x) interpolation.*

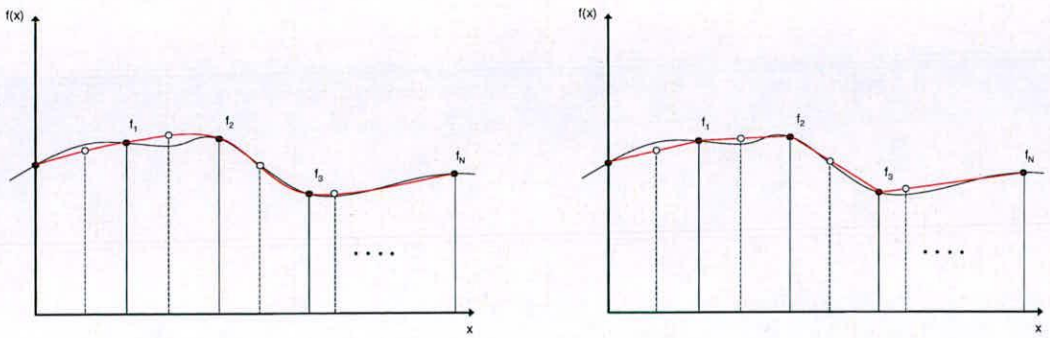

(a) (b)

Figure 2.21: *(a) Polynomial approximation. (b) Linear interpolation.*

ever interpolating from nonuniformly sampled signals is a more challenging problem. Other types of interpolation functions must be applied, one of the alternative interpolation functions which is often used in this situation is the Lagrange interpolator. The Lagrange interpolator is essentially a polynomial which is designed to represent each sample with a function that goes through zero at all other sample points [53].

2.5.1 Keystone interpolation

The resampling operation required by the PFA as derived in section 2.4 is a 2D resampling operation, from the nonuniformly sampled polar raster to a uniform rectangular grid which is the format required for the most efficient FFT routines. 2D resampling requires the use of a 2D interpolating function instead of the 1D function used in equation (2.51), this means that more known sample values contribute to the sum required to determine a desired sample value. The result is a more computationally complex resampling procedure, where N points contributed in the 1D case N^2 points are used for the 2D interpolation. To reduce this computational burden the 2D resampling required by the PFA is often performed by a routine known as keystone interpolation. Keystone interpolation is a two stage routine and gets its name from the shape of the interpolated samples at the intermediate stage.

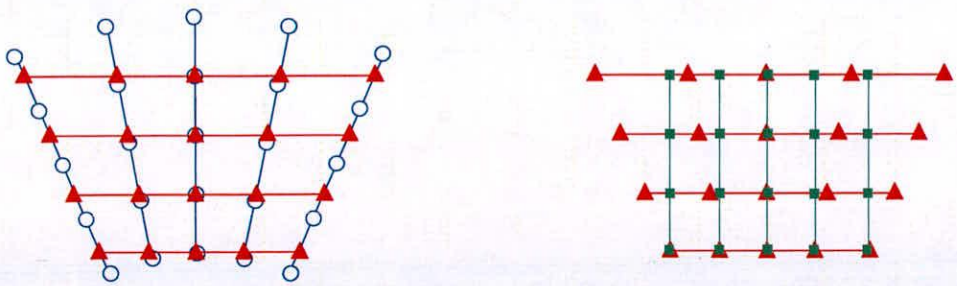

(a) (b)

Figure 2.22: *Keystone interpolation method. (a) Range resampling. (b) Cross range resampling.*

The two stages of keystone interpolation are range resampling and cross range resampling, as illustrated in Figure 2.22. The figure shows the known PFA phase history samples on the polar raster in blue. These samples are then resampled, dealing with only the samples on a given $\mathbf{k}$ vector at a time, in the range direction to the desired sample locations marked in red. These

desired sample locations are found from the intersection of each $\mathbf{k}$ vector with the uniformly spaced in range desired sample grid.

These new samples are then resampled in the cross range direction, again only operating on samples on one constant-range line at a time, to the desired uniform rectangular grid locations marked in green. When resampling in the cross range direction the known samples are nonuniformly distributed, however the assumption is usually made that the samples are at least locally uniform. By performing the resampling as two 1D operations the computational load of the 2D resampling operation is reduced [1, 2].

2.6 Autofocus

Uncompensated nonlinear flight path error, atmospheric distortion error, airframe vibration etc. results in a phase error in the collected SAR data. This phase error is present in the returns from all scatterers and is hence a space invariant error, all scatterers in the imaged scene suffer the same amount of defocus due to the phase error. This is the important difference with the space variant errors that arise as a result of the RVP term in PFA or the uncompensated MTRC error present in the RFA. Since the error is common to all scatterers in the scene, the image can be considered a convolution of the scatterer positions with the space invariant blurring function, $h(n)$.

$$s_\epsilon(k,n) = h(n) \bigotimes s(k,n) \tag{2.52}$$

where

$$h(n) = IFFT_i \left\{ e^{j\phi_\epsilon(i)} \right\} \tag{2.53}$$

where $s_\epsilon(k,n)$ is the image domain data including the phase error function, $s(k,n)$ is the ideal image domain data and $\phi_\epsilon(i)$ is the slow time phase error function in the frequency domain. This results in every scatterer in the scene defocusing, through mainlobe broadening reducing image resolution for low order phase error terms, and as an increase in sidelobe levels which shows in the image as a lack of contrast for higher order phase error terms [1, 2, 54, 55].

Autofocus is a data driven technique that attempts to estimate and remove this uncompensated space invariant phase error, usually by exploiting the image domain data after IFP processing. There are many different methods in the literature to estimate and remove this error of varying complexity. The map drift method discussed in [1, 56] uses the holographic properties of the SAR data to estimate phase errors via sub-aperture image formation with evaluation of the

degree of shift present in the resulting sub-aperture images providing an estimate of the phase error of a given order. Contrast maximisation and entropy minimisation algorithms [57–59] use the assumption that bright isolated scatterers in the scene present the best opportunity to estimate the phase error function, and seek to reduce the energy in the phase error noise signal. However all of these algorithms have deficiencies that lead to a lack of robustness when used on a variety of phase errors and in most cases when there are few bright objects in the image as is typically the case for rural scenes [1, 2].

Phase gradient autofocus (PGA) also uses the fact that the brightest scatterers in the image will have the strongest signal to noise ratio and as a result are the best scatterers to use to form an estimate of the error function. However many bright scatterers in the scene are sought to allow a coherent integration of the phase error estimate from each scatterer, increasing the robustness of the algorithm and reducing the effect of poorly chosen scatterers [60–62]. Therefore if bright isolated scatterers on separate range lines can be selected and appropriately windowed so that noise from other scatterers is not included, circularly rotating these scatterers to the scene centre will remove cross range position dependant phase terms then after inverse Fourier transforming the image in the cross range dimension the phase error function should be all that is present in the data. The gradient of the phase error function is calculated by comparing the phase of consecutive pulses and then coherently summing the result to determine a phase error function estimate.

$$\Delta\phi_\epsilon(i) = \angle \sum_{k=1}^{N} \bar{s_\epsilon}^\star(k, i-1)\bar{s_\epsilon}(k, i) \tag{2.54}$$

$$\hat{\phi}_\epsilon(i) = \sum_{l=2}^{i} \Delta\phi_\epsilon(l) \tag{2.55}$$

with $\phi(1) = 0$. Where $\bar{s_\epsilon}(k, i)$ is the frequency domain data including the phase error and $\bar{s_\epsilon}^\star(k, i-1)$ its complex conjugate, $\hat{\phi}_\epsilon$ is the estimated frequency domain phase error function. This phase error estimate is then removed from the data

$$\bar{s}_c(k, i) = \bar{s}_\epsilon(k, i)e^{-j\hat{\phi}_\epsilon(i)} \tag{2.56}$$

where $\bar{s}_\epsilon(k, i)$ is the frequency domain data including the phase error function and $\bar{s}_c(k, i)$ is the corrected frequency domain data, the data is returned to the image domain via an FFT in the cross range direction.

The fact that the PGA uses the coherent sum of many bright scatterers in the image means that

the quality of the scatterers chosen is actually less important than would be expected, in fact results show that the algorithm performs reasonably well even on rural scenes where there are very few bright point like scatterers, a case which most autofocus algorithms find difficult [1,2].

The scatterer selection, windowing and error estimation and removal procedure is performed iteratively to remove any residual error terms, as the improved focus of the image allows a more accurate selection of appropriate scatterers and windowing, producing a more accurate phase error estimate. A common windowing process is to reduce the window width with every iteration of the algorithm. This iterative procedure is repeated until the estimated phase error is below a predetermined threshold indicating that the image quality is satisfactory. Figure 2.23 shows the steps of the PGA in a flow chart.

However a 'quality' phase gradient algorithm is presented in [63, 64] where the need for the algorithm to be iterative is removed by an initial scatterer screening phase which seeks to determine which scatterers in the scene will result in the best estimate of the phase error function by filtering the choice of scatterers used. Choice of scatterers is based not only on the brightness of the scatterer but the degree of isolation of a scatter's point spread function from those surrounding scatterers. Though this 'quality' PGAs would seem to be more reliant on the presence of either bright or isolated scatterers in the scene, the performance of PGA when this is not the case is one of the algorithms main strengths and is the reason that the PGA is considered the dominant autofocus algorithms in most cases.

PGA has been demonstrated to be applicable to bistatic SAR imagery as well as monostatic SAR [12, 65] . The bistatic PFA presented in [12] performs the necessary resampling operation from the bistatic distorted polar grid to a parallelogram grid, which fills the sampled area of k-space better than the rectangular grid used in the monostatic PFA. This distorts the axes in the image domain so that the bistatic cross range direction is aligned along the x-axis (as it is in the monostatic case), a consequence of this is that the monostatic PGA method of circular shifting individual range lines to remove the linear phase term can be implemented with no changes. Hence the bistatic parallelogram shaped PFA resample grid aligns with the phase error in the k-space domain, this alignment of the resample grid is an important stage in the bistatic PFA.

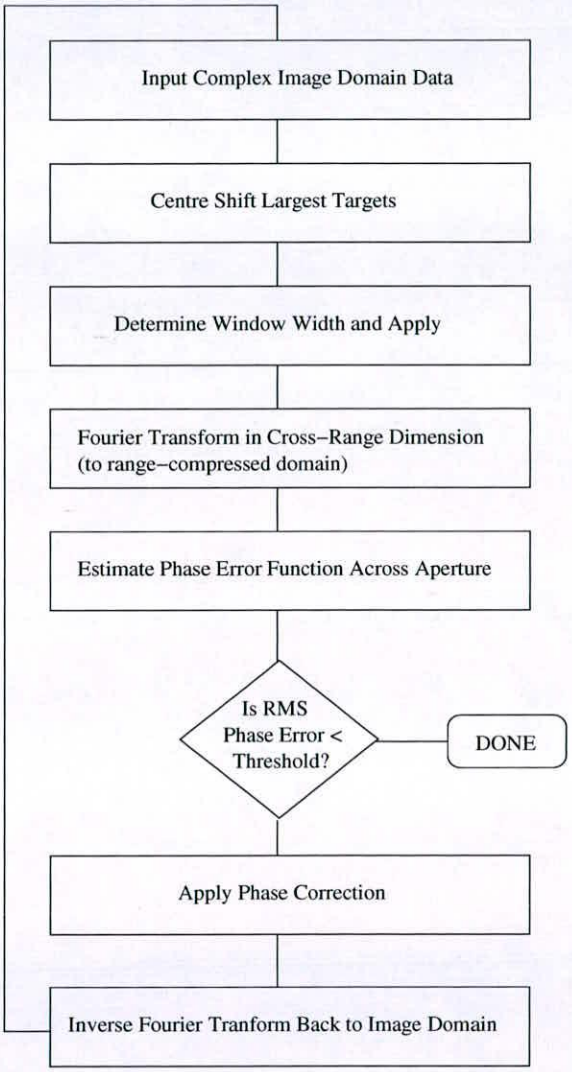

Figure 2.23: *Flow chart describing stages of phase gradient autofocus algorithm [1].*

2.7 Manoeuvring platform

Many of the IFPs discussed in section 2.4 depend upon the assumption that the radar platform traverses a straight and level flight path, transmitting pulses at regular intervals. For example the CBP algorithm is particularly sensitive to the flight path that the radar flies, as this information is used during the signal processing of the algorithm. Often deviations from the straight and level flight path are treated as a source of error and contribute to the image focus problem that autofocus algorithms such as the PGA attempt to ameliorate.

However this straight and level flight path is overly restrictive for applications where contact with an enemy is likely or even possible. In this type of military environment the ability to perform aircraft manoeuvres whilst collecting SAR data would be advantageous and help to increase the survivability of the radar platform. In this scenario the degree of manoeuvre that an aircraft can perform whilst still being able to perform SAR data collection could be a decisive factor in the selection of which IFP algorithm is used.

In the PFA described in section 2.4.2, the flight path followed by the radar platform affects the look direction vector $\mathbf{u}$ and hence the location of the k-space data through the look angle θ as described in equations (2.24) to (2.28). However in the dechirp type processing described the location of the k-space samples along the direction $\mathbf{u}$ doesn't depend on the distance from the scene, instead this distance depends only upon the radar centre frequency. This is because the dechirp reference used for the PFA is a chirp delayed by the scene centre return time $\frac{l_0}{c}$. Therefore the main effect on the area of k-space sampled is through the look direction angle θ, meaning that only the along track position of the radar at each PRI time has a significant bearing on the SAR data collection. This allows processing of data collected from flight paths that are not straight and level with the PFA, provided the actual flight path is known [1, 28, 66, 67].

For the simple case of an accelerating aircraft following a straight and level flight path in the x direction, the sample spacing in the k_x direction will be even more irregular than in the constant velocity case (as illustrated in Figure 2.22). In addition the bandwidth compression that affects bistatic systems, since

$$\hat{\mathbf{u}} = \frac{\hat{\mathbf{u}}_t + \hat{\mathbf{u}}_r}{2} \tag{2.57}$$

will only be a unit vector in the case of the transmitter and receiver look direction vectors being the same, means that the samples in the k_y direction will be irregularly spaced. Thus the resampling operation for a bistatic manoeuvring SAR system is a complex problem.

2.8 Three dimensional imaging

During typical spotlight SAR image collection the area of k-space obtained is a polar arc existing on a 2D plane, this plane of data exists at the slant angle of the flight path. However before image formation this data is commonly projected into the ground plane so that images formed appear similar to an optical image taken from above the scene of interest, as shown in Figure 2.24.

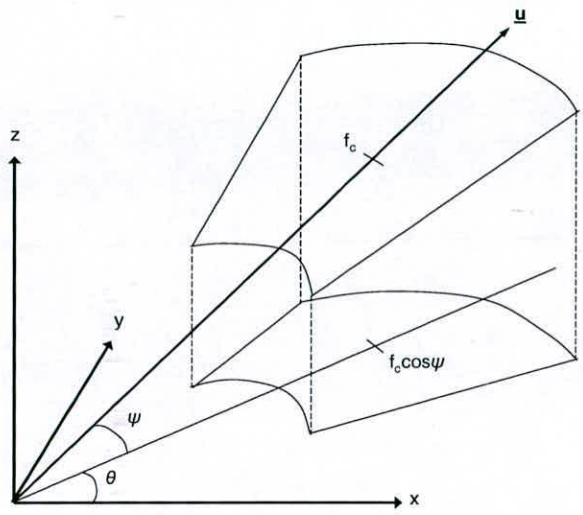

Figure 2.24: *2D polar data collection surface on the slant plane in k-space, which is projected into the image display frame for geometrically correct 2D image formation.*

It is because the SAR data collection surface only exists in two dimensions that the phase history data contains only enough information about the scene to enable images to be formed containing information about the scene in range and azimuth directions. If instead of collecting data on a 2D plane in k-space, a volume of k-space could be sampled then this would contain altitude information about the scene as well [68]. Since we cannot sample a volume of k-space with single pass spotlight SAR systems, methods of sampling more k-space than the simple polar arc on a 2D plane to enable altitude information to be contained in the sampled data are needed. This section shall cover some of the most important techniques for 3D SAR image formation that are present in the open literature.

It is hypothesised that the extra information present in 3D SAR images could allow for improved ATR performance due to the additional resolvable dimension, since it is a commonly

held belief that the performance of ATR algorithms is aided by improving image resolution [69].

2.8.1 Interferometric SAR

Instead of having only a single 2D plane in k-space containing information about a scene of interest, Interferometric SAR (IFSAR) aims to extract altitude information from two independent planes of data. Either a single aircraft with two radar systems (separated in space) is used to obtain two data sets with different slant angles, or a second image is formed of the scene from a second pass(separated in time). These two data sets can each be used to form images of the scene, however each will have different properties due to the different collection geometries. Image domain phase shifts proportional to scene height are present in the data. The object of interferometric SAR is to use only the area of k-space common to both images, then interfere the images to determine altitude or observe changes in the scene between passes. This is essential since only for significantly overlapping apertures can the clutter in the two images be considered coherent [1, 70–72].

Once the two images have been formed using only the section of k-space common to both apertures an additional registration of the images is necessary to ensure that features in the image are in the same locations in both images. This is often performed by identifying features in one image and calculating a mapping function necessary to ensure that the features are correctly positioned in both images.

This can be performed using a similar method to the two-dimensional mapping to be discussed in chapter 3. Coordinates of features present in both images are obtained and then after an affine mapping stage, which removes the offset distance between the images and removes the image rotation, a Volterra series can be used to calculate mapping coefficients of the mapping function used to correct for local image warping. The Volterra mapping coefficients are then used as part of an image domain resampling operation to ensure that both images have data about the same points in the scene, completing the registration process [1].

In these images neighbourhoods of image pixels are then correlated to determine the phase shifts present due to the height of the terrain in the scene. This function is unwrapped to provide the height dependent phase function present in the images, and can then be used to form a three dimensional image of the scene of interest.

2.8.2 Stereo-SAR

Stereo-SAR as discussed in [73,74] is a similar radar mode to IFSAR however rather than being used to generate a full 3D elevation map, as is the case for IFSAR, stereo-SAR is used only to calculate the height of features affected by the layover effect in SAR images.

A scatterer that is raised out of the SAR image plane will have the same return time of flight as other scatterers which lie in the IDF. As a result of the range ambiguity the raised scatterer will appear in the wrong location in SAR images since it lies at the same range as other scatterers in the IDF, the raised scatterer will appear at a point closer to the synthetic aperture than it actually is [1,73,74]. The raised scatterer appears projected onto the IDF in a direction dependent upon the projection illustrated in Figure 2.24. This effect in SAR imagery is termed layover.

As the name suggests, in a similar manner to IFSAR, two different SAR images are used in stereo SAR. However unlike in IFSAR the more different the collection geometries of the two SAR images used in stereo-SAR are the better the technique works [73]. Given that the slant plane is at a different angle for both the SAR images used, the layover effect causes raised scatterers to appear at different places in the two images. Using the additional information as a result of having two observations of the same scene the height of laid over scatterers can be computed. An alternative single pass SAR algorithm for obtaining 3D terrain relief is presented in [75], where a squinted SAR system is considered and the elevation of a target in the scene of interest can be calculated using the Doppler centroid to determine the intersection of the range sphere, Doppler cone and the elevation plane of the radar antenna. This method is proposed as a cheaper alternative to IFSAR since it only requires a single antenna, however the terrain relief retrieved is less accurate and at a lower resolution than achieved in IFSAR.

The fact that the two data collection geometries must be sufficiently different to give an accurate estimate of scatterer height in stereo-SAR places a limit on the applicability of the technique. For instance since bistatic SAR images have shadows, due to the look directions of the transmitter and receiver, the necessity to have different geometries increases the chance that the scatterer of interest will be occluded by shadowing.

2.8.3 SAR 2D aperture synthesis

There are several methods for 3D SAR image formation described in the literature that extend the 2D IFPs described in section 2.4 to the case where the sampled data are a filled 3D volume

of k-space [76–80].

A 3D version of the RMA is presented in [76, 77], where the data is collected from a synthesised 2D planar aperture in [76] and a cylindrical or spherical aperture in [77] using a stepped frequency system to generate the extra dimension of the aperture, where conventional 2D SAR data are collected from a 1D aperture. As per the 2D RMA the image domain resolutions are defined by the radar bandwidth in the range direction and the length of the aperture in the azimuth and vertical azimuth directions.

$$\begin{aligned} \delta_r &= \frac{c}{2B} \\ \delta_{cr} &= \frac{cR_0}{2f_cL_x} \\ \delta_{vcr} &= \frac{cR_0}{2f_cL_z} \end{aligned} \tag{2.58}$$

where L_x and L_z are the lengths of the synthetic aperture in the x and z directions and δ_{vcr} is the resolution in the vertical cross-range (or vertical azimuth) direction.

The 3D RMA follows the same structure to the 2D RMA, with the 1D operations extended to 2D:

1. 2D azimuth FFT in the x-z direction
2. 2D matched filter in the range - cross range directions
3. Stolt interpolation in the range direction
4. 3D IFFT to form image.

However as with the 2D RMA, since the algorithm takes chirped data in the azimuth and vertical azimuth directions as its input the high sample rate required would lead to even larger data sets than in the 2D case using this IFP.

A 3D polar processing algorithm for ISAR is presented in [78]. This algorithm operates on ISAR data collected over many different slant angles, in this way it is the same as conventional SAR collected with a 2D flight path. This results in a filled 3D sampled area of k-space where the samples lie on several of the collection planes shown in Figure 2.24. Since the resolution achievable when using the PFA depends upon the extent of the area of k-space sampled in both the range and azimuth directions, for this 3D application of the PFA the resolutions achievable

are demonstrated to be dependent on the extent of the 3D volume of data in k-space in the range, azimuth and vertical azimuth directions.

Before a 3D IFFT is used to form the 3D image the data is resampled as is necessary for the 2D PFA. To implement the resampling the polar data on each slant plane is resampled using the 2D keystone resampling method described in section 2.5.1. Once the data lies on a uniform grid on each slant plane a resampling is performed in the k_z direction to provide data on a regularly spaced 3D rectangular grid. As with the 2D version of the PFA this method provides a computationally efficient method for 3D SAR image formation limited however by the plane wave approximation.

A system overview and simulation results for the ARTINO (airborne radar for three-dimensional imaging and nadir observation) system developed at FGAN-FHR (research establishment of applied science - research institute for high frequency physics and radar techniques) are presented in [81, 82]. The ARTINO system uses multiple transmit and receive elements spaced linearly along the UAV platform wing span. The radar system flies over the scene of interest and is capable of forming high resolution (approx. 20 cm) SAR images including height information about targets out of the ground plane. The simulation results presented demonstrate the concept and achieved image resolutions.

2.8.4 Curvilinear SAR

Rather than require samples from a full volume of k-space from a 2D synthesised aperture, algorithms are present in the literature that discuss 3D SAR image formation from single pass SAR systems [4,83–88]. Using conventional single frequency SAR systems it is not possible to sample a full volume of k-space using single pass spotlight SAR. However since the resolution of an image in range and azimuth depends upon the extent of the sampled area of k-space in the k_x and k_y directions, a 3D SAR image could be formed from a curved flight path. This is termed curvilinear SAR in the literature. This type of manoeuvre would sample a 2D surface of data points in the k-domain, with extent in all three dimensions. Since an aperture like this has extent in the k_z direction it should be possible to form a 3D SAR image from data collected when following a curvilinear flight path.

In [83] Knaell presents results from application of the CLEAN spectral estimation and maximum likelihood estimation techniques to data collected from curvilinear apertures. The aper-

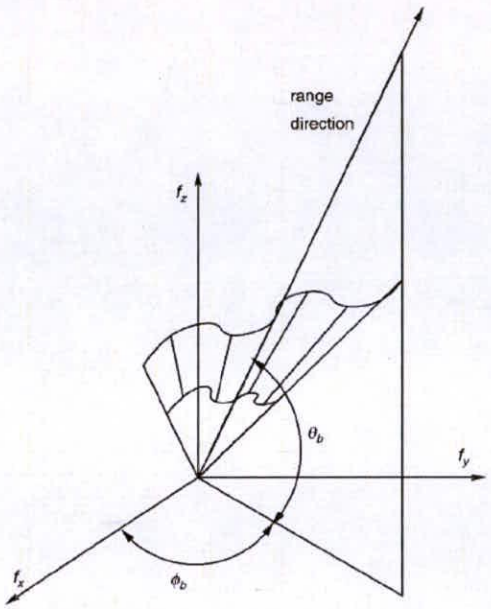

Figure 2.25: *2D surface of sampled k-space by manoeuvring aircraft, from [4].*

tures considered vary from circular, parabolic to sinewave shaped data collection apertures. The results presented demonstrate that the curvilinear apertures considered preserve enough of the 3D information about the target scene to be used for 3D SAR imaging applications. However, high scatterer sidelobes due to the synthetic aperture shape are highlighted as a problem.

The use of Fourier methods for 3D target feature extraction is presented in [85]. The resolution and sidelobe levels of targets in a SAR image are shown to be dependent upon the synthetic aperture shape. Li considers the performance of FFT based image formation from orthogonal apertures to demonstrate poor sidelobe performance of the Fourier image reconstruction when compared to data collected from a full 2D aperture. The RELAX parameter estimation method is then used to extract the target features in the curvilinear SAR system.

A non-iterative parametric imaging algorithm for curvilinear SAR is presented in [86, 87]. The algorithm derived is based on using the MUSIC spectral estimation technique in the range and cross range directions successively. This sequential approach reduces the order of the nonlinear optimisation process reducing the computation cost of the algorithm. The sequential estimation is possible due to a decoupling of the range and cross range parameter which is valid for small target scenes at large stand of ranges. The results presented demonstrate lower target sidelobe levels in 3D SAR images formed using the algorithm than for images formed using a 3D FFT

directly. Simulation results presented in [88] demonstrate the performance of the algorithm for flight paths with linear and random aperture errors, the results show that the target location estimate has a slight error however the target point spread function is significantly improved when compared to the AUTORELAX algorithm. This improvement in performance makes the algorithm discussed more robust to flight path errors than other parametric image formation algorithms discussed in the literature.

A method for reducing the high sidelobe levels in SAR images from sparsely sample aperture, such as in curvilinear SAR is presented in [89]. Robust Capon beamforming (RCB) is used to suppress the high sidelobe levels for targets image from curvilinear SAR apertures as demonstrated in [85]. The sparsely sampled phase history data chieved using curvilinear SAR is shifted to the zeros in the azimuth and elevation directions by applying a phase compensation term, this removes the coupling between the range and azimuth / elevation parameters. The sample covariance matrix is calculated for samples with the same range frequency and then used in the non-parametric RCB spectral estimation method. Simulation results demonstrating this RCB-based 3D SAR imaging method show that it reduces the high target sidelobes present in images formed using the FFT.

The achievable resolution for the filled k-space volume 3D SAR system is dependent upon the extent of the area of k-space in each of the k_x, k_y and k_z directions. Therefore the optimal curved flight path that should be followed to maximise the resolutions achievable for curvilinear 3D SAR is examined in [4]. Image formation is performed using a CBP algorithm and simulated results are presented. This demonstrates that it is possible to form 3D SAR images from a single pass 3D curved flight path using CBP. However the computational cost associated with CBP, which scales badly with scene size plus the extension of the image to three dimensions, motivates consideration of alternative image formation algorithms.

If data collected following an out-of-plane nonlinear flight path were projected into the ground plane and a 2D SAR image formed in the conventional way, using PFA for instance, then an uncompensated quadratic phase error corresponding to the curvature of the flight path would blur the image. The amount of defocus experienced is determined by the amount of out-of-plane motion form the radar platform. It is suggested in [4] that autofocus could be used to measure the quadratic phase error and hence estimate the target height, however it states that layover from other targets at the same range and different heights may prevent accurate height estimation. Layover is the effect in SAR images where targets with height out of the ground

plane appear at the same position as targets on the ground plane which have the same range to the radar. Hence two targets in physically different positions can both contribute to the same resolution cell due to the layover effect.

The optimal flight path to be followed for curvilinear SAR is also considered in [90] where a feature-independent aperture evaluator is derived. By minimising this index, the azimuth and elevation flight path parameters necessary to optimise target location estimation accuracy using parametric methods are obtained.

3D SAR image formation based on the assumption that the number of scattering centres in a scene is sparse, ie. that it is small compared to the number of pixels in the 3D SAR image is presented in [91]. The algorithm presented forms sub-images using small areas of k-space collected from a nonlinear flight path using a sparse image reconstruction method. These sub-images are noncoherently summed to ensure that the resulting image contains the non-persistent scattering centres from multiple polarizations from all the sub-images. The algorithm presented is compared to image formation using the FFT on the sparsely sample 3D SAR phase history data. The simulation results presented show that the algorithm presented demonstrates improved sidelobe performance.

The extension of curvilinear SAR from the spotlight mode to a new 'composite mode' curvilinear SAR (CCLSAR) is presented in [92]. This algorithm is developed to allow use of curvilinear SAR over large ground areas with faster mapping rates than in conventional spotlight curvilinear SAR, in much the same way as strip-map SAR offers faster mapping rates than spot-light SAR. The algorithm operates in strip-map mode in the azimuth direction and in the spotlight mode in the elevation direction. Hence the radar platform travels in a sinusoidal pattern in the x-z plane along a linear path in the x-y plane, while the radar beam is steered to follow the straight line path on the ground as in strip-map mode SAR. Simulation results are presented demonstrating the achievable resolutions in all three dimensions, these results shown that the CCLSAR mode is capable of forming 3D SAR images with comparable resolutions in azimuth and elevation and claims to achieve better elevation than using IFSAR.

2.9 Summary

This chapter has provided an introduction to radar signal processing and the resolutions achievable in traditional radar systems. Chirped signals were introduced to demonstrate the improved

range resolution that can be achieved using coded waveforms. The concept of synthetic aperture radar was introduced and the improved azimuth resolution when compared to traditional radar systems was described. Several modes of SAR operation were described, including bistatic SAR, along with a mathematical model of the spotlight bistatic SAR geometry. The main SAR IFP algorithms presented in the literature were described along with the advantages and constraints relevant to each, particular attention was paid to the PFA as it will be used throughout the work presented in the rest of the thesis.

A brief description of the principles and mathematics of sampled data systems and the resampling process of interpolation were presented. Keystone resampling the commonly used approximation to the 2D resampling required when using the PFA SAR IFP was described. The dominant data driven autofocus algorithm for correction of image domain blurring, due to phase errors from inaccurate measurement of aircraft position or atmospheric distortion, PGA was presented. The challenges and advantages presented by manoeuvres performed by the radar platform during the SAR data collection period were discussed.

The limitation imposed by the traditional SAR data collection geometry on the ability to form 3D SAR images was presented. The main methods for forming 3D SAR images presented in the literature were presented, including the extension of some of the 2D IFPs to the 3D SAR problem using 2D synthesised apertures. In addition methods for forming 3D SAR images from single pass data collection geometries were discussed.

This should place the contents of this thesis into context and establish the novelty of the work presented, along with providing the necessary theory to enable someone unfamiliar with SAR to understand the contents of the remaining chapters.

Chapter 3
Two Dimensional Mapping Methods

3.1 Introduction

When implementing the polar format algorithm (PFA) a resampling operation from a polar raster to a regular rectangular grid is required before the collected radar data can be transformed using the fast Fourier transform (FFT) into the image domain. This resampling operation is often performed by the keystone method, where the 2D resampling required is approximated as two separable 1D resampling operations [1, 2, 12].

This chapter presents an alternative method of performing this interpolation where the phase history data on a polar raster is mapped to a different domain in which the interpolation is simpler. The sample points are uniquely mapped to a domain where the necessary 2D resampling operation is separable into two distinct 1D resampling operations, and the sample points are unit spaced to allow the same interpolation basis function to be used at all sample positions. In this domain designing a 2D window to fit the data is also simpler. There are many different ways to perform this mapping operation, this chapter covers three methods: Volterra series based mapping, analytic mapping and a semi-analytic mapping method, as well as describing two ways of implementing the interpolation.

The general method for the nonlinear mapping techniques presented in this chapter is to map the k-space sample locations to a uniform rectangular grid. As a result of the spotlight bistatic SAR data collection process we have a set of k-space sample points $\{\mathbf{k}_i\}_{i=0}^{N-1}$, where $\mathbf{k} = [k_x k_y]^T$, on an irregular distorted polar grid as defined by the PFA in equations (2.24 - 2.28). In order to allow the 2D resampling operation, required by the PFA, to be separable into two 1D resampling operations we seek a nonlinear mapping function to a regular rectangular grid. The target grid is chosen to be uniform and integer spaced for simplicity, $\{\mathbf{k'}_i\}_{i=0}^{N-1}$ where $\mathbf{k'} = [k'_x k'_y]^T$. Each point in the original sample grid maps to a point in the new domain.

$$\mathbf{k'} = \mathbf{f}(\mathbf{k}) \tag{3.1}$$

where $\mathbf{f}(\cdot)$ is the nonlinear mapping function. In this domain selecting a single interpolation function, which goes through zero at all other known values, for all points in the data set should be possible where in the data collection domain this is not the case due to the irregular spacing of samples on the distorted polar raster.

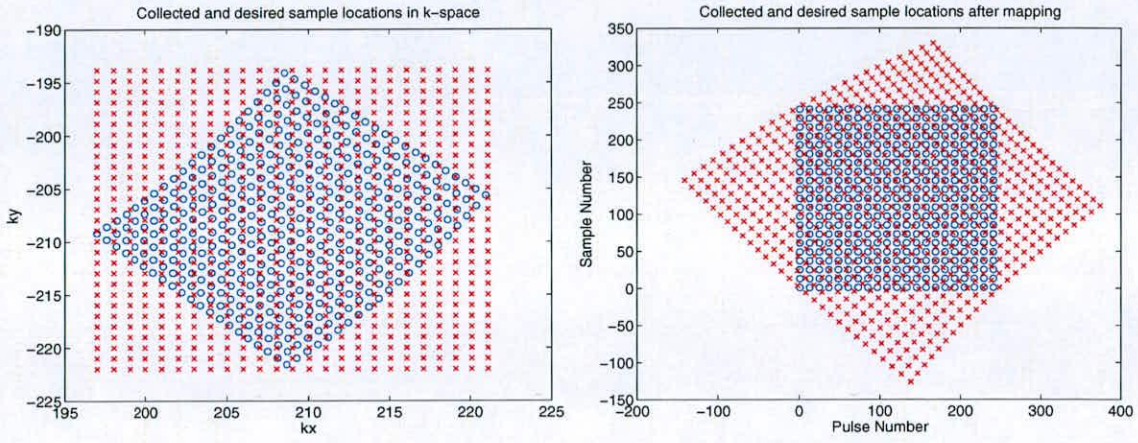

(a) (b)

Figure 3.1: *Sample and desired locations, (a) before and (b) after mapping.*

Figure 3.1 illustrates this process, the k-space locations of the phase history samples are shown in Figure 3.1(a) as blue circles lying on the polar raster shape with the samples on each pulse lying on a straight line in this case at approximately 45^o. The desired sample positions for use in the FFT, shown as red crosses, form a regular rectangular region surrounding the sampled phase history.

The method of selecting these desired sample locations chosen for the results presented in this chapter is to determine the maximum sample density in both the k_x and k_y directions of the collected data samples. The desired grid is then simply a rectangular region encompassing the collected data points, with the sample spacing matching the sample densities already determined. However this method is not the only suitable method of selecting the desired sample locations, the mapping methods presented in the following chapter could just as easily be implemented for a desired sample grid chosen by other means. For instance in [12] it is demonstrated that the result of bistatic PFA image formation can be focused using the PGA algorithm, provided that the PFA interpolation is performed to a parallelogram shaped grid where the principle axis is in the direction given by half the bistatic angle, β. Therefore in practice it may be preferable to select a different desired sample grid than that used in this chapter, however for simplicity and ease of understanding a rectangular grid encompassing all the collected data points shall be

used throughout this chapter.

After determining the mapping function required to map the known sample positions to a regular rectangular grid, the desired samples are mapped to the same domain. This is shown in Figure 3.1(b) where the known phase history sample locations (blue) now lie on a regular integer spaced rectangular grid, the axes on this plot show that the sample positions now range from 1 to N_p the number of pulses and from 1 to N_s the number of samples. The desired samples (red) have been mapped to the same domain and now no longer lie on the original regularly spaced grid, the desired sample grid has been rotated and distorted and the sample spacing is irregular in both dimensions because of the mapping. The interpolation process is performed in this domain.

The rest of the chapter is organised as follows, three mapping methods developed are presented and demonstrated through simulation results, the advantages of each method is discussed. Two different approaches to performing the interpolation will be presented and demonstrated, the relative merits of each is discussed before the performance of the overall mapping and interpolation process is compared to the performance achievable using the keystone interpolation method on simulated manoeuvring platform bistatic SAR data.

3.2 Volterra series mapping

As discussed in the previous section, the general method for the nonlinear mapping techniques is to map the k-space sample locations to a uniform rectangular grid. We have a set of k-space sample points $\{\mathbf{k}_i\}_{i=0}^{N-1}$, where $\mathbf{k} = [k_x k_y]^T$, on an irregular distorted polar grid. We require a nonlinear mapping function, $\mathbf{f}(\cdot)$, to a regular rectangular grid;

$$\mathbf{k}' = \mathbf{f}(\mathbf{k}) \tag{3.2}$$

One method for finding this nonlinear mapping function is to use a Volterra series.As discussed in section 2.8.1 a Volterra series can be used to approximate a general mapping function, and can be used to map identical features in two SAR images to the same position as part of the image registration problem in IFSAR. A second order Volterra series, described here for illustrative purposes;

$$k_x' = a + a_0 k_x + a_1 k_y + a_{00} k_x^2 + a_{01} k_x k_y + a_{11}^2 k_y^2 \ldots \tag{3.3}$$

$$k'_y = b + b_0 k_x + b_1 k_y + b_{00} k_x^2 + b_{01} k_x k_y + b_{11}^2 k_y^2 \ldots \tag{3.4}$$

can be written in matrix form. The target grid is chosen to be uniform and integer spaced for simplicity, $\{\mathbf{k'}_i\}_{i=0}^{N-1}$ where $\mathbf{k'} = [k'_x k'_y]^T$. Each point in the original sample grid maps to a point in the new domain, therefore for each point we write equations (3.3) and (3.4) for the Volterra series mapping the k-space to the uniform grid.

$$\begin{bmatrix} \mathbf{k'_1} \\ \mathbf{k'_2} \\ \vdots \\ \mathbf{k'_n} \end{bmatrix} = \begin{bmatrix} 1 & k_{x1} & k_{y1} & k_{x1}^2 & k_{x1}k_{y1} & k_{y1}^2 \\ 1 & k_{x2} & k_{y2} & k_{x2}^2 & k_{x2}k_{y2} & k_{y2}^2 \\ & & & \vdots & & \\ 1 & k_{xn} & k_{yn} & k_{xn}^2 & k_{xn}k_{yn} & k_{yn}^2 \end{bmatrix} \begin{bmatrix} a \\ a_0 \\ a_1 \\ a_{00} \\ a_{01} \\ a_{11} \end{bmatrix}$$

Each of these equations has six unknowns however since (in general) we have many points (ie. $N > 6$) we cannot therefore find an exact solution. Instead we must aim for a least-squares solution, which gives the mapping coefficients, $\mathbf{a}$, required to map the sample locations to the desired grid as

$$\mathbf{k'} = \mathbf{K}.\mathbf{a} \tag{3.5}$$

$$\mathbf{a} = \left[\mathbf{K^T K}\right]^{-1} \mathbf{K^T k'} \tag{3.6}$$

These coefficients are then used to map the desired grid to the same space. Once this mapping has been performed the interpolation can be performed in this domain with the advantages described previously. Although this method is capable of mapping the sample grid to the desired locations, to reduce the computation time only up to third order terms have been retained in the Volterra series. This means that the mapping performed is not as accurate as could be achieved using this method. To compensate a linear mapping is performed prior to the nonlinear mapping.

$$\mathbf{k'}_{affine} = \mathbf{s} + \mathbf{T}\mathbf{k} \tag{3.7}$$

A linear mapping can be found by principle component analysis (PCA) and independent component analysis (ICA). PCA is a decomposition of the matrix $\mathbf{T}$ into a diagonal scaling matrix

$\mathbf{\Lambda}$ and a unitary rotation/reflection matrix $\mathbf{V}$

$$\mathbf{k'}_{affine} = \mathbf{s} + \mathbf{T}\mathbf{k} \tag{3.8}$$

$$= \mathbf{s} + \mathbf{V}\mathbf{\Lambda}^{-1}\mathbf{k} \tag{3.9}$$

PCA can be seen as a combination of shift s, stretch $\mathbf{\Lambda}^{-1}$ and rotate/reflect $\mathbf{V}$. To calculate this linear map compute the mean;

$$\mathbf{m} = \frac{1}{N}\sum_{i=0}^{N-1}\mathbf{k}_i \tag{3.10}$$

and the covariance;

$$\mathbf{C} = \frac{1}{N}\sum_{i=0}^{N-1}(\mathbf{k}_i - \mathbf{m})(\mathbf{k}_i - \mathbf{m})^T \tag{3.11}$$

Eigenvalue decomposition (Principle Component Analysis) then provides the scaling and rotation elements;

$$\mathbf{C} = \mathbf{V}\mathbf{\Lambda}\mathbf{V}^T \tag{3.12}$$

A final rotation matrix can be implemented to rotate the image by the mid-pulse angle. This linear mapping procedure rotates and shifts the k-space samples to a shape similar to that obtained when performing monostatic broadside SAR imaging, this limits the complexity of the problem that the Volterra series is used to solve, therefore improving the quality of the map while only using lower order terms in the series.

Therefore the mapping operation using the Volterra mapping algorithm consists of performing a linear (or affine) mapping of the known k-space samples and the desired sample grid, then these sample locations are used as the input to the Volterra mapping stage which completes the mapping. The interpolation required by the PFA is then performed in this mapped space. Therefore equation 3.2 can be rewritten as a two stage process as follows;

$$\mathbf{k'}_{affine} = \mathbf{f}(\mathbf{k}) \tag{3.13}$$

$$\mathbf{k'} = \mathbf{f}(\mathbf{k'}_{affine}) \tag{3.14}$$

3.2.1 Results

The Volterra series based mapping method was implemented as a MATLAB simulation and has been tested for a variety of system geometries. The mapping stages are illustrated in Figure

3.2 for a bistatic SAR system with approximately 60^o bistatic angle and approximately 1m resolution. Figure 3.2(a) shows the collected and desired sample grids in k-space, where the collected phase history samples are shown in blue lying on the distorted bistatic polar raster and the desired sample positions for use in the PFA image formation FFT form an integer spaced regular rectangular grid surrounding the known samples.

Figure 3.2(b) shows these sample points after the initial affine mapping stage, the axes show that these points are in the affine mapped space, where the collected phase history samples have been rotated to lie on the k_y-axis. The outline of the known sample grid appears approximately rectangular, due to the linear mapping's rotation and scaling operations which have removed the mean and covariance of the samples. However the bistatic distortion of the sample grid has not been removed so the blue sample grid is not quite rectangular, the slight curvature of the grid can be seen on the left and right hand edges. The effect of the affine mapping can also be seen looking at the desired sample positions (red).

The bistatic distortion seen on the known sample grid in Figure 3.2(b) is removed by the Volterra series mapping operation and the final collected samples can be seen to lie on a unit spaced rectangular grid in Figure 3.2(c). The figure axes show that the sample points are now in the mapped space where the interpolation will be performed. The mapped phase history sample points (blue) range from 1 to N_p, the number of pulses, in the k_x direction and from 1 to N_s, the number of samples on each pulse, in the k_y direction. The effect of the final mapping stage can also be seen on the desired sample grid (red) which now appears less rectangular.

It can be seen from these results that the initial linear mapping stage the collected (blue) sample points have been rotated to lie on the k_y axis and their outline appears approximately rectangular, due to the linear mapping's rotation and scaling operations. However the bistatic distortion of the sample grid has not been removed, this happens during the Volterra series mapping operation and the final collected samples can be seen to lie on a unit spaced rectangular grid. The effect of the final mapping stage can also be seen on the desired sample grid which now has a more irregular appearance.

The rms error introduced as a result of the mapping process can be calculated by:

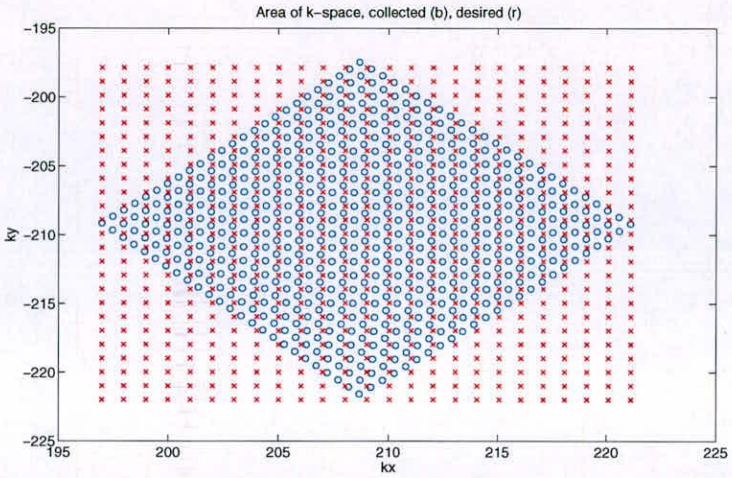

(a)

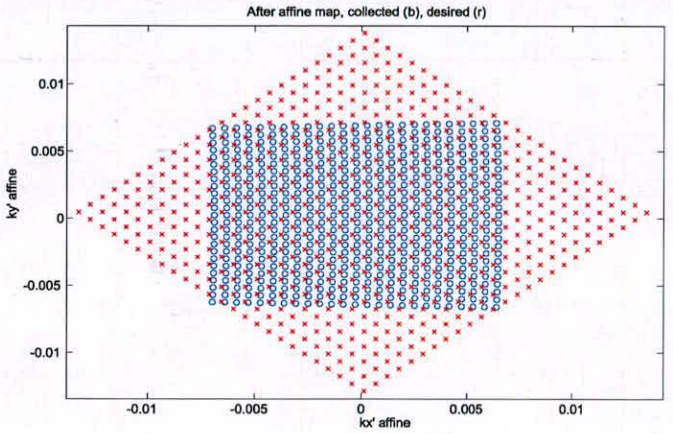

(b)

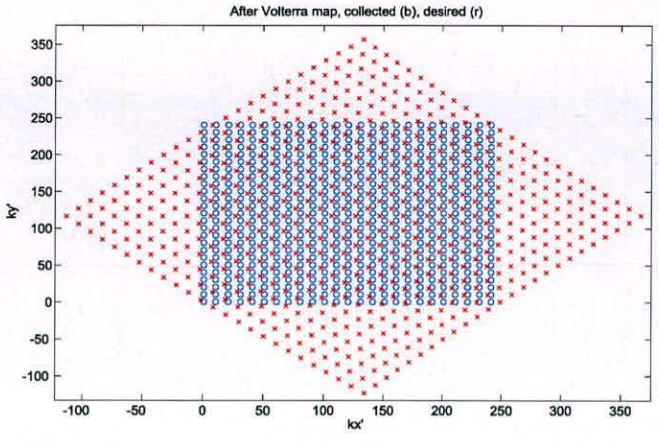

(c)

Figure 3.2: *Sample and desired locations (a) before mapping, (b) after linear mapping and (c) after nonlinear Volterra mapping.*

$$error = \sum_{M}\sum_{N} \mathbf{k'}_{ij} - \bar{\mathbf{k}_{ij}}$$
$$error_{rms} = \sqrt{\frac{error}{NM}} \tag{3.15}$$

where $\mathbf{k'}_{ij}$ is the target grid and $\bar{\mathbf{k}_{ij}}$ is the actual mapped grid. The rms error provides a measure of the accuracy of the mapping operation, it represents the average distance of the mapped points from their desired position.

For the example shown in Figure 3.2, $error_{rms}$ = 3.2874 x 10^{-4}. This represents 3/1000ths of the desired sample spacing. This rms error can be compared to the error in the keystone interpolation method where the assumption of local uniformity of the samples during the azimuth resampling process is made. For typical parameters of a 1m resolution SAR system operating in the X-band at a stand-off range of 20km, the error in this assumption during the keystone resampling is approximately 4.0525 x 10^{-6}. However this is only for the non-manoeuvring platform case, for the manoeuvring case this approximation will become increasingly inaccurate, for instance the rms error for the keystone resampling is approximately 5.8778 x 10^{-3} for 10 ms^{-2} along-track acceleration.

The rms error calculated after the mapping procedure is completed may be used to determine if the Volterra series used to perform the mapping was of a high enough order, allowing a recalculation of the mapping coefficients using a higher order Volterra series if an unsatisfactory level of accuracy is achieved by the Volterra mapping.

3.2.2 Discussion

The Volterra series mapping method has been demonstrated to perform a mapping of the collected bistatic SAR data sample points to a regular rectangular target grid. Using the mapping coefficients calculated during this process the desired sample points, for use in SAR image formation via the FFT, are mapped to the same domain. The results presented indicate that for bistatic PFA sample grids a third order Volterra series provides an accurate mapping method.

The Volterra series provides a general method for mapping any sample grid regardless of it's

complexity, to the desired grid. Using the Volterra series it is theoretically possible to map any grid onto a regular rectangular grid provided enough terms in the Volterra series are retained. To this end the mapping operation can be made to be self-calibrating, using a measure of mapping performance such as the rms error to determine if higher order terms are required.

However in the SAR application the collected sample grid has limited complexity. The samples on a given pulse must lie on a straight line in k-space for example, where the Volterra method is able to cope with a grid without this restriction. The Volterra series mapping method provides a greater flexibility than is required by the problem it is being applied to, therefore it should be possible to use this limited complexity to perform the mapping with a simpler mapping function, this idea will be developed further in the next two sections of this chapter.

3.3 Analytic mapping

The second method of performing the mapping operation is based on the observation that the equations used to define the phase history sample locations in k-space are performing a mapping. Before the position of the samples in k-space are determined a particular sample can be considered defined by which radar pulse the sample belongs to and its position in the fast time samples of that pulse. At this point the pulse number and fast time sample number can be considered the indices of a matrix, with each pulse a separate row in the matrix. The samples are then mapped onto the polar grid to determine their position in k-space. The samples of the collected bistatic SAR data are located in k-space on a distorted polar raster given by;

$$\mathbf{k} = \omega\left(\frac{\hat{\mathbf{u}}_\mathbf{t} + \hat{\mathbf{u}}_\mathbf{r}}{2}\right) \tag{3.16}$$

where

$$\omega(t,\hat{t}) = \frac{4\pi}{c}\left[f_c + 2\mu\left(\hat{t} - \left(\frac{r_{0t}(t) + r_{0r}(t)}{c}\right)\right)\right] \tag{3.17}$$

where $\mathbf{k}$ is the sample location in k-space, $\hat{\mathbf{u}}_t$ is the unit vector in the direction of the transmit platform from the scene centre, $\hat{\mathbf{u}}_r$ is the unit vector in the direction of the receive platform from the scene centre, f_c is the radar centre frequency, μ is the the chirp rate, r_{0t} and r_{0r} are the ranges from the transmit and receive platforms to the scene centre respectively, t is the slow time variable and $\hat{t}$ is the fast time variable [1, 2, 12].

By recognising that the phase history data samples can be considered as matrix elements or points on a regular rectangular grid, before being mapped to their position in k-space, then this mapping can be analytically inverted to determine the position of the desired samples in the domain that the interpolation is performed in. However this inversion is only likely to be possible for simple flight paths, so to begin with a bistatic system with linearly accelerating transmit and receive platforms shall be considered. This can be represented as

$$\begin{aligned}\mathbf{x}_t &= \mathbf{x}_{t0} + \mathbf{v}_t((i-1)PRI) + \frac{1}{2}\mathbf{a}_t((i-1)PRI)^2 \\ \mathbf{x}_r &= \mathbf{x}_{r0} + \mathbf{v}_r((i-1)PRI) + \frac{1}{2}\mathbf{a}_r((i-1)PRI)^2\end{aligned} \tag{3.18}$$

where $\mathbf{x}_t$ is the position of the transmit platform, $\mathbf{x}_{t0}$ is its initial position, $\mathbf{v}_t$ is the velocity of the transmit platform and $\mathbf{a}_t$ is its acceleration (similarly for the receive platform $\mathbf{x}_r$ etc), i is the pulse number in the SAR data collection period and PRI is the pulse repetition interval.

$$t = (i-1)PRI \tag{3.19}$$

$$\tan(\theta) = \frac{k_x}{k_y}$$

$$\Rightarrow \tan(\theta) = \frac{(x_{t0x} + v_{tx}t + \frac{1}{2}a_{tx}t^2) + (x_{r0x} + v_{rx}t + \frac{1}{2}a_{rx}t^2)}{(x_{t0y} + v_{ty}t + \frac{1}{2}a_{ty}t^2) + (x_{r0y} + v_{ry}t + \frac{1}{2}a_{ry}t^2)} \tag{3.20}$$

where θ is the bistatic look angle. After cross multiplication and grouping of terms of the same order

$$\begin{aligned}\frac{1}{2}\left[(a_{tx} + a_{rx}) + \frac{k_x}{k_y}(a_{ty} + a_{ry})\right]t^2 + \left[(v_{tx} + v_{rx}) + \frac{k_x}{k_y}(v_{ty} + v_{ry})\right]t \\ + \left[(x_{tx} + x_{rx}) + \frac{k_x}{k_y}(x_{ty} + x_{ry})\right] = 0\end{aligned} \tag{3.21}$$

which can be solved for i using

$$t = \frac{-B \pm \sqrt{(B^2 - 4AC)}}{2A}$$

where

$$\begin{aligned} A &= \frac{1}{2}\left[(a_{tx}+a_{rx})+\frac{k_x}{k_y}(a_{ty}+a_{ry})\right] \\ B &= \left[(v_{tx}+v_{rx})+\frac{k_x}{k_y}(v_{ty}+v_{ry})\right] \\ C &= \left[(x_{tx}+x_{rx})+\frac{k_x}{k_y}(x_{ty}+x_{ry})\right] \end{aligned} \tag{3.22}$$

More typically given that for SAR a straight and level flight path is used, we could assume no accelerations and calculate t using

$$t = \frac{-\left[(x_{tx}+x_{rx})+\frac{k_x}{k_y}(x_{ty}+x_{ry})\right]}{\left[(v_{tx}+v_{rx})+\frac{k_x}{k_y}(v_{ty}+v_{ry})\right]} \tag{3.23}$$

to calculate a noninteger pulse number i for the desired samples. Then using

$$\mathbf{x}_{tnew} = \mathbf{x}_{t0} + \mathbf{v}_t(i_{new}-1)PRI + \frac{1}{2}\mathbf{a}_t((i_{new}-1)PRI)^2 \tag{3.24}$$

where $\mathbf{x}_{tnew}$ is the location of the transmit platform relating to the noninteger pulse number i_{new}, a similar result can be written for the receive platform.

$$|\mathbf{u}| = \sqrt{\left(\frac{\hat{\mathbf{u}}_t+\hat{\mathbf{u}}_r}{2}\right)^2} \tag{3.25}$$

where

$$\begin{aligned} \hat{\mathbf{u}}_t &= \frac{x_t}{|x_t|} \\ \hat{\mathbf{u}}_r &= \frac{x_r}{|x_r|} \end{aligned} \tag{3.26}$$

are the unit vectors in the direction of the transmit and receive platforms respectively, this gives

$$\omega = \frac{|\mathbf{k}|}{|\mathbf{u}|}$$

$$\omega = \frac{\sqrt{k_{xi}^2+k_{yi}^2}}{|\mathbf{u}|} \tag{3.27}$$

$$\Rightarrow j = f_s \left[\frac{1}{4\pi\mu} \left(\frac{\omega c}{2} - 2\pi f_c \right) + \frac{T_p}{2} + \frac{D}{c} \right] \tag{3.28}$$

where the size of the scene being imaged is D metres in both x and y directions.

Equations (3.21) and (3.28) give the necessary equations to exactly map the known sample locations in $[k_x, k_y]$ to the integer spaced regular rectangular grid given by $[i, j]$, and using the same equations the desired sample locations necessary for use of the FFT can be mapped to the same domain.

3.3.1 Results

The result of implementing this mapping method on the same 1m resolution, 60^o bistatic angle simulated SAR data set used to demonstrate the Volterra series mapping is shown in Figure 3.3. Again the result of the mapping can easily be seen, the known sample points lying on a regular rectangular grid and the desired samples mapped to an irregular grid.

The rms error of the mapping operation was calculated in the same manner as before and for the analytic mapping operation illustrated in Figure 3.3, $error_{rms}$ =3.7208 x 10^{-13}. Since the analytic inversion is an exact mathematical inversion of the original mapping function this error figure represents the arithmetic rounding error from the simulation process.

3.3.2 Discussion

An analytic inversion of the implicit mapping operation used to calculate the sample positions of SAR data sets has been derived. Simulation results demonstrate that this is an accurate method for performing the mapping operation.

In addition to this, performing the mapping in this way is a more tailored solution to the SAR interpolation problem than the Volterra mapping method, since it exploits the inherent structure of the problem. The known sample positions all lie equally spaced along a limited number of radial lines, with an additional scaling of the sample spacing which varies for each radial line. Using this structure allows for very accurate mapping of the sample positions, as demonstrated by the calculated rms error presented.

However the derivation presented in this section only considers a constantly accelerating platform. If a variable acceleration or some other irregularity was included in the data then this

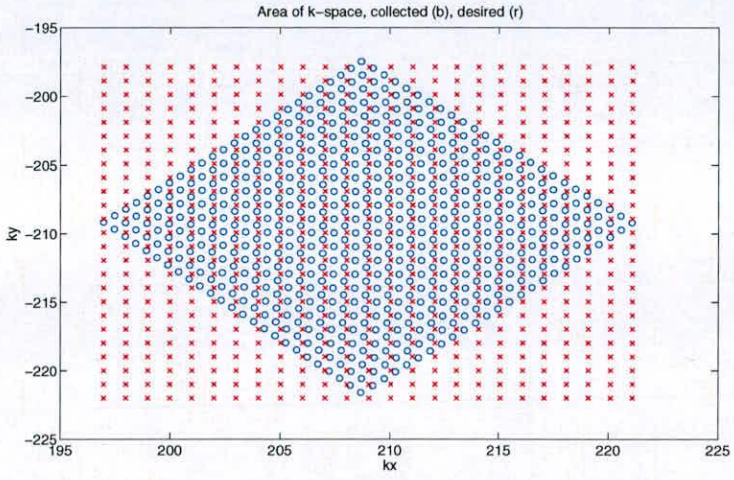

(a)

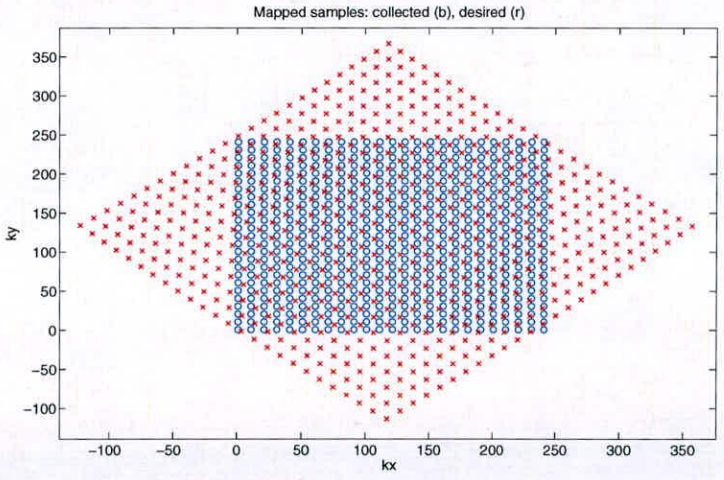

(b)

Figure 3.3: *Sample and desired locations (a) before mapping and (b) after analytic mapping operation.*

analytic inversion needs to be performed for even higher order terms, it would then become very difficult to perform an analytic inversion simply due to the mathematical complexity that it would create. Since the application considered for this task is SAR imaging and it is known that many SAR systems employ complex pulse repetition sequences (known as 'pulse jitter') and with a varying radar centre frequency to counter jamming (known as frequency agility) [7], these features make this analytic inversion a much more difficult task than in the simple case presented.

3.4 Semi-analytic mapping

Since a full analytic inversion of the mapping which defines the PFA is not always achievable an alternative method of performing the inversion was sought. This method is described as a semi-analytic mapping since it relies on the same principle as the analytic inversion, however the inversion itself is performed using an interpolation procedure to determine the noninteger desired sample positions in the mapped domain.

The samples of the collected bistatic SAR data are located in k-space on a distorted polar raster given by;

$$\mathbf{k} = \omega \left(\frac{\widehat{\mathbf{u}}_t + \widehat{\mathbf{u}}_r}{2} \right) \tag{3.29}$$

$$\mathbf{k} = \omega \mathbf{u} \tag{3.30}$$

$$\mathbf{k} = \omega |\mathbf{u}| \widehat{\mathbf{u}} \tag{3.31}$$

where $\widehat{\mathbf{u}}_t$ is the unit vector in the direction of the transmit platform, $\widehat{\mathbf{u}}_r$ is the unit vector in the direction of the receive platform and $\mathbf{u}$ is the bistatic look vector. Therefore $\mathbf{u}$ is a function of the bistatic look direction θ, given by half the bistatic angle.

$$\widehat{\mathbf{u}} = \begin{bmatrix} \cos\theta \\ \sin\theta \end{bmatrix} \tag{3.32}$$

To be more explicit the k_x and k_y sample locations are given by;

$$\mathbf{k} = \begin{bmatrix} \mathbf{k}_x \\ \mathbf{k}_y \end{bmatrix} = \omega_j |\mathbf{u}(\theta_i)| \widehat{\mathbf{u}}(\theta_i) \tag{3.33}$$

where the subscript i indicates the pulse number and the subscript j indicates the frequency

sample number. Then the integer pair $[i, j]$ define a uniform rectangular grid. Equation (3.33) provides a nonlinear function mapping points on the uniform grid at $[i, j]$ to points in k-space $[k_x, k_y]$. To form images using the FFT we need to map points on a nonuniform grid in k-space $[k_x, k_y]$ onto the space defined by $[i, j]$, therefore we need to invert the nonlinear mapping function given in equation 3.33.

$$\mathbf{k} = f\left(\begin{bmatrix} i \\ j \end{bmatrix}\right) \tag{3.34}$$

$$\begin{bmatrix} i \\ j \end{bmatrix} = f^{-1}(\mathbf{k}) \tag{3.35}$$

In some cases with simple geometry, this mapping can be inverted to provide a mapping function that can be used to map the polar raster to a uniform rectangular grid and for the desired rectangular grid to the same space. This analytic inversion is not always achievable but in these cases the inversion can be performed by way of utilising the intermediate function θ.

$$\theta(t) = \tan^{-1}\left(\frac{\widehat{u}_x(t)}{\widehat{u}_y(t)}\right) = \tan^{-1}\left(\frac{\mathbf{k}_x}{\mathbf{k}_y}\right) \tag{3.36}$$

where $u_x(t)$ is the x-component of the bistatic look vector and $u_y(t)$ is the y-component of the bistatic look vector. θ provides the mapping from k_x,k_y to pulse number for the collected samples, if this function is up-sampled then it can be used to perform the mapping operation for the desired sample locations, giving the noninteger pulse number *i*. As illustrated in Figure 3.4(a) the function θ yields a noninteger value of *i* for a k'_x,k'_y position not lying on the original sample grid. The same operation of up sampling the data and interpolating gives the values of the functions $|\mathbf{u}(\theta_i)|$ and $\widehat{\mathbf{u}}(\theta_i)$ for these noninteger values of *i*. Now using these values;

$$\omega_j = \frac{|\mathbf{k}|}{|\mathbf{u}(\theta_i)|} \tag{3.37}$$

giving the noninteger frequency sample number *j*, for the desired sample locations. Again as illustrated in Figure 3.4(b) a chosen sample point not lying on the original sample grid is used to obtain the sample number for the chosen point.

3.4.1 Results

This semi-analytic mapping method has been implemented in MATLAB and the results of performing the mapping on the 1m resolution, 60^o bistatic angle, simulated SAR data used in the

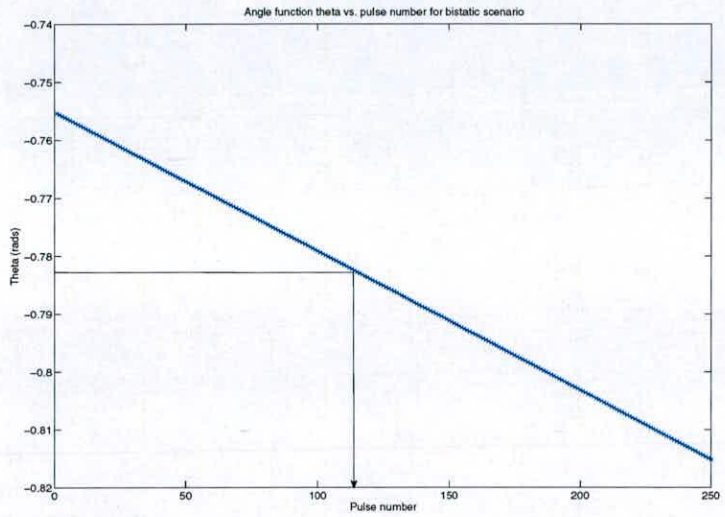

(a)

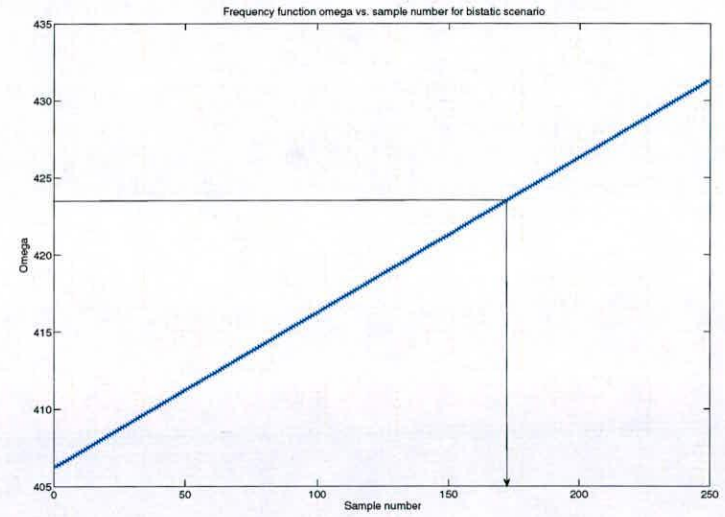

(b)

Figure 3.4: *Upsampled (a) angle and (b) frequency functions. A chosen k_x,k_y provide the pulse number of the point. Then using this pulse number the frequency function can be produced which provides the sample number for the given frequency.*

previous two sections are shown in Figure 3.5.

The rms error of the semi-analytic mapping operation was calculated to be, $error_{rms} = 0.0046$. The semi-analytic mapping result shown in Figure 3.5(b) looks unlike the results presented for the previous mapping methods, this is because the interpolation required to perform the mapping for the desired points outside of the collected area of k-space is impossible, therefore these samples have been mapped to (0,0). This means that the full area of the mapped space doesn't have the same outline as for the previous mapping methods.

3.4.2 Discussion

A semi-analytic inversion of the k-space sample locations within the PFA has been derived and demonstrated to perform an accurate mapping from the k-space sample locations to the desired interpolation domain, where the 2D interpolation from the known to desired sample locations is separable This semi-analytic mapping is a more robust and versatile version of the analytic mapping presented in the previous section.

3.5 Comparison

In this section the three mapping algorithms developed in the previous sections are compared, along with the keystone resampling method, to evaluate the mapping accuracy achieved by the mapping algorithms in different bistatic SAR simulations. When comparing the mapping algorithms, in addition to the previous discussion of mapping accuracy and generality of the algorithm , it is important to note that the accuracy which the mapping is performed to is only one of the properties of the method that is of interest. The computational complexity of the algorithm is also an important property. The computational complexity of the three mapping algorithms and the keystone resampling method is analysed, to determine which of the algorithms are computationally less intensive along with which parts of the mapping algorithms in particular lead to this computational complexity.

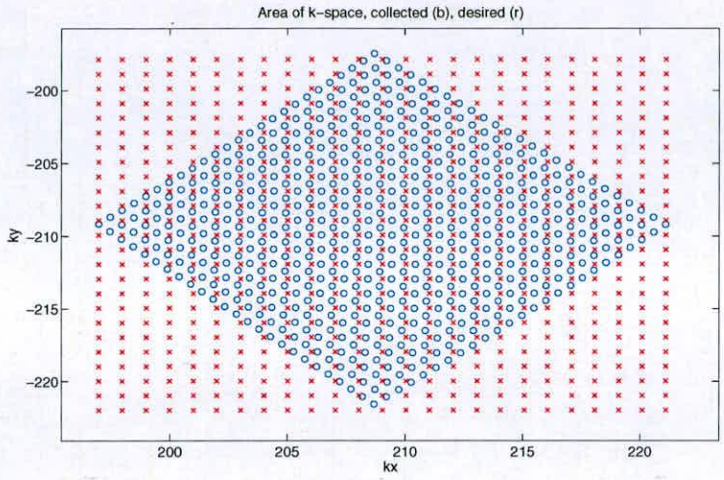

(a)

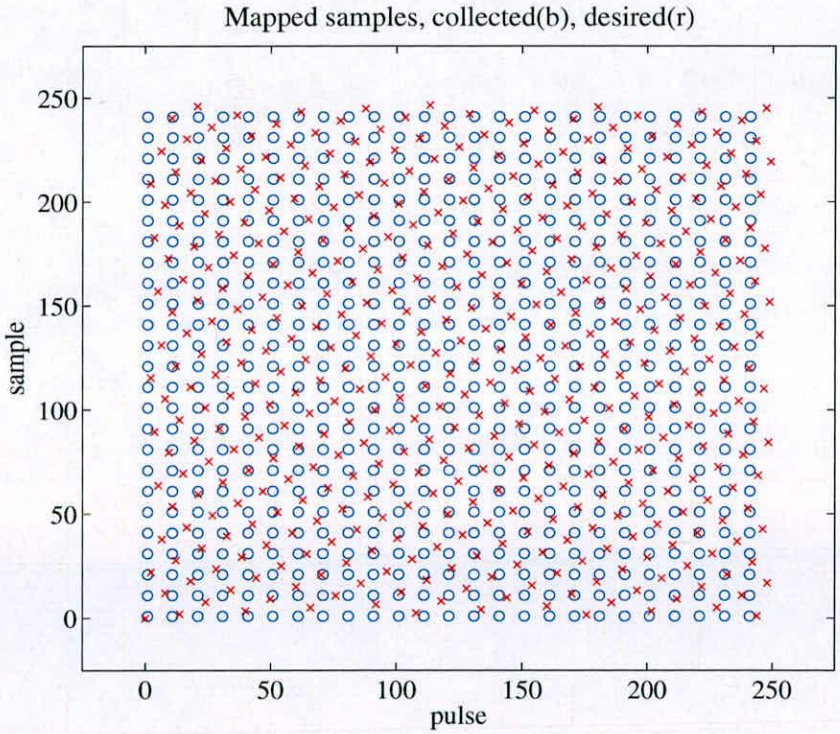

(b)

Figure 3.5: *Sample and desired k-space locations (a) before and (b) after semi-analytic mapping operation.*

3.5.1 Computational cost

There are many different possible ways of evaluating the computational complexity of an algorithm, the method used in this section follows the method used in [2], a simple computation count was performed for each of the mapping methods. For the purposes of this operation count the number of floating point real number additions and multiplications were counted, with an addition or multiplication being considered a single operation. A single complex operation is considered to be a single radix-2 FFT butterfly, this consists of one complex multiply and two complex additions, this equates to four floating point multiplications and six floating point additions. This means that a simple conversion of ten floating point operations per complex operation can be used [2].

Using this analysis the complex operation count, C_{fft}, for a power of 2 FFT is given by

$$C_{fft} = \left(\frac{N}{2}\right) log_2 N \tag{3.38}$$

and the computational cost to perform an interpolation, C_p, for N output points is given by

$$C_p = \left(\frac{N}{2}\right) \left[(L_f - 1)\, DSR + 1\right] \tag{3.39}$$

where, L_f, is the length of interpolation filter used and, DSR, is the downsample rate of the interpolation procedure [2].

Performing the Volterra mapping as described in the previous section requires an affine mapping and the Volterra mapping to be performed. These two mapping operations can be broken down into several processing stages, the affine map requires calculation of the mean and covariance of the input sample points, then an eigenvalue decomposition is performed. The Volterra series mapping coefficients are calculated by a least squares estimate as in equation 3.6.

Table 3.1 shows the computation count for each of these stages, based on a third order Volterra series being used for the mapping procedure. The table also shows the number of floating point operations for typical simulated parameters with N sample points , where $N = N_p N s$, ie. the number of pulses multiplied by the number of fast time samples on each pulse and $N_p = N_s = 250$, hence $N = 62500$ samples in Tables 3.1 to 3.4.

This computation count shows that the most computationally intensive part of the Volterra mapping method is the least squares estimate of the Volterra mapping coefficients. This operation

Volterra mapping stage	Computation count	Floating point operations (millions)
Calculate mean and covariance	$6N$	0.375
Eigenvalue decomposition	$24N$	1.500
Affine map	$19N$	1.188
Least squares estimate	$260N$ + 36324000	336.592
Total floating point operations	$309N + 36324000$	339.655

Table 3.1: *Floating point operations count for the Volterra mapping method, $N = 62500$.*

is computationally intensive due to the requirement of calculating the inverse matrix $[\mathbf{K}^T\mathbf{K}]^{-1}$, a computationally demanding operation for a large matrix.

Performing the analytic mapping as described in the previous section can be broken down into repeated calculation for each desired sample position of noninteger pulse number, i_{new}, transmit and receive platform positions at this time in the flight path, $\mathbf{x}_{tnew}$ and $\mathbf{x}_{rnew}$, the look direction vector at this position, $|\mathbf{u}|$, and finally the calulation of the noninteger sample number , j.

Table 3.2 shows the computation count for each of these stages in the mapping procedure along with the number of floating point operations associated with each stage for the typical simulated number of samples as described previously.

Analytic mapping stage	Computation count	Floating point operations (millions)
Calculate i_{new}	$40N$	2.500
Calculate $\mathbf{x}_{tnew}$ and $\mathbf{x}_{rnew}$	$40N$	2.500
Calculate $\|\mathbf{u}\|$	$52N$	3.250
Calculate j	$37N$	2.313
Total floating point operations	$169N$	10.563

Table 3.2: *Floating point operations count for the analytic mapping method, $N = 62500$.*

When analysing the computational cost of the analytic mapping method, there are no large matrix inversions or transpositions as in the Volterra mapping. Therefore the computational cost of implementing the analytic mapping method is approximately equal for each stage of the mapping.

The semi-analytic mapping method may be expected to perform similarly to the analytic method

in this computational cost analysis since it is based on the same principles. However unlike the analytic mapping where the algorithms consists of multiplications of each sample point, the semi-analytic mapping is achieved using repeated interpolations to determine the pulse and sample number for each desired sample point. The stages that the semi-analytic mapping method is broken down into for the purposes of this computational cost analysis are calculating and interpolating the intermediate function θ, calculating and interpolating the value of the intermediate look direction vector $|\mathbf{u}|$, then calculation of the noninteger pulse number i, and the noninteger sample number j.

Table 3.3 shows the computation count for each of these stages in the mapping procedure along with the number of floating point operations associated with each stage for the typical simulated number of samples as described previously.

Semi-analytic mapping stage	Computation count	Floating point operations (millions)
Calculate and upsample θ	$52\sqrt{N}$	0.013
Calculate and upsample $\|\mathbf{u}\|$	$71\sqrt{N}$	0.018
Obtain i	$54N$	3.375
Obtain j	$72N$	4.500
Total floating point operations	$126N + 123\sqrt{N}$	7.906

Table 3.3: *Floating point operations count for the semi-analytic mapping method, $N = 62500$.*

The upsampling operations in the semi-analytic mapping method are relatively efficient due to the use of bilinear interpolation, the most computationally intensive stages of the semi-analytic mapping are the look up operations performed while determining the noninteger pulse and sample numbers, i and j.

The keystone method can be broken down into two main stages, fast time and slow time resampling operations. Both of these operations can in turn be split into three main processing stages, calculating the length of the sample vector in the given direction, calculating the equation of the line the samples lie on and finally calculating the intercept points of the known and desired sample grids.

Table 3.4 shows the computation count for each of these stages in the mapping procedure along with the number of floating point operations associated with each stage for the typical simulated number of samples as described previously.

Keystone method stage	Computation count	Floating point operations (millions)
Calculate radius	$18N$	1.125
Calculate line equations	$5N + 5\sqrt{N}$	0.314
Find intercepts	$6N$	0.375
Calculate length	$20N$	1.250
Calculate line equations	$5N + 5\sqrt{N}$	0.314
Find intercepts	$6N$	0.375
Total floating point operations	$60N + 10\sqrt{N}$	3.753

Table 3.4: *Floating point operations count for the keystone method, $N = 62500$.*

Similarly to the analytic mapping method, determining the desired resampling positions for the keystone interpolation method relies on simple addition and multiplication operations. To calculate the intersection of pulse lines with constant range spacing lines for instance. There are no single processing stages that are particularly computationally intensive and the computational cost of the keystone method is approximately equal for both the fast time and slow time resampling operations.

3.5.2 Mapping accuracy

The three mapping methods developed were used to perform the mapping in three different SAR simulations, the rms error was calculated to determine how accurately each mapping algorithm was able to perform the mapping. Third and fourth order Volterra series were both used to perform the mapping to determine if any improvement in mapping accuracy was achieved using a higher order Volterra series to perform the mapping. The three SAR scenarios each with approximately 1m range and azimuth resolution are: a non-accelerating bistatic SAR system with bistatic angle, $\beta = 90^o$, a constantly accelerating monstatic SAR system with $a_t = a_r = 20\text{ms}^{-1}$ and lastly a bistatic SAR system with an accelerating receive platform with bistatic angle, $\beta = 90^o$, $a_t = 0\text{ms}^{-1}$ and $a_r = 20\text{ms}^{-1}$.

The error in the azimuth resampling operation in the keystone resampling method is due to the assumption that the azimuth sample spacing is uniform. The azimuth sample spacing doesn't vary significantly from the monostatic to the bistatic case, therefore the estimated error is the same for monostatic and bistatic cases. For reference, the approximate error in the azimuth resampling operation is 3.4652 x 10^{-5} for the non-accelerating case and 1.1908 x 10^{-2} for the

accelerating case.

Another measure of the computational complexity of each mapping method is to measure the time taken to perform the mapping operation. The MATLAB simulations of each of the mapping methods used to produce the results presented in this section were timed. The result of this timing along with the rms error results are shown in Tables 3.5, 3.6 and 3.7. These timings can only be taken as a guide to the time taken to perform the mapping using each mapping method, since the MATLAB code used is unoptimised and can vary significantly depending upon successful use of vectorisation in the implementation. In addition some algorithms are easier to efficiently program, for instance the matrix operations involved in the Volterra series mapping provide an efficient way to implement that algorithm. However this may cause disparity between the algorithms purely because of ease of programming.

Mapping method	rms error	time taken (s)
3rd order Volterra series	3.2874×10^{-4}	0.395726
4th order Volterra series	3.2874×10^{-4}	0.827689
Analytic	3.7208×10^{-13}	5.358786
Semi-analytic	0.0067	98.699925

Table 3.5: *rms error and computational speed for each of the mapping methods for a non-accelerating bistatic SAR scenario,* $\beta = 90^o$, $a_t = a_r = 0ms^{-1}$.

Mapping method	rms error	time taken (s)
3rd order Volterra series	0.1439	0.467348
4th order Volterra series	0.1439	1.036017
Analytic	3.4288×10^{-13}	6.876574
Semi-analytic	0.0096	159.856984

Table 3.6: *rms error and computational speed for each of the mapping methods for an accelerating monostatic SAR scenario,* $\beta = 0^o$, $a_t = a_r = 20ms^{-1}$.

Mapping method	rms error	time taken (s)
3rd order Volterra series	0.0394	0.427685
4th order Volterra series	0.0394	0.935402
Analytic	0.3757	5.885312
Semi-analytic	0.3831	138.876770

Table 3.7: *rms error and computational speed for each of the mapping methods for an accelerating bistatic SAR scenario,* $\beta = 90^o$, $a_t = 0ms^{-1}$, $a_r = 20ms^{-1}$.

The mapping accuracy of the Volterra mapping algorithm is good for the non-accelerating bistatic case, for the accelerating bistatic case the performance is considerably worse however this error still represents approximately a 4% error in the mapping operation. The performance of the Volterra mapping algorithm in the accelerating monostatic case is worse again, representing approximately a 15% error in the mapping.

The anlaytic mapping algorithm provides accurate mapping in both the non-accelerating bistatic and the accelerating monostatic cases, however the algorithm provides poor mapping accuracy for the accelerating bistatic case where the resulting error introduces a significant error into the resampling operation. The mapping accuracy of the semi-anlytic mapping algorithm is similarly poor for the accelerating bistatic case, but is accurate to approximately 1% of the sample spacing in both the other cases.

The timing results presented in Tables 3.5, 3.6 and 3.7 show that the Volterra mapping algorithm is the fastest in each of the scenarios considered, with the fourth order Volterra series taking longer to compute than the third order series. The analytic mapping method is slower than the Volterra series mapping but faster than the semi-analytic mapping in each case. The efficient vectorisation of the Volterra mapping algorithm is a possible source of this computational speed, where the analytic mapping has not been as efficiently implemented. The times taken by the semi-analytic mapping are significantly greater than for the other methods mainly due to the look up operations performed as part of this algorithm.

3.5.3 Discussion

Computational cost analysis of the three mapping algorithms developed in the previous sections of this chapter has been presented. This computational cost analysis shows that the analytic and semi-analytic mapping methods are less computationally complex than the Volterra series based mapping method. One of the reasons for this reduction in complexity is the more specific nature of these algorithms which are designed solely for application to the accelerating bistatic SAR PFA resampling problem, where as the Volterra mapping is a more generally applicable method of performing mappings.

Results showing the rms error in applying each of the mapping methods to various SAR scenarios have been presented. These rms error results show that for the examples considered no improvement in mapping accuracy is gained by using fourth order terms in the Volterra series.

The rms error results show that the analytic mapping algorithm performs extremely accurate mapping except in the case of the accelerating bistatic SAR example where the rms error represents an unacceptably large error in the mapping which is sure to corrupt the content of resulting SAR images. The Volterra mapping and semi-analytic mapping algorithms both perform well for the non-accelerating bistatic SAR, however each of these algorithms fails in either the accelerating monostatic or bistatic SAR examples, though the degradation in mapping accuracy for the Volterra series based mapping algorithm is less than for the other two methods when it performs poorly.

Determining the necessary balance between computational complexity and accuracy is beyond the scope of this section and is application specific. For instance a specific radar system may present the pilot with real-time SAR imagery and in these cases the accuracy of the mapping operation might be less important than the computation time taken to present the image to the pilot. However in a ground station solution where the time taken to form the image is of less importance, a more accurate solution might be preferable.

3.6 Interpolation

The motivation for performing the mapping operation is that after mapping the interpolation can be performed in a domain where this procedure is simpler. In the mapped domain the interpolation is separable into two 1D interpolations, interpolating from a regular rectangular grid to an irregular grid of desired sample locations. Two different methods of performing this interpolation are discussed in this section, an input centred method based on oversampling the input data in both dimensions to calculate each output sample, and an inverse method using an output centred method to calculate each output sample from the contribution from every input sample, termed as such since it is the inverse of the method used for the oversampling method.

3.6.1 Oversampling

One method of performing the interpolation necessary for use of the FFT is to increase the sample density of the data on the regular rectangular grid to such a degree that a known sample value corresponds to every desired sample position. To do this a limited length $\mathrm{sinc}(x)$ function, scaled to the value of the sample, is placed in each of the known sample positions as described in section 2.5. The data is then evaluated as the sum of all these $\mathrm{sinc}(x)$ functions in a given

direction (vertical for instance) at positions on a much finer grid, this process is then repeated in the other direction (horizontal).

$$\begin{aligned} \mathbf{Z}_{nj} &= \sum_{i=1}^{N}\sum_{n=1}^{N_d} \mathbf{A}_{ij}\mathrm{sinc}(k'_{xn} - k'_{xij}) \\ \mathbf{Z}_{nm} &= \sum_{j=1}^{M}\sum_{m=1}^{M_d} \mathbf{Z}_{nj}\mathrm{sinc}(k'_{ym} - k'_{ynj}) \end{aligned} \tag{3.40}$$

where A is the sample value and the subscripts i, j refer to the i, jth sample, k'_x and k'_y refer to the locations of the samples in the mapped k' domain and the subscripts n, m refer to the n, mth desired sample, Z is the interpolated sample value, there are NM input samples and N_dM_d output samples.

After this operation the phase history data is sampled on a regular rectangular grid with a higher sample density in both directions. However without a nearly infinite sample density it is unlikely that these new samples will coincide with all the desired sample locations, so either the nearest sample can be selected or a linear interpolation performed between the two nearest samples to obtain the value of the desired sample.

3.6.2 Inverse method

An alternative method of calculating the value of desired sample points can be implemented as follows. Instead of upsampling to a more dense data set, the distances of a desired sample point from all known sample locations (in the mapped domain) in the k'_x and k'_y directions are calculated. The value of the basis $\mathrm{sinc}(x)$ interpolation function for all these distances is then calculated and the value contributed to the desired sample point from each known point is the product of the two values.

$$\begin{aligned} \mathbf{X}_{nm} &= \mathbf{K}'_{\mathbf{x}} - k'_{xnm} \\ \mathbf{Y}_{nm} &= \mathbf{K}'_{\mathbf{y}} - k'_{ynm} \end{aligned} \tag{3.41}$$

$$\mathbf{Z}_{nm} = \mathrm{sinc}(\mathbf{X}_{nm})\mathrm{sinc}(\mathbf{Y}_{nm}) \tag{3.42}$$

where k_x and k_y are coordinates of the n, mth sample in the mapped k' space, $\mathbf{K}'_{\mathbf{x}}$ and $\mathbf{K}'_{\mathbf{y}}$ are matrices of the coordinates of the known samples in the mapped k' space, $\mathbf{X}_{nm}$ and $\mathbf{Y}_{nm}$ are matrices of the distances from the n, mth sample to all the known samples in the x and y

directions respectively, and $\mathbf{Z}_{nm}$ is the interpolated value of the n, mth desired sample point.

This has been termed an inverse method because the interpolation is calculated in the opposite way to the oversampling method, ie. rather than evaluate the contribution of a single known point to all desired points, a single desired point is calculated from all known points. This type of method can also be referred to as output centred interpolation since the value of the desired output samples are calculated one at a time.

3.6.3 Comparison

A bistatic SAR image formation simulation was performed using the Volterra series mapping method to perform the mapping and using both of the interpolation procedures described in this section. When implementing the oversampling method of interpolation the oversampling rate selection was problematic. As described previously, a higher oversampling rate increases the chance of points on the desired grid coinciding with points on the higher sample density known values grid, however high oversampling rates require large amounts of memory for the interpolation procedure, often exceeding the computational memory available. The oversampling rate was fixed at 16 times oversampling, this is clearly not the infinite oversampling desired, meaning that linear interpolation between the nearest known sample points is necessary.

Results from the simulations performed are included in Figure 3.6. The image formed using the oversampling method shows a residual blurring error near the edges of the imaged scene. This error is not due to inaccuracy in the mapping method, as it would be present in both images if this were the case. The error shown is due to the limit on oversampling rate. The oversampling interpolation method is introducing a quantisation type error into the image formation process. As the oversampling rate is reduced, the space between the two samples selected for linear interpolation increases, resulting in a less accurate value for the desired sample. This error varies for each sample and has a greater effect on the interpolation of signals which have a high frequency than on low frequency signals. This is why the blurring in the results shown is greatest nearest the scene edges. Scatterers near the scene edge induce a higher frequency sinewave in k-space than scatterers near to the scene centre, therefore the error introduced by the interpolation process causes greater blurring of these scatterers. This means that unless a higher than practical upsampling factor is used there will always be parts of the resulting images that will be subject to blurring.

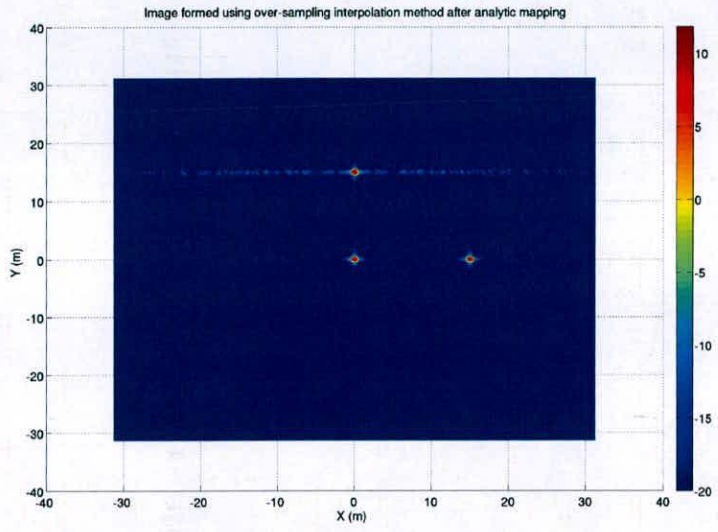

(a)

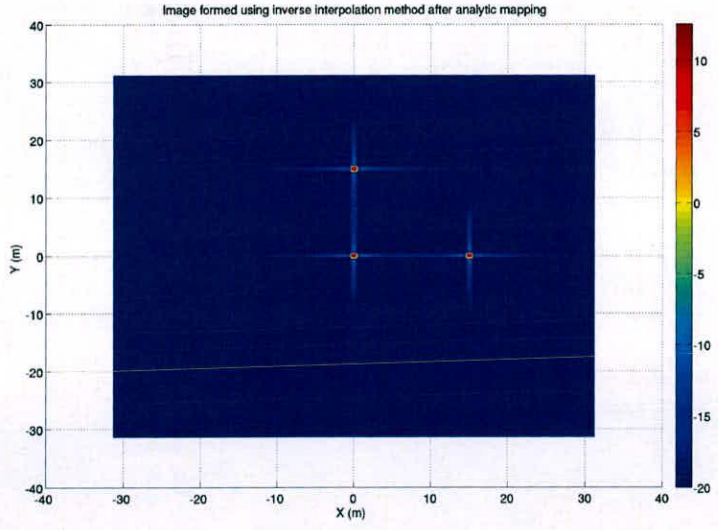

(b)

Figure 3.6: *SAR images formed using the PFA after mapping using the analytic mapping method using, (a) the oversampling method, (b) the inverse interpolation method.*

The memory requirements of the two interpolation methods differ, the oversampling method is memory intensive due to storing all the intermediate sample positions before performing the linear interpolation. The first oversampling operation increases the size of the data set by the oversampling factor, this larger data set is then oversampled a second time resulting in a much larger data set ie. for an MxN grid with an oversampling rate R_{over} the number of stored samples N_{stored} increases twice;

$$\begin{aligned} step1 : N_{stored} &= (R_{over}M)N \\ step2 : N_{stored} &= (R_{over}M)(R_{over}N) \\ \Rightarrow N_{stored} &= R_{over}^2 MN \end{aligned} \tag{3.43}$$

Since the inverse method doesn't store any intermediate results the data set does not grow in this way. The number of computations necessary for the inverse method is also lower than for the oversampling method, by approximately the oversampling rate, since the additional linear interpolation adds little compared to evaluating the interpolation functions at all the extra oversample points. In addition to the improved accuracy in interpolation of high frequency signals giving better focused images, the inverse interpolation method provides a better method for performing the interpolation procedure required.

3.7 Simulation results

When considering manoeuvring aircraft it is important to understand the effect that the manoeuvre has on the sampled area of k-space obtained. A simple manoeuvre to consider is a circular turn, typical of a SAR system mounted on a jet aircraft. The circular turn gives the aircraft a significant component of its velocity in the direction of the scene centre, how does this affect the sampled area of k-space?

The area of k-space sampled during the data collection procedure is determined by;

$$\mathbf{k} = \omega \left(\frac{\hat{\mathbf{u}}_\mathbf{t} + \hat{\mathbf{u}}_\mathbf{r}}{2} \right) \tag{3.44}$$

where

$$\omega(t, \hat{t}) = \frac{4\pi}{c} \left[f_c + 2\mu \left(\hat{t} - \left(\frac{r_{0t}(t) + r_{0r}(t)}{c} \right) \right) \right] \tag{3.45}$$

so the radial lines of the distorted polar raster are determined by the bistatic look angle, and the distance of the samples along these radii are determined only by the radar parameters. This is because the distance to the scene centre is removed as a reference on receipt. Thus only the along track position at a given pulse time has a significant bearing on the sampled area of k-space. Therefore it is not necessary to determine exact manoeuvre geometries, it is enough to consider the case where transmit and receive platforms have significant along track accelerations, to determine the effect of irregular sampling on the image formation process. The irregular nature of the bistatic look angle for this case means that the sample spacing in k-space is more irregular than for the simple straight line constant velocity flight path normally considered for spotlight SAR.

A 2D bistatic SAR simulation where the receiver flight path can be varied was developed. This allows the effect of both bistatic angle, β, and receiver acceleration, a_r to be observed. Each simulation with a different mid-pulse bistatic angle ($\beta = 0^o, 30^o, 60^o, 90^o$) was repeated for different receiver accelerations ($a_r = 0, 10, 20, 30$ ms^{-2}). The radar parameters used in the simulation are shown in Table 3.8. The data is then processed according to the PFA using the semi-analytic mapping method where the interpolation is performed using the inverse interpolation routine.

Radar Parameters	Radar Parameters
$f_c = 10$ GHz	$B = 600$ MHz
$f_s = 0.41667$ MHz	$T_p = 600\mu$ s
$PRF = 0.041667$ kHz	$R_0 = 15$ km
$v_t = v_r = 150$ ms^{-1}	

Table 3.8: *Radar parameters used for bistatic SAR simulation.*

3.7.1 Results using mapping method

The simulation was performed as described above for $\beta = 0^o$ ie. the monostatic case. Figure 3.7 shows the image formed with $a_r = 10$ ms^{-2} and also the point spread function (psf) of a target displaced in the x-direction as it appears in SAR images formed when the receiver platform acceleration is varied.

Figure 3.7(a) shows the SAR image reconstruction of the target scene which consists of three

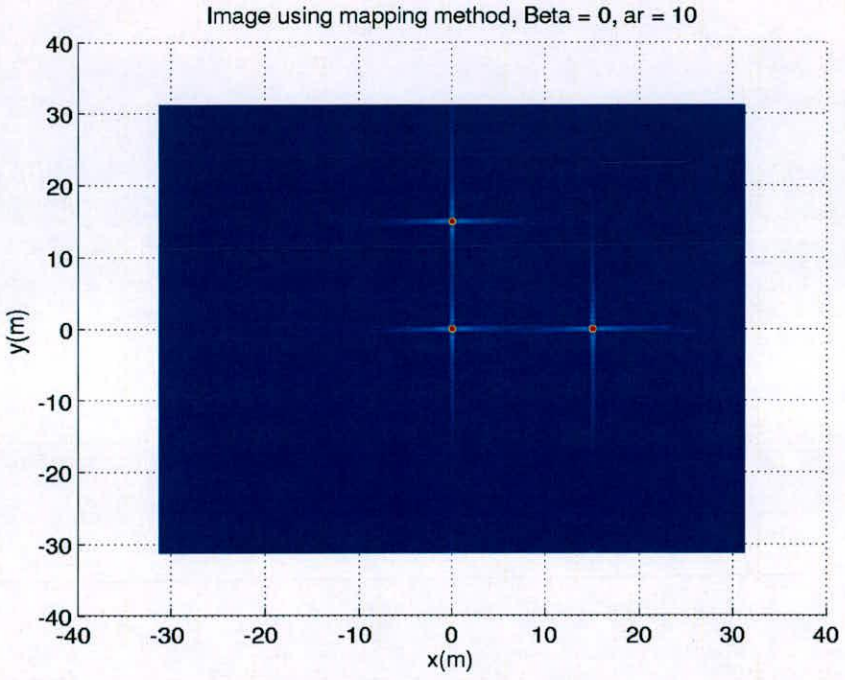

(a)

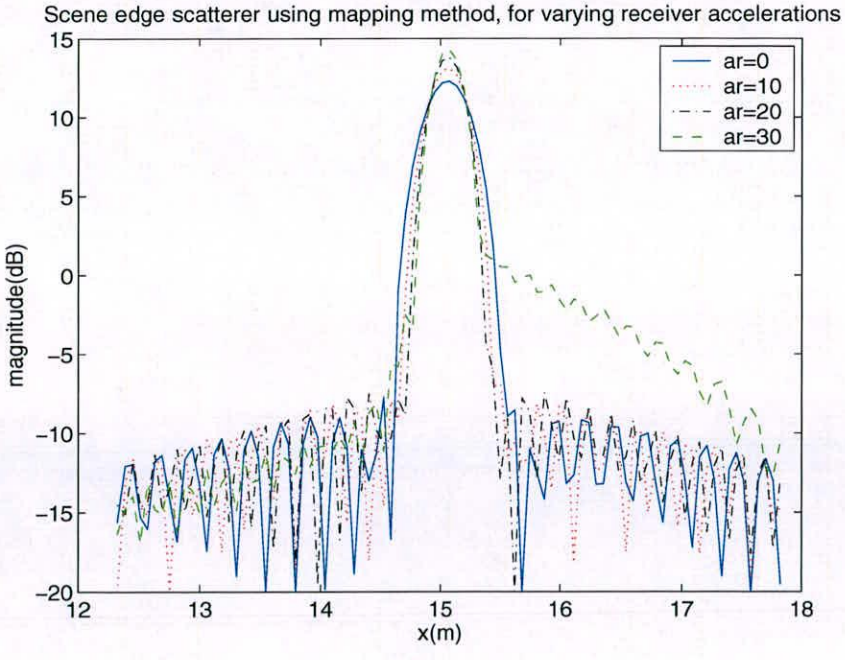

(b)

Figure 3.7: *(a) Image formed using mapping method for $\beta = 0^o$ and (b) psf for varying receiver acceleration.*

point targets, one at the scene centre, one displaced 15m in the y-direction and one displaced 15m in the x-direction. The colormap shows the magnitude of the reconstructed SAR image on a logarithmic scale with the pixels with the greatest magnitude shown in red, and lowest magnitude pixels in dark blue. Figure 3.7(b) shows the value of the resulting images at a slice through the azimuth sidelobe structure of the target displaced in the x-direction. The figure shows that the psf of the scatterer displaced in the x-direction doesn't change significantly when the receiver acceleration is varied. There is a slight improvement in resolution with the accelerating platform causing the scatterer mainlobe to be slightly narrower than for the non-accelerating case. This slight increase in resolution is due to the receiving platform traversing a slightly longer flight path due to the acceleration. The high sidelobe in the result for $a_r = 30$ ms^{-2} is due to the scatterer being too near the scene edge and aliasing of the induced sinewave occurring. This is due to the variation in sample density throughout the area of k-space, sample density determines the highest frequency sinewave that can be supported and hence how large a scene can be imaged. This variation in sample density leads to a lower scene size than can be imaged at lower accelerations without aliasing occurring

Figure 3.8 shows the SAR image reconstruction of the target scene formed with $\beta = 30^o$ and $a_r = 10$ ms^{-2} and also the psf of the target displaced in the x-direction as it appears in SAR images formed when the receiver acceleration is varied. Figure 3.8(a) shows the same three targets with a rotated sidelobe structure due to the bistatic angle. Aliasing can be seen to occur before it would be expected to, for instance at approximately (x,y) = (-20,-10) where sidelobe content appears at an artificial scene edge. This appears because of the variation in k-space sample density as before. Figure 3.8(b) shows the value of the images at slices through the azimuth sidelobe structure of the target displaced in the xdirection. The psfs show the same improvement in resolution due to acceleration as seen in Figure 3.7(b) and the sidelobe levels of the psfs are also noticeably higher than those in Figure 3.7(b), this is noticeable in Figure 3.8(a) as poorer image contrast.

Figure 3.9 shows the SAR image reconstruction of the target scene formed with $\beta = 60^o$ and $a_r = 10$ ms^{-2} and also the psf of the target displaced in the x-direction as it appears in SAR images formed when the receiver acceleration is varied. Figure 3.9(a) shows the same three targets with a rotated sidelobe structure due to the bistatic angle. Again aliasing can be seen to

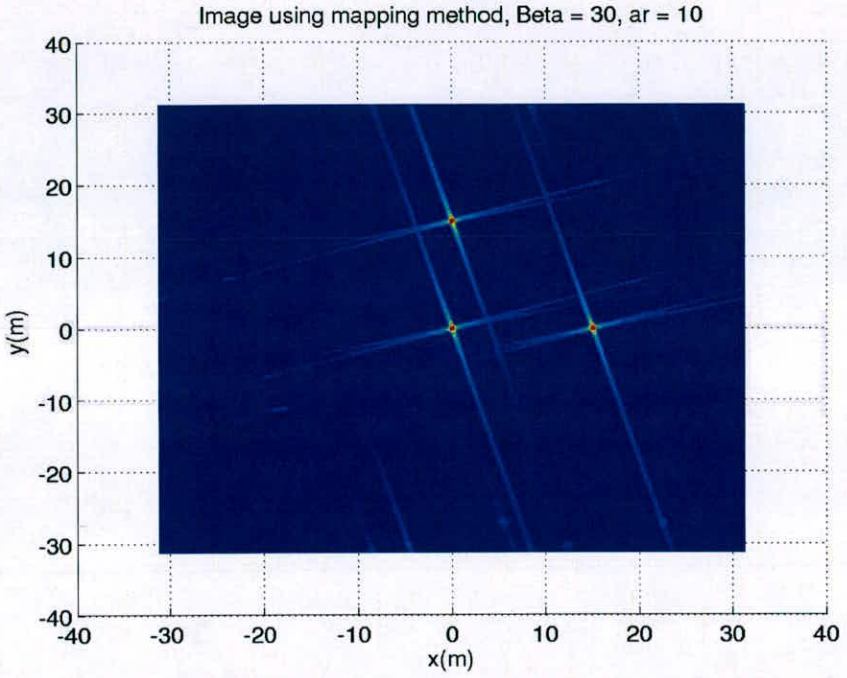

(a)

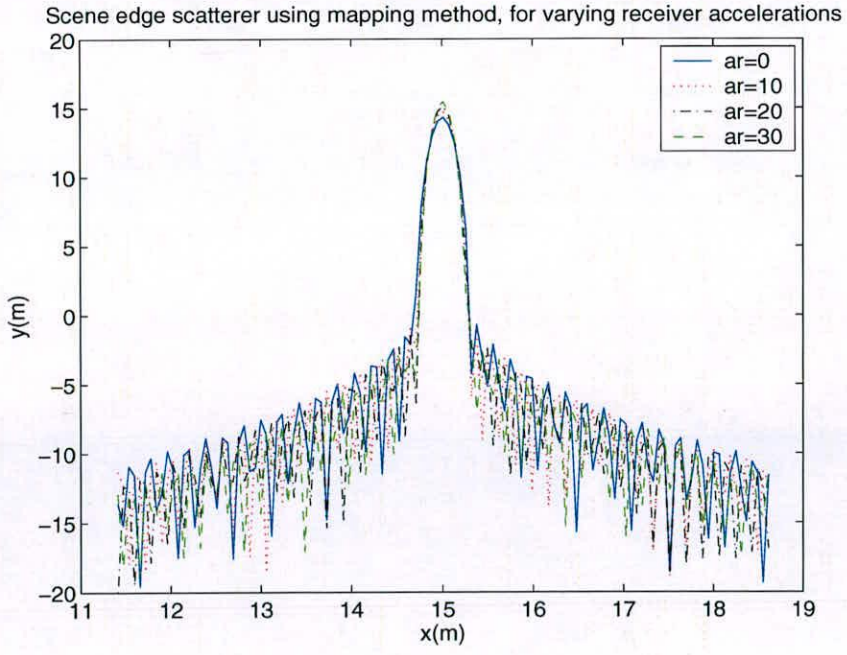

(b)

Figure 3.8: *(a) Image formed using mapping method for $\beta = 30^o$ and (b) psf for varying receiver acceleration.*

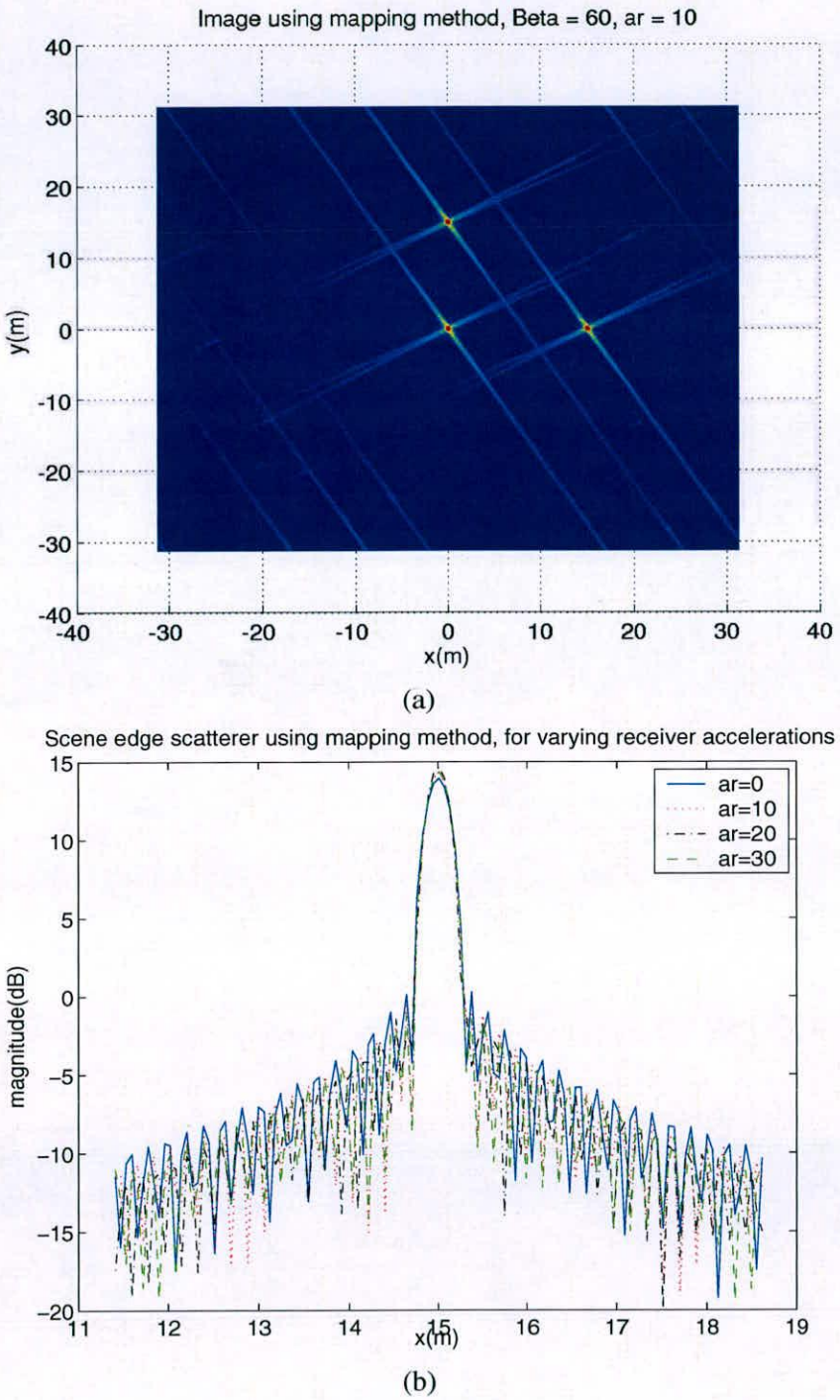

Figure 3.9: *(a) Image formed using mapping method for $\beta = 60^o$ and (b) psf for varying receiver acceleration.*

occur before it would be expected to, for instance at approximately (x,y) = (-25,0). Also bright spots in the aliased sidelobes can be seen, for instance at approximately (x,y) = (-5,-25), it is thought that these are due to the combination of the aliased sidelobes at points where they are unsupported by any of the sample densities present. Figure 3.9(b) shows the value of the images at slices through the azimuth sidelobe structure of the target displaced in the x-direction. The psfs show the same improvement in resolution due to acceleration as seen in Figure 3.7(b) and the sidelobe levels of the psfs are also noticeably higher than those in Figure 3.7(b), this is noticeable in Figure 3.9(a) as poorer image contrast.

Figure 3.10 shows the SAR image reconstruction of the target scene formed with $\beta = 90^o$ and $a_r = 10$ ms^{-2} and also the psf of the target displaced in the x-direction as it appears in SAR images formed when the receiver acceleration is varied. Figure 3.10(a) shows the same three targets with a rotated sidelobe structure due to the bistatic angle. Again aliasing can be seen to occur before it would be expected to, for instance at approximately (x,y) = (25,20) and bright spots in the aliased sidelobes can be seen, for instance at approximately (x,y) = (-25,-25). The psfs show the same improvement in resolution due to acceleration as seen in Figure 3.7(b) and the sidelobe levels of the psfs are also noticeably higher than those in Figure 3.7(b).

3.7.2 Results using keystone interpolation

2D monostatic SAR simulations with varying platform acceleration were performed using the radar parameters shown in Table 3.8. Figure 3.11 shows the images formed using the keystone method of interpolating the irregularly sampled phase history, for receiver accelerations (a) $a_r = 0$ ms^{-1} and (b) $a_r = 10$ ms^{-1}. Figure 3.12 shows the result of the simulation for receiver accelerations (a) $a_r = 20$ ms^{-1} and (b) $a_r = 30$ ms^{-1}. The figures show the simulated SAR images of the target scene which as before consists of three point targets, one at the scene centre, one displaced 15m in the range direction and one displaced 15m in the cross range direction. The colormap shows the magnitude of the reconstructed SAR image on a logarithmic scale with the pixels with the greatest magnitude shown in red, and lowest magnitude pixels in dark blue.

Figure 3.11(a) is nearly identical to the result presented in Figure 3.7 (a), with the same focus of the three scatterers achieved. Figure 3.11(b) show that as the platform acceleration increases there image blurring occurs in the cross range direction, this can be seen in the image as a

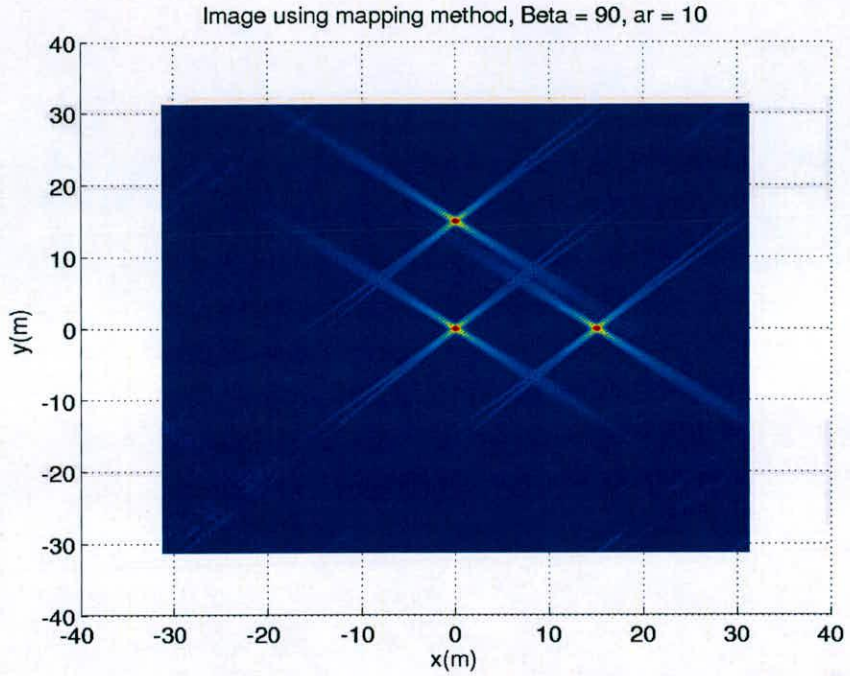

(a)

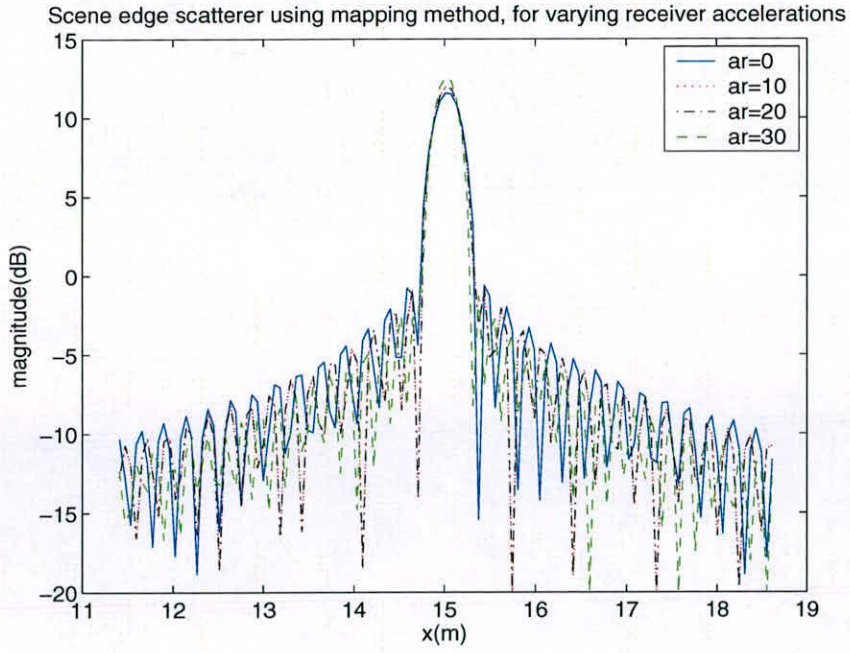

(b)

Figure 3.10: *(a) Image formed using mapping method for $\beta = 90^o$ and (b) psf for varying receiver acceleration.*

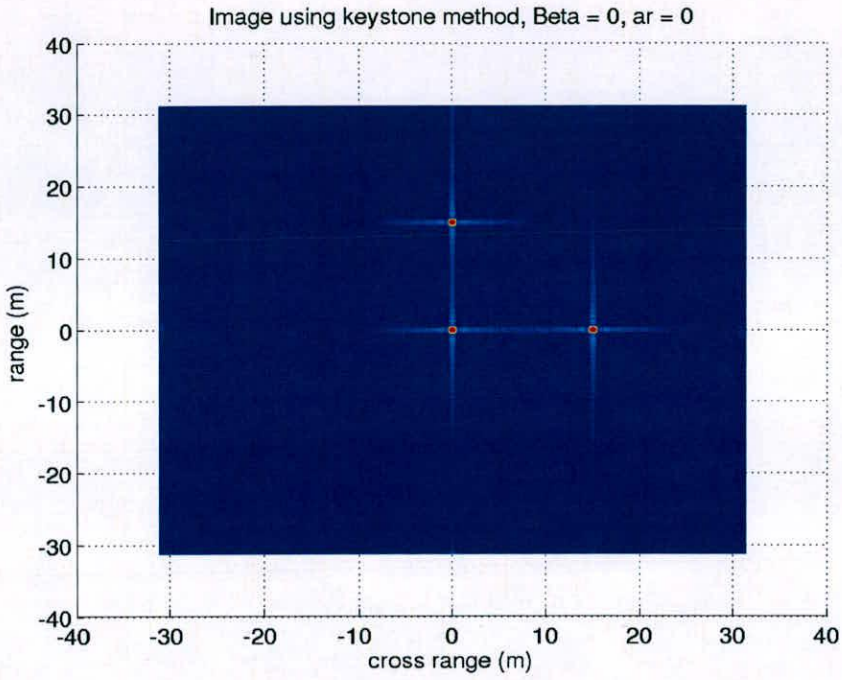

(a)

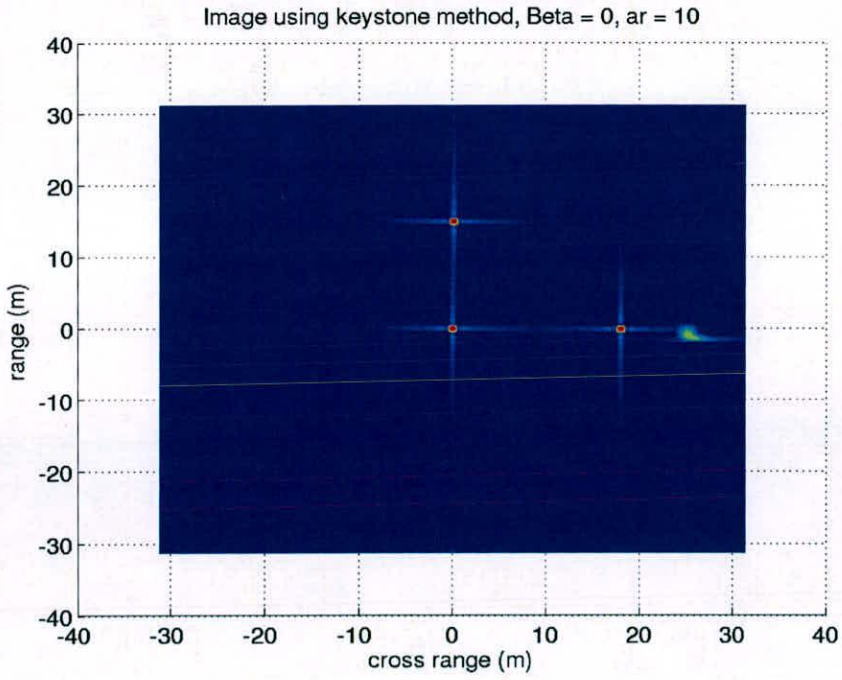

(b)

Figure 3.11: *Accelerating platform, $\beta = 0^o$, (a) $ar = 0\ ms^{-1}$, (b) $ar = 10\ ms^{-1}$, images formed using keystone interpolation method.*

green shape at (x,y) = (25,0). This blurring is due to the incorrect interpolation of the phase history data in the slow time resampling part of the keystone interpolation method. Due to the acceleration these samples are more irregularly spaced than in the nonaccelerating case. In addition the varying slow time sampling rate causes the PFA to place the scatterer displaced in cross range in the wrong position in the image, the target displaced in the cross range direction now appears at approximately (x,y) = (18,0).

Figure 3.12(a) shows the simulated SAR image formed with $a_r = 20$ ms^{-1} which shows that as the platform acceleration increases there is an increasing amount of energy present in the image blurring in the cross range direction, as the blurring present at approximately (x,y) = (25,0) covers a larger area of the simulated SAR image and has a greater magnitude. In addition the position error for the target displaced in the cross range direction is greater than in Figure 3.11(b), the target now appears at approximately (x,y) = (20,0).

Figure 3.12(b) shows the simulated SAR image formed with $a_r = 30$ ms^{-1} which shows even more image blurring in the cross range direction, as the blurring present at approximately (x,y) = (25,0) covers a larger area of the simulated SAR image and has a greater magnitude and also other blurring arefacts appear at approximately (x,y) =(-15,0),(15,0),(-15,-15) and (15,15). In addition the position error for the target displaced in the cross range direction is greater than in Figure 3.12(a), the target now appears at approximately (x,y) = (23,0).

3.8 Discussion

3.8.1 Summary

In this chapter a method for performing the polar to rectangular resampling required by the PFA for SAR image formation has been presented. This method aims to simplify the resampling process by mapping the known and desired sample points to a domain where the known samples lie on an integer spaced regular rectangular grid. This operation turns the irregular to regular grid resampling problem into a regular to irregular grid resampling. This allows the same interpolation function, which goes through zero at all other known sample points, to be used at all sample points in the data.

Three different methods of performing this mapping operation were derived. A Volterra series based mapping algorithm, using a least squares solution to a limited order polynomial to calcu-

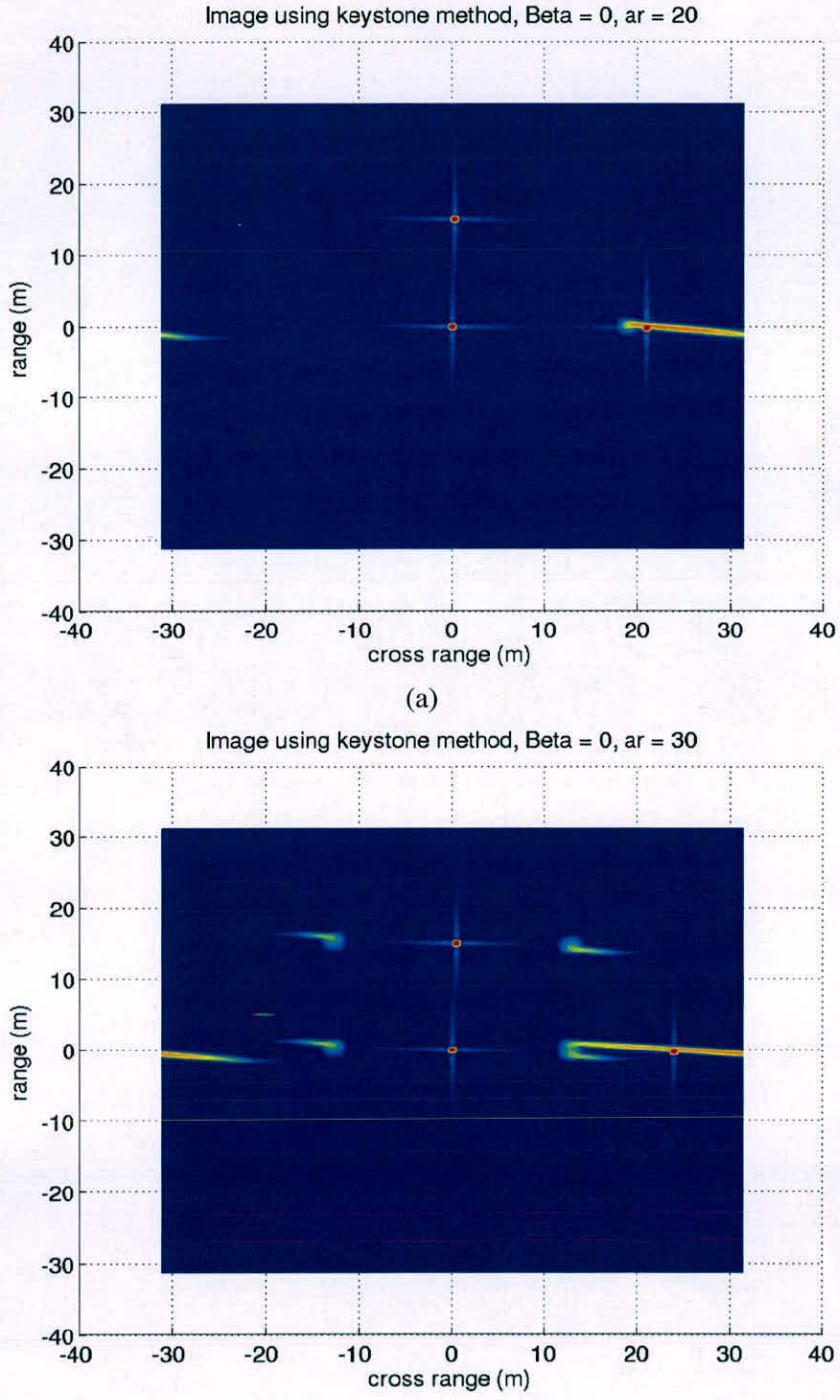

Figure 3.12: *Accelerating platform, $\beta = 0^o$, (a) $ar = 20\ ms^{-1}$, (b) $ar = 30\ ms^{-1}$, images formed using keystone interpolation method.*

late mapping coefficients used to map both the known and desired samples to the new domain. This method for performing the mapping is general and can map grids of arbitrary comlplexity provided sufficiently high ordered terms in the Volterra series are used in the mapping. An algorithm was derived by inversion of the inherent mapping operation in the PFA where the collected data samples are mapped from a matrix of pulse and sample numbers, to the polar raster in k-space. This derivation lacks the flexibility of the Volterra mapping algorithm as it is specific to the SAR data collection geometry, this more focused approach is computationally simpler than the Volterra mapping method however in scenarios with particularly complicated platform motion the analytic inversion becomes much more complex than for simple platform motions. A semi-analytic mapping method was derived, which uses the intermediate look direction vector to perform the mapping in a similar way to the analytic mapping method but using interpolated values of this vector to perform the mapping for the desired sample positions. This semi-analytic mapping method is simpler to perform than the analytic mapping method since it does not require an accurate mathematical representation of the platform motion.

A comparison of each of the three mapping algorithms has been presented, this comparison showed that the Volterra mapping algorithm is the most computationally complex mapping method considered mainly due to the flexibility of the algorithm. The rms error involved in performing the mapping operation was calculated for different SAR scenarios and although no algorithm provided extremely accurate mapping for all the scenarios considered, each algorithm was demonstrated to perform accurate mapping in at least one of the scenarios.

Two different algorithms for performing the resampling operation in the mapped domain were presented, a method based on oversampling the data and an output centred or inverse method. Performing interpolation using the oversampling method was demonstrated to introduce spatially varying errors into the resulting SAR images and required a large amount of computer memory be available for storing the oversampled data. The output centred interpolation method does not require the same computational resources as the inverse method and was demonstrated to perform accurate interpolation with little impact on resulting SAR image quality.

Simulation results demonstrating the application of the semi-analytic mapping method and the output centred interpolation to PFA SAR image formation for varying bistatic angles and accelerations were presented. These results showed that images formed using the proposed method contain few image artefacts from the mapping algorithm and that the method of interpolation was robust for various platform accelerations and bistatic geometries. Simulation results for im-

ages formed using the keystone interpolation method were also presented, these images showed that the keystone interpolation introduced significant blurring as a result of the assumption that the slow time resampling operation can be considered locally uniform.

3.8.2 Applications

In addition to providing a simple framework for the interpolation required for the PFA, the method described also allows interpolation of data on grids which cannot even locally be considered regular. This provides the imaging aircraft the opportunity to deviate from the fixed straight and level flight path normally required for SAR imaging, as deviation from this path simply changes the k-space sample density in the PFA. Provided the position of the aircraft is accurately recorded this type of sample density variation is not significantly different to the varying sample density of the distorted polar raster in conventional PFA. This method could also provide some ability to perform deliberate irregular sampling by alteration of the radar pulse repetition frequency as is common in many military applications where the enemy is likely to attempt to jam the receiving radar. This method could also provide some capability to perform interrupted SAR, forming images from non-continuous radar data sets. For instance combining the collected data from multiple imaging episodes of the same scene, either from the same platform or even in a multistatic operation where the data is collected by multiple radar antennae at different viewing angles.

Chapter 4
3D SAR Image Formation

4.1 Introduction

Spotlight SAR images are typically formed from data collected from aircraft following a linear constant altitude flight path. As a result of this flight path geometry the sampled area of k-space obtained is a 2D plane in 3D k-space, the information about the scene of interest is projected orthogonally onto this plane. Because of this projection 3D information about the scene is lost during the data collection process [1, 2], since the sampled area of k-space has no extent in the k_z dimension.

Resolution in the range direction is achieved by using high bandwidth waveforms combined with matched filtering, resolution in the cross range direction is achieved by synthesising a larger aperture in the along track direction. Hence to gain the ability to resolve targets in altitude, or the vertical cross range direction, a 2D aperture can be synthesised. Synthesising an 2D aperture in this way allows sampling of a volume of the 3D k-space, information about the 3D content of the scene is preserved and a 3D image can be reconstructed. To synthesise a 2D aperture in this way multiple passes of the scene to be imaged are required, from linear flight paths at varying altitudes as described earlier in the Chapter 2 [76–80]. Alternatively data collected from two passes from different slant angles can be combined using IFSAR [1, 70–72] or Stereo-SAR [73, 74] as described in Chapter 2.

However in military applications making several passes of a scene of interest may put the radar platform at risk, hence the ability to form SAR images containing information about the 3D content of the scene is a useful capability. Algorithms capable of forming a 3D SAR image from a single flight path are described in [4, 83, 85–92], this method involves the radar platform following an out-of-plane nonlinear flight path. Performing data collection from a flight path like this alters the shape of the data collection surface in k-space, the degree to which information about the 3D content of the scene is preserved is dependent upon the shape, dimensions and orientation of the sampled surface in k-space.

This chapter presents a method of forming 3D SAR images from nonlinear curved 3D flight paths using the Fourier transform to perform the image formation. The non-parametric image formation approaches in the literature focus on using matched filtering or convolution-back projection algorithms which are known to be computationally intensive in 2D SAR image formation, the computational load associated with these algorithms scales poorly with increasing scene size thus the introduction of another image dimension makes these algorithms less appealing [4].

The rest of this chapter is organised as follows; the second section describes the data collection surface sampled when following an out-of-plane nonlinear flight path along with how the shape of this data collection surface affects the properties of images formed when following this type of flight path. The third section introduces a 2D example which has the same properties as the 3D problem along with simulation results showing the resolution, position accuracy and point spread function achieved using different nonlinear apertures. In the fourth section of this chapter a 3D version of the Volterra mapping algorithm developed in Chapter 3 of this thesis is derived and simulation results from using this image formation technique from a nonlinear curved 3D flight path are presented, along with results from a simpler nearest neighbour interpolation process. Lastly a summary of the work contained in this chapter is presented.

4.2 3D data collection surface

The collected SAR signal used to form an image is as derived earlier in equations (2.21) and (2.22) which are re-written here:

$$S(\mathbf{k}) = \int_{-\infty}^{\infty} (A_t.A_0) \,.\mathrm{rect}\left(\frac{\hat{t} - \left(\frac{l_0}{c}\right)}{T_p}\right) .e^{j\mathbf{k}.\mathbf{x}} d\hat{t} \tag{4.1}$$

where A_t and A_0 are the amplitudes of the transmitted radar waveform and the reference waveform used to perform the deramp-on-receive operation respectively, $\hat{t}$ is the fast time variable, l_0 is the round trip distance to the scene centre, T_p is the width of the transmitted pulse, $\mathbf{x}$ is the position of a target in the scene with respect to scene centre,

When following an out-of-plane nonlinear flight path as shown in 4.1(a), which is chosen using the optimal flight path selection described in [4] and will be used throughout this chapter, the samples of this function are located in k-space on a 2D surface as shown in Figure 4.1(a), given

by:

$$\mathbf{k} = \omega \mathbf{u} \tag{4.2}$$

where

$$\omega(t, \hat{t}) = \frac{-2\pi}{c}\left(f_c + 2\mu\left(\hat{t} - \frac{l_0}{c}\right)\right). \tag{4.3}$$

where t is the slow time variable, f_c is the centre frequency of the radar waveform, μ is the chirp rate of the radar waveform used, c is the speed of light.

$$\mathbf{k} = [\mathbf{k}_x \quad \mathbf{k}_y \quad \mathbf{k}_z]^T \tag{4.4}$$

where $\mathbf{u}$ is the apparent look direction vector in the direction given by θ and ψ.

$$\mathbf{u} = \begin{bmatrix} \sin\theta\cos\psi \\ \cos\theta\cos\psi \\ \sin\psi \end{bmatrix} \tag{4.5}$$

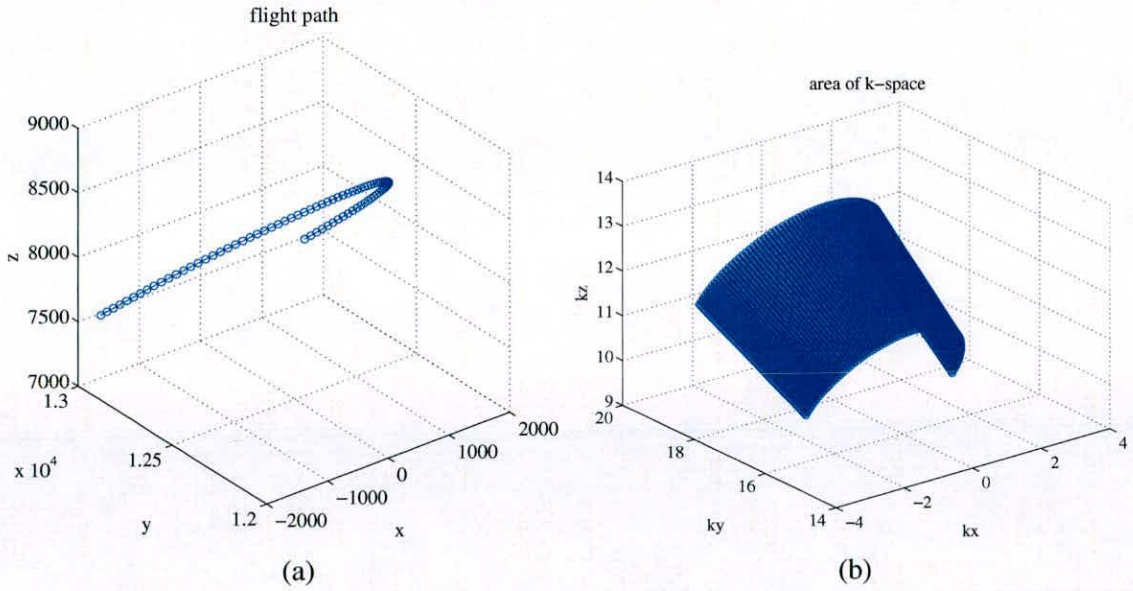

Figure 4.1: *(a) Curved 3D flight path, (b) resulting sampled 2D surface of 3D k-space.*

The resolution of the SAR image depends on the extent of this k-space data in each of the three k_x, k_y and k_z dimensions

$$\delta_x = \frac{2\pi}{\Delta X} \tag{4.6}$$

$$\delta_y = \frac{2\pi}{\Delta Y} \tag{4.7}$$

$$\delta_z = \frac{2\pi}{\Delta Z} \tag{4.8}$$

The size of scene that can be unambiguously sampled is related to the sample spacing in the k_x, k_y and k_z dimensions by

$$D_x = \frac{2\pi}{\Delta x} \tag{4.9}$$

$$D_y = \frac{2\pi}{\Delta y} \tag{4.10}$$

$$D_z = \frac{2\pi}{\Delta z} \tag{4.11}$$

4.3 2D simulation of 3D data surface

For Fourier reconstruction of the 3D scene the 2D surface in 3D k-space needs to be resampled to a uniform grid of samples to allow use of the computationally efficient FFT in all three dimensions. Hence the 3D resampling problem has some similarities to the resampling as part of the PFA as considered in Chapter 3, however the resampling from a 2D surface to a 3D grid of points is a new problem. This resampling operation to data points off the data collection surface can be considered separately to the other aspects of the 3D SAR resampling problem. The aim of this is to answer the question, can genuine interpolation rather than extrapolation be performed off the sampled data surface due to the surface curvature? To aid development of 3D SAR imaging techniques a 2D simulation of the 3D SAR resampling problem was developed, this simulation is designed to mimic the off surface part of the 3D resampling.

A simulated 2D area of k-space was generated for a simple 32m square scene containing a single point target displaced from the scene centre by 5m in both directions. The sampled area of k-space has extent in the k_x and k_y dimensions large enough to allow a 1m resolution SAR image to be formed. This sampled area of k-space is plotted in Figure 4.2(a) and the resulting SAR image, formed by windowing the data in both dimensions and performing a 2D FFT, is shown in Figure 4.2(b).

As stated in equations (4.6) to (4.11) it should be possible to sample k-space data on two orthogonal slices of k-space data and still form a SAR image of an extended scene with the full resolution defined by the extent of the two orthogonal slices in the k_x and k_y dimensions. The simple 2D area of k-space shown in Figure 4.2(a) was sampled onto an orthogonal aperture as shown in Figure 4.3, where the full signal in k-space is included for illustrative purposes

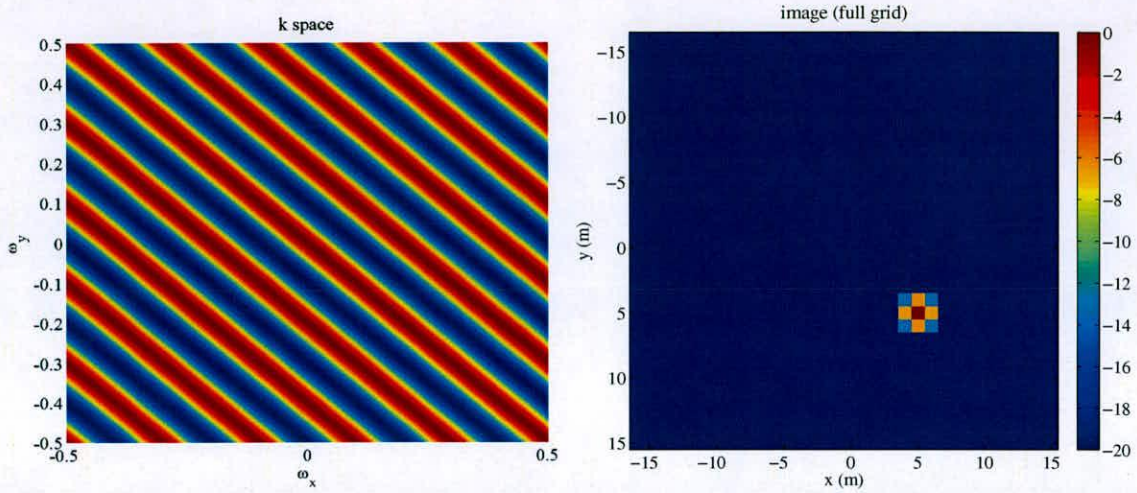

Figure 4.2: *(a) Full sampled volume of k-space and (b) the SAR image that can be formed using this data showing the point spread function.*

only. The orthogonally sampled data is only available at sample points lying on the orthogonal slices (shown in white) through this area of k-space shown. The data samples not lying on the orthogonal aperture were set to zero, zero padding the orthogonal aperture to the same size as the 2D area of k-space. A simulated SAR image was formed from this data using convolution back-projection, the result of this image formation process is shown in Figure 4.4(a). The simulated SAR image formed by performing a 2D FFT on the zero padded orthogonal aperture data is shown in Figure 4.4(b).

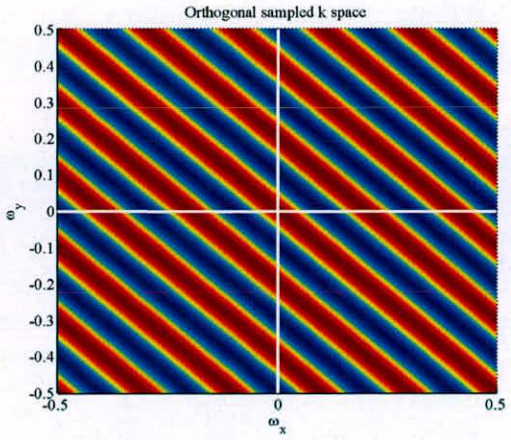

Figure 4.3: *Orthogonal sampling of k-space.*

The simulated SAR images in Figure 4.4 both place the target in the correct location within the reconstructed scene, in addition the target point spread function is nearly identical in both

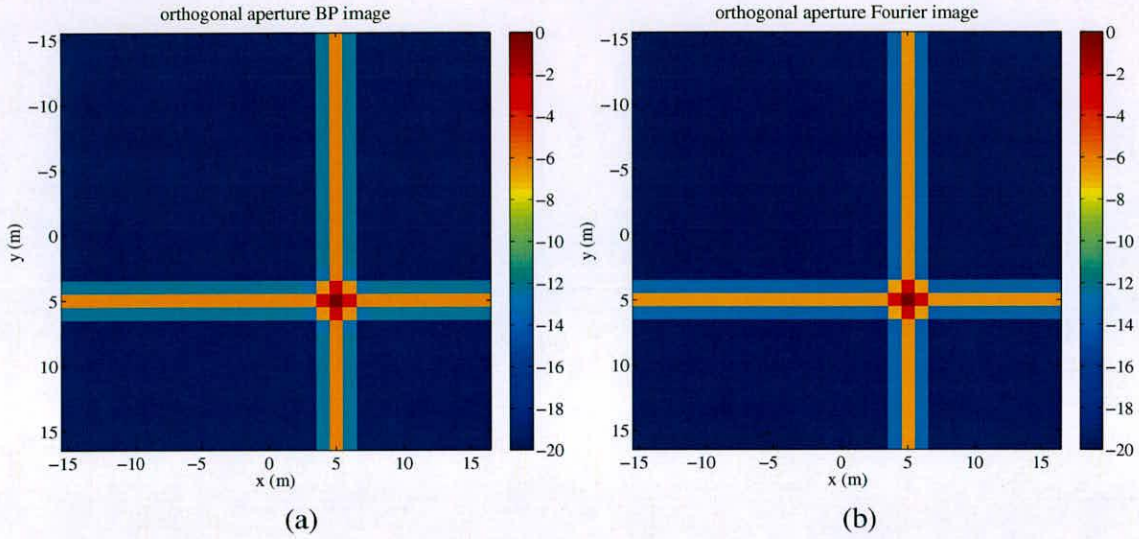

Figure 4.4: *SAR images formed from orthogonal sampled k-space data. (a) Using convolution back-projection, (b) using Fourier method.*

images. The psf is determined by the aperture shape, hence the psf is a $sinc(x)$ function in both images. However since the orthogonal aperture shown in Figure 4.3 doesn't sample the full volume of k-space, as in Figure 4.2(a), the majority of the data is padded with zeros. The fact that the area of k-space is sampled so sparsely results in psf sidelobes that are significantly higher than for the fully sampled k-space area. This simulation result confirms the result shown in [85].

4.3.1 Simulation results

The 2D simulation was extended to allow different data apertures to be used. Since the purpose of the 2D simulation is to aid the development of image formation techniques from 2D sampled data surfaces collected from nonlinear 3D curve flight paths, the apertures considered were a circular aperture and a semi-circular aperture. Similarly to the orthogonal aperture, the circular aperture samples the 2D area of k-space on a circular line with diameter matching the extent of the 2D k-space area, as shown in Figure 4.5(a), where the circular aperture is shown in white and the full area of k-space is included for illustrative purposes only. The sampled data used to form the SAR image is only available at points on this circle. A simulated SAR image was formed from this data using the convolution back-projection algorithm, shown in Figure 4.5(b). This image shows that despite the unconventional aperture shape the data sampled on the circular aperture is sufficient to form a SAR image with the same resolution as the orthogonal aperture.

In this case the psf is not a simple $sinc(x)$ function, due to the shape of the data aperture.

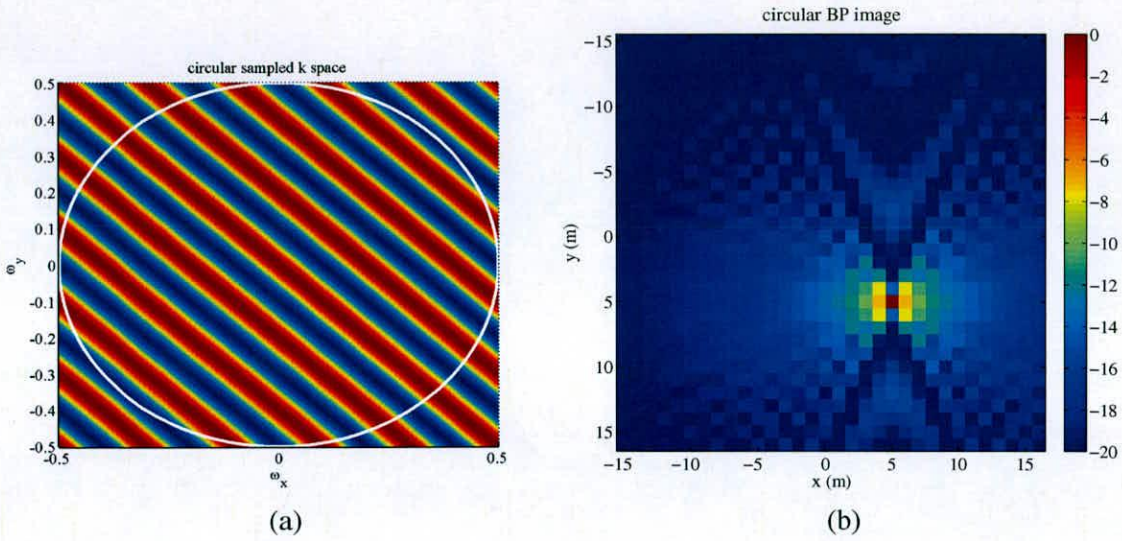

Figure 4.5: *(a) Circular sampled k-space data, (b) SAR image formed using convolution back-projection from circularly sampled k-space data.*

In order to form an image using the FFT from the data sampled on a circular aperture, the data must be resampled onto a regular rectangular grid. To perform this resampling the mapping concepts developed in Chapter 3 are used. In this case a version of the semi-analytic mapping was developed. The circular aperture was split at the minimum k_x value, and the circular sampling points mapped to a integer spaced points lying on a straight line. The angle and distance from the centre of the k-space data to the sample points on the circular aperture were used to perform the mapping of the known sample points as well as the desired sample points on the regular rectangular grid. After this mapping was performed, the data was resampled using the output centred $sinc(x)$ interpolation algorithm used in Chapter 3, as defined by equations (3.41) to (3.42).

The result of image formation using a 2D FFT after applying this semi-analytic mapping method is shown in Figure 4.6(a), along side the result achieved using a simple nearest neighbour interpolation algorithm to perform the interpolation without mapping, in Figure 4.6(b).

Both simulated SAR images show the target in the correct position within the scene, as well as achieving the same resolution. The point spread function of the target in the image formed using the semi-analytic mapping algorithm is similar to that in the image using CBP, however the sidelobes are not symmetric. The point spread function of the target in the image formed using the nearest neighbour interpolation algorithm is much less regular than in either of the

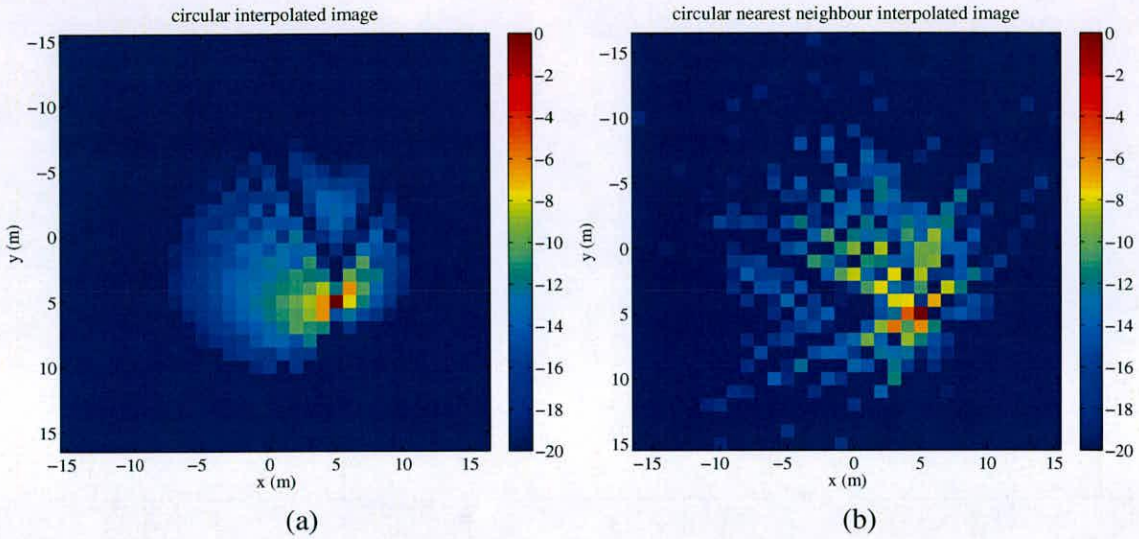

Figure 4.6: *SAR images formed using Fourier method from circular sampled k-space data, (a) using semi-analytic mapping, (b) using simple nearest neighbour interpolation.*

other two results. The point spread functions in the y direction of all three targets are plotted in Figure 4.7.

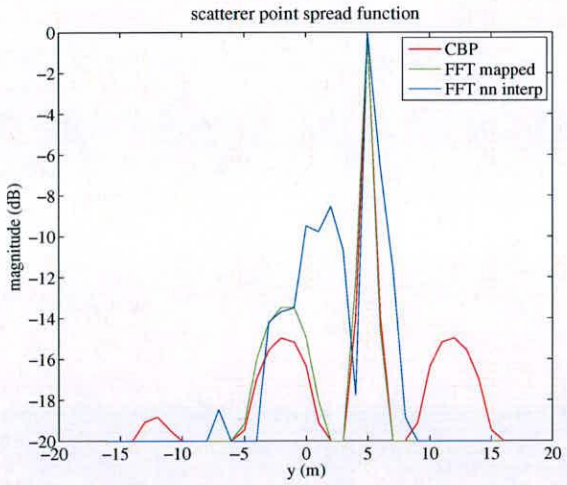

Figure 4.7: *Point spread function in the y-direction for each of the SAR image formation methods using circular sampled k-space data.*

The second aperture shape considered was a semi-circular aperture, since this is approximately the shape of the sampled 2D data surface shown in Figure 4.1(b). In this case the aperture was simply half of the circular aperture considered previously, this means the extent of the sampled k-space in the k_y direction is half that in the k_x direction. This means that the resolutions achievable are not equal, with twice the resolution in the y direction. The sampled area of k-

space and the semi-circular aperture are shown in Figure 4.8(a),where the semi-circular aperture is shown in white. Data is only available at sample points on this semi-circular aperture and the full area of k-space is shown for illustrative purposes only. The simulated SAR image formed using the CBP algorithm is shown in Figure 4.8(b).

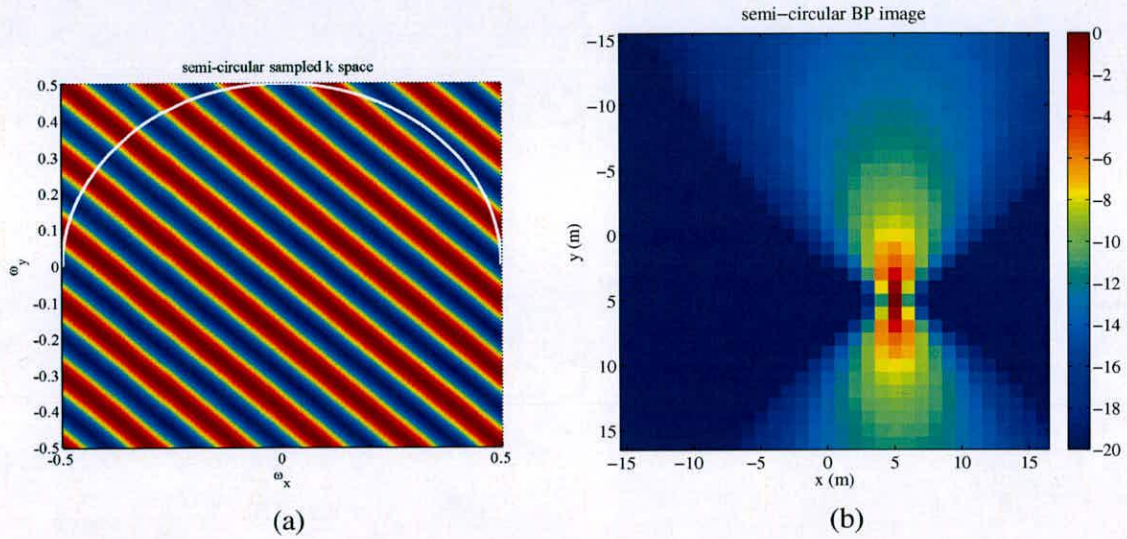

Figure 4.8: *(a) Semi-circular sampled k-space data, (b) SAR image formed using convolution back-projection from semi-circular sampled k-space data.*

The semi-analytic mapping algorithm and the nearest neighbour interpolation algorithm were used to form images from the semi-circularly sampled k-space data, the simulated 2D SAR images are shown in Figure 4.9. As in the circular aperture case all three algorithms place the target in the correct position within the scene and achieve the expected resolutions. As before the psf for the target in the image formed using the semi-analytic mapping algorithm is similar to the psf in the image formed using the CBP algorithm, where as the psf in the image formed using the nearest neighbour algorithm is less defined. The psf's in the y direction are plotted in Figure 4.10, where the irregular structure of the psf using the nearest neighbour interpolation can be seen to be lower in magnitude than the psf's using the other algorithms.

A second simulation was performed using data sampled on a semi-circular aperture, this time for a point target displaced further from the scene centre. Simulated data for a target displaced 25m from the centre of a 128m square scene was generated spanning the same extent of the 2D k-space as before. Simulated SAR images were formed using all three imaging algorithms considered in the previous examples, these images are shown in Figure 4.11. The image formed using CBP in Figure 4.11(a) places the target in the correct position and shows a similar psf to

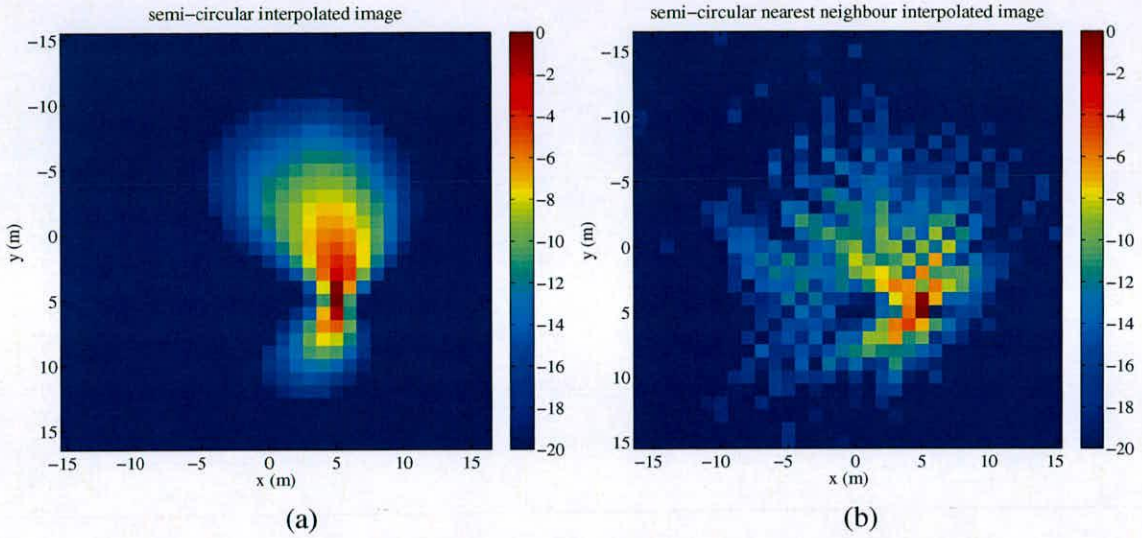

Figure 4.9: *SAR images formed using Fourier method from semi-circular sampled k-space data, (a) using semi-analytic mapping, (b) using simple nearest neighbour interpolation.*

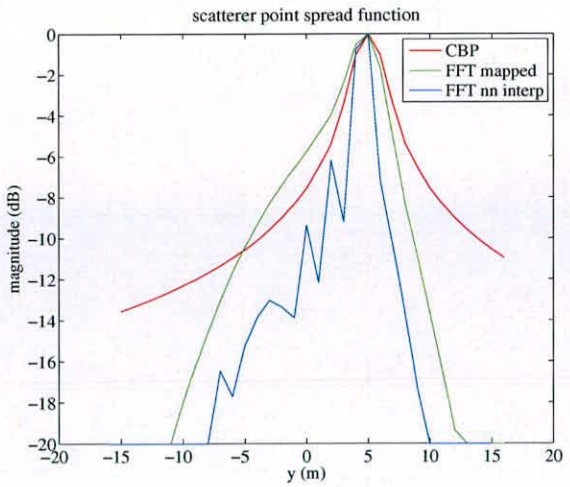

Figure 4.10: *Point spread function in the y-direction for each of the SAR image formation methods using semi-circular sampled k-space data.*

before, except for fringes near the edge of the larger scene. The image formed using the nearest neighbour interpolation method in Figure 4.11(c) places the target in the correct location and has a similar poorly defined psf structure as in the previous examples, however with the addition of a similar effect to the CBP near the edges of the larger scene. The image formed using the semi-analytic mapping algorithm in Figure 4.11(b) is much poorer than the other two images, the target is not focused successfully and is not centred on the correct location. The psf's in the y direction for the images formed using all three image formation methods are plotted in Figure 4.12.

4.3.2 Discussion

A 2D simulation of the off surface resampling problem in 3D SAR image formation was developed. This simulation was performed for k-space data of a simple scene using several different aperture shapes. Results were presented for orthogonally sampled k-space using CBP and a simple Fourier image, these images confirmed that the resolution of the SAR image is defined by the extent of the sampled k-space in the k_x and k_y dimensions. These results also showed that the shape of the point spread function is the same as for the full aperture case, however the psf sidelobes are higher.

A semi-analytic mapping algorithm based on the algorithm derived in Chapter 3 was developed. Simulated images formed from circular and semi-circular apertures using this method of image formation were compared to images formed using CBP and a nearest neighbour interpolation algorithm. Images formed using these methods were able to place the target in the correct position within the SAR image and the resolution achieved matched with the theory. The psf's of targets using these aperture shapes is less well defined than for the orthogonal or filled aperture cases and in the case of the nearest neighbour algorithm the psf has less apparent structure. These results showed that interpolation off the data collection surface is possible due to the curved shape of the aperture.

4.4 3D Volterra mapping method

The method used to perform the 3D resampling is based on the method developed in Chapter 3. The 2D surface of nonuniformly sampled data will be mapped to a 2D plane of uniformly sampled points. A grid of desired sample points surrounding the known samples is then mapped

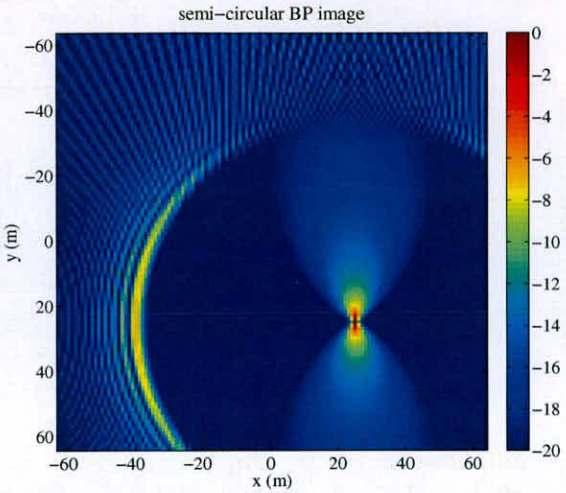

(a)

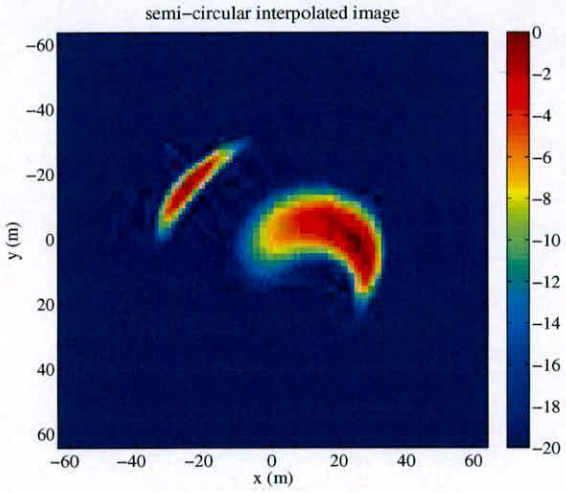

(b)

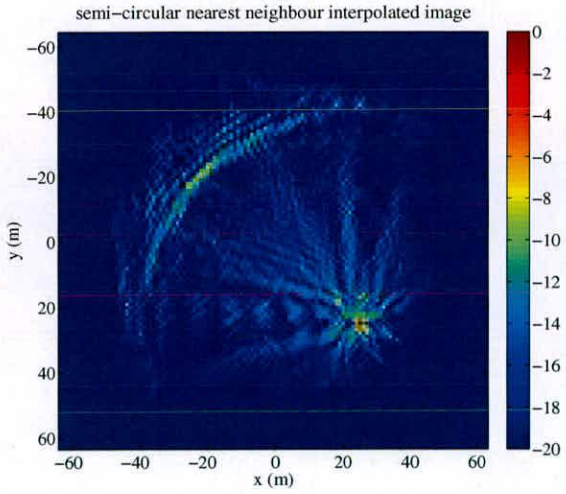

(c)

Figure 4.11: *Images formed from semi-circular sampled k-space data with larger scene extent, (a) using convolution back-projection , (b) using semi-analytic mapping and (c) using simple nearest neighbour interpolation.*

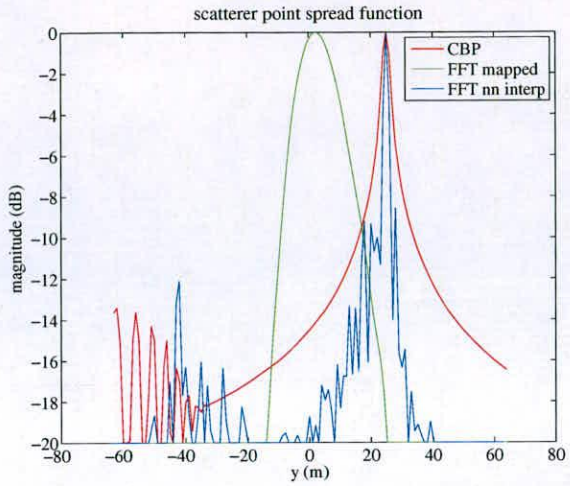

Figure 4.12: *Point spread function in the y-direction for each of the SAR image formation methods using semi-circular sampled k-space data with larger scene extent.*

to the same space.

$$\mathbf{k}' = f(\mathbf{k}) \tag{4.12}$$

where

$$\mathbf{k}' = \begin{bmatrix} \mathbf{k}'_x & \mathbf{k}'_y & \mathbf{k}'_z \end{bmatrix}^T \tag{4.13}$$

the target grid $\mathbf{k}'$ is chosen to be uniform and integer spaced for convenience. However, as in the 2D resampling another target grid could be chosen. For instance, a target grid aligned with the range, cross range and vertical cross range directions.

An affine mapping is performed as described in equations (3.9) to (3.12), a Volterra series is used to perform the mapping operation, a second order Volterra series is described here for illustrative purposes

$$\mathbf{k}'_x = a + a_0 k_x + a_1 k_y + a_2 k_z + a_{00} k_x^2 + a_{01} k_y^2 + a_{02} k_z^2 + a_{10} k_x k_y + a_{11} k_x k_z + a_{12} k_y k_z \ldots \tag{4.14}$$

which can be rewritten as a matrix equation:

$$\mathbf{k}' = \mathbf{K}\mathbf{a} \tag{4.15}$$

which has a least squares solution

$$\mathbf{a} = \left[\mathbf{K}^T\mathbf{K}\right]^{-1}\mathbf{K}^T\mathbf{k}'_x \tag{4.16}$$

Performing the resampling operation in this domain has many of the same advantages as in the 2D case; the interpolation function is identical at each sample position unlike on the original irregularly sampled surface. The interpolation function goes to zero at all the other sample positions and the interpolation separates into three 1D interpolation operations. Once the interpolation has been performed in the mapped domain, the resampled data is Fourier transformed using an FFT in each of the k_x, k_y and k_z directions to form a 3D image of the scene of interest.

4.4.1 Simulation results

An orthogonal surface with extent in all three dimensions was created, the orthogonal aperture is selected to have nominally the same extent in each dimension as the sampled area of k-space from the curved flight path, as shown in Figure 4.1 which is formed using the radar parameters specified in Table 4.1. This orthogonal aperture is determined by projecting the curved aperture onto each of the $k_x - k_y$,$k_x - k_z$ and $k_y - k_z$ planes. The orthogonal aperture used is shown in Figure 4.13(a), where the orthogonal aperture samples are plotted in different colours to help illustrate the data surface. The sample points in the $k_x - k_y$ plane are shown in green, the samples in the $k_x - k_z$ plane are shown in blue and the samples in the $k_y - k_z$ plane are shown in red.

Radar Parameters	Radar Parameters
$f_c = 1$ GHz	$B = 150$ MHz
$f_s = 0.55$ MHz	$T_p = 150\mu$ s
$\psi = 30^o$	$\Delta\psi = 5^o$
$\delta_x = \delta_y = \delta_z = 1$ m	$D_x = D_y = D_z = 80$ m
$R_0 = 15$ km	

Table 4.1: *Radar parameters used for 3D SAR simulation.*

The simulated sampled SAR data on the orthogonal aperture was generated for a single point target displaced 10 m from the scene centre in all three dimensions. The values of the data on the surface are calculated by;

$$s(t, \hat{t}) = e^{j\mathbf{k}.\mathbf{x}} \tag{4.17}$$

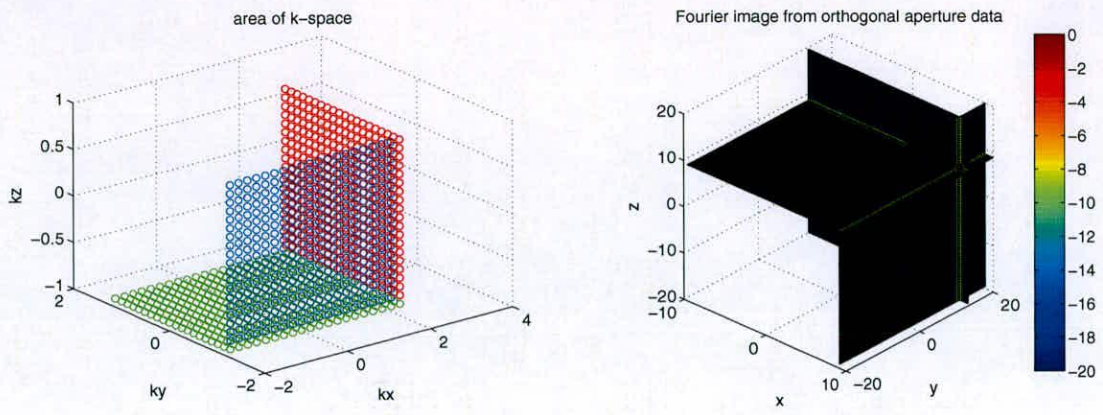

(a) (b)

Figure 4.13: *(a) Orthogonal 3D sampled data, (b) image formed by Fourier transforming orthogonal sampled data after zero-padding.*

To perform the image formation these samples are then loaded into a matrix of zeros and Fourier transformed in all three dimensions using an FFT. The resulting image is shown in Figure 4.13(b), where the plot shows the value of the full volume of the simulated 3D SAR image at slices through the image. The three slices are in the x-y plane, the x-z plane and the y-z plane and all three slices pass through the location of the target. As in the 2D example the target is located correctly in the scene, however since the aperture doesn't sample the full volume of data the point spread function takes the form of a $sinc(x)$ function in each dimension, with raised sidelobe levels.

The simulation was performed using the monostatic flight path shown in Figure 4.1(a) using the parameters specified in Table 4.1, which samples a 2D surface as shown in Figure 4.1(b). In this case the scene of interest consisted of a single point target displaced 20 m from the scene centre in all three dimensions. The extent of the surface in each of the k_x, k_y and k_z dimensions was determined and the maximum sample density in each dimension estimated, these parameters were used to determine the desired cube grid of points to which the resampling was performed. The 2D surface with the desired sample points are shown in Figure 4.14.

The affine and Volterra mapping stages discussed in section 4.4 were applied to the known data points on the 2D surface to determine the mapping coefficients to be used to move the data points from the data collection domain, to the domain in which the sampled data lies on an integer spaced uniform grid in the $k'_x - k'_y$ plane. These mapping coefficients were then applied to the desired cube of points to bring them into the same domain. Figure 4.15 shows

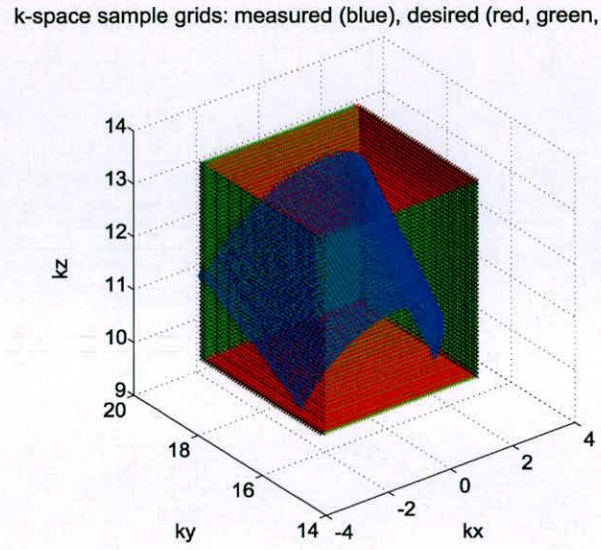

Figure 4.14: *Desired sample grid fully surrounding the 2D data surface in 3D k-space, sample grid surfaces are coloured differently to aid interpretation. The sampled 2D data surface is shown in blue. The desired sample grid top and bottom surfaces are marked in red, opposite faces are marked in green and black.*

the result of the mapping operation. The calculated rms error of the mapping operation is, $error_{rms} = 0.0874$.

After the mapping procedure the samples are interpolated using a $sinc(x)$ interpolation function as described in equations (3.41) and (3.42), extended to perform interpolation in all three dimensions. This interpolation is only performed for samples nearest to the data collection surface, all other points are assumed to be zero valued. To perform the image formation these samples are then Fourier transformed in all three dimensions using an FFT. The resulting simulated SAR image is shown in Figure 4.16, where pixels with values below -12dB have been made transparent to allow the 3D point spread function of the target to be seen since the resulting SAR image contains data at all points in the 3D volume defined by the scene of interest.

Slices through the target point spread function in each of the $x-y$, $x-z$ and $y-z$ dimensions are shown in Figure 4.17. These slices show that the image formation process has located the target at the correct location in the scene, and also show the point spread function in each plane in the image domain.

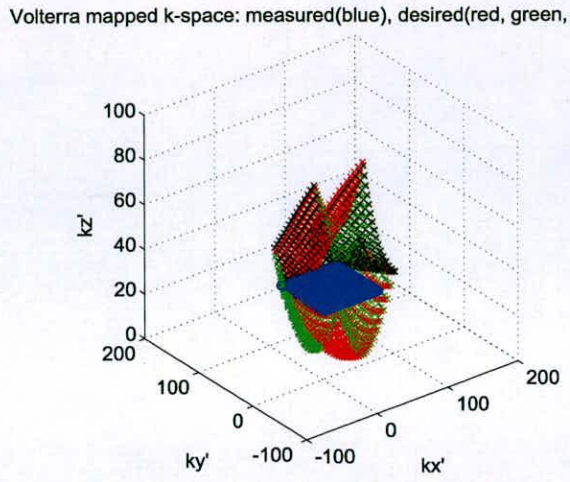

Figure 4.15: *Desired sample grid fully surrounding the 2D data surface in 3D k-space after 3D Volterra mapping, sample grid surfaces are coloured differently to aid interpretation. The sampled 2D data surface is shown in blue. The desired sample grid top and bottom surfaces are marked in red, opposite faces are marked in green and black.*

4.4.2 3D nearest neighbour resampling

Using the same flight path and sampled data surface as shown in Figure 4.1 an alternative method of 3D image formation was implemented. Instead of performing the interpolation in the mapped domain using $sinc(x)$ interpolation, the sampled k-space data was resampled to the nearest points in the cube of desired sample points using a simple nearest neighbour scheme. Again all other sample points in the desired sample grid are assumed to be zero valued. This resampled data was then Fourier transformed in each dimension using an FFT in exactly the same way as for the 3D Volterra mapping algorithm.

The resulting simulated 3D SAR image is shown in Figure 4.18, where pixels with values of less than -12dB have been made transparent. Slices through the target point spread function in each of the $x-y$, $x-z$ and $y-z$ dimensions are shown in Figure 4.19. These slices show that the image formation process has located the target at the correct location in the scene, and also show the point spread function in each plane in the image domain.

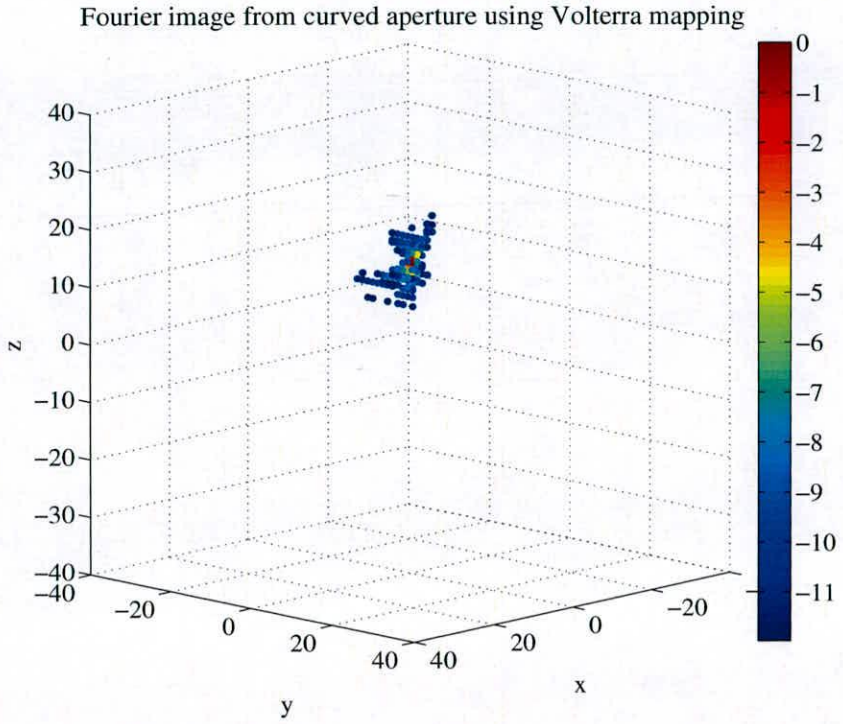

Figure 4.16: *3D scatter plot showing resulting 3D SAR image using 3D Volterra mapping and resampling, values less than -12dB have been made transparent to aid visualisation.*

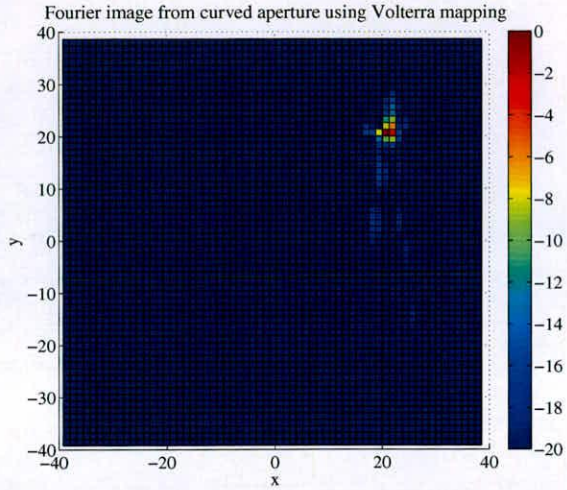

(a)

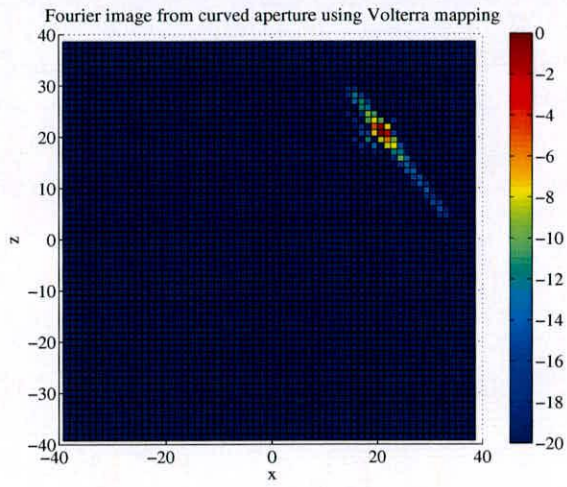

(b)

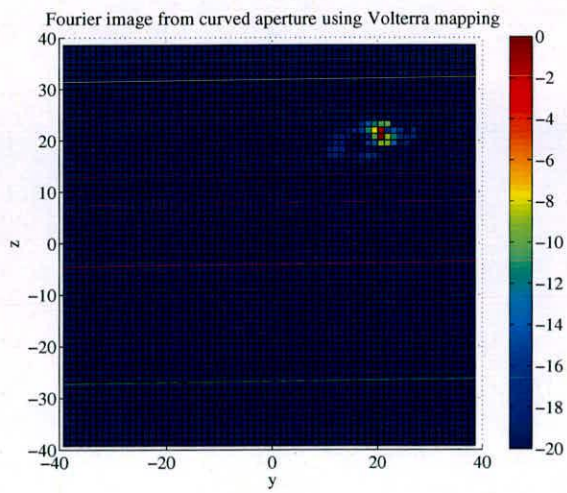

(c)

Figure 4.17: *Slices through full volume of the 3D SAR image formed using Volterra mapping and resampling, (a) x-y plane, (b) x-z plane, (c) y-z plane.*

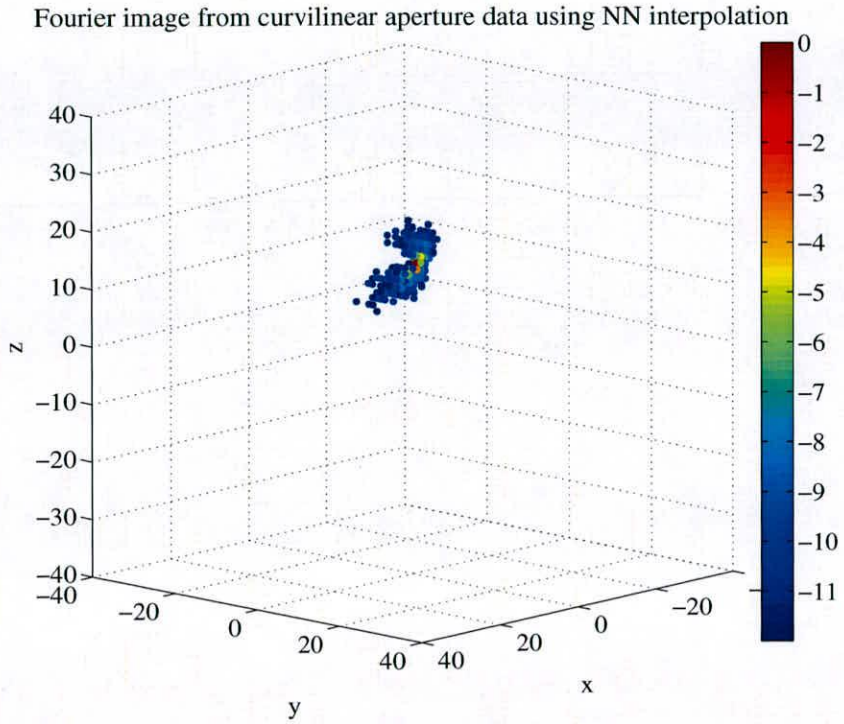

Figure 4.18: *3D scatter plot showing resulting 3D SAR image using nearest neighbour interpolation, values less than -12dB have been made transparent to aid visualisation.*

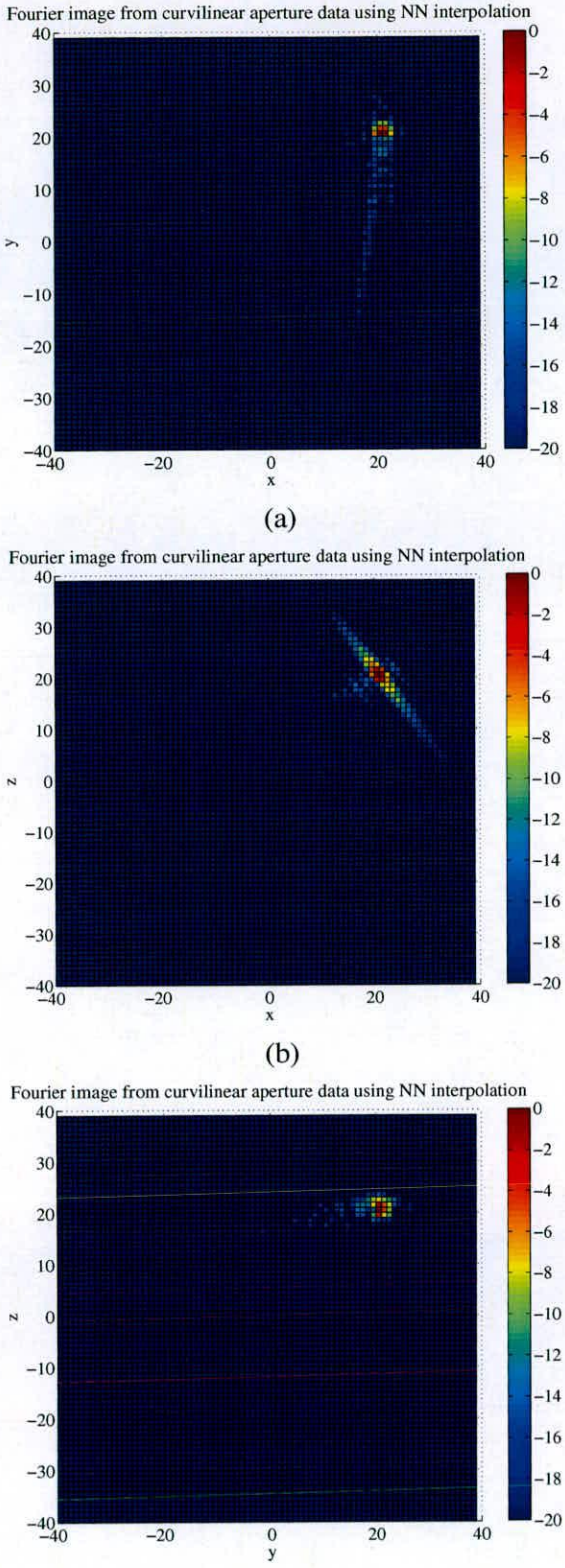

Figure 4.19: *Slices through full volume of the 3D SAR image formed using nearest neighbour interpolation, (a) x-y plane, (b) x-z plane, (c) y-z plane.*

4.4.3 Discussion

A method for forming 3D SAR images from out-of-plane nonlinear flight paths, using Fourier imaging techniques has been derived. This image formation algorithm is a 3D extension of the 2D Volterra mapping algorithm developed in Chapter 3. Simulation results showing that Fourier imaging is possible from 3 orthogonal planes of data with extent in each dimension in k-space were presented. These results show that the extent of the sampled surface of k-space in each dimension defines the resolution achievable, as demonstrated in the 2D example.

Simulation results of applying this image formation technique to data collected from an out-of-plane nonlinear flight path were presented, these results showed that targets in the scene of interest are placed in the correct position within the 3D SAR image and have the resolution expected. In addition, image formation from the same data was performed using a nearest neighbour interpolation algorithm. The result of using this image interpolation algorithm matches the performance of the 3D Volterra mapping algorithm well. The point target in the scene of interest is placed correctly in the scene and the same image resolution is achieved as using the 3D Volterra mapping algorithm. These results show that the off surface interpolation is possible because of the curved shape of the data collection surface.

This method of forming 3D SAR images is simple and computationally efficient, however the target point spread function is irregular in shape due to the shape of the data collection surface and the sidelobe levels are higher than could be achieved with a sampled volume of k-space.

4.5 Summary

In this chapter a method for forming 3D SAR images from 3D curved flight paths using Fourier methods has been presented. Collected SAR data from 3D curved flight paths lies on a 2D surface in the 3D k-space, this surface has extent in all three dimensions. Since image resolution is dependent upon the extent of the k-space data in the direction of interest, it is possible to form a SAR image with resolution in all three dimensions from a single flight path.

A method for performing the necessary resampling from the 2D surface to a cube grid of desired sample points surrounding the data is proposed. This resampling operation is more challenging than in the 2D SAR case where the data lies on a plane and interpolation is performed on this plane. In the 3D case the resampling operation has two facets, firstly the irregular to regular grid

sampling problem as considered in Chapter 3 and also the additional problem of interpolating the data off the 2D surface to the points on the desired sample grid.

To aid development of algorithms for the 3D problem a simple simulation of the off surface interpolation problem was developed. Results from this simulation were presented which demonstrated that it is possible to resolve targets using data sampled on orthogonal lines in the 2D k-space, the image resolution is the same as for a fully sampled k-space grid since the orthogonal aperture has the same extent in each of the k_x and k_y dimensions. The resulting images have high sidelobe levels however targets in the scene are located in the correct position.

This simulation was then extended to consider other aperture shapes. Results from applying a convolution back-projection (CBP) image formation algorithm to data from a circular aperture in k-space were presented. These were compared to images formed using a Fourier image formation algorithm based on the semi-analytic mapping algorithm presented in Chapter 3, where the angle and radius of the circular aperture are used to perform the mapping. Results were also presented for a simple nearest neighbour interpolation scheme. These results showed that all three image formation methods were able to place the target in the scene at the correct position and all three algorithms achieved similar resolutions. Similar results were presented using a semi-circular sampled are of k-space. Results from simulation of a larger scene showed that the CBP and nearest neighbour interpolation algorithms produced similar results with the target in the correct position, however the result from the semi-analytic mapping showed the target in the wrong position and very blurred.

A 3D version of the Volterra mapping algorithm developed in Chapter 3 was derived, where an affine mapping and a Volterra series based mapping are performed by calculating a least squares estimate of the mapping coefficients used to map the 2D surface in k-space to a plane in the mapped domain. The target grid is assumed to be a uniformly sampled cube of data points surrounding the known data values.

Results from a 3D SAR simulation were presented, firstly from a 3D orthogonal aperture which showed the equivalent result to the orthogonal aperture in 2D. Again the target was placed in the correct position with high point spread function sidelobes. This simulation was then extended to perform the 3D Volterra mapping on simulated SAR data from a 3D curved flight path. Results were presented using the 3D Volterra mapping algorithm and also a nearest neighbour interpolation scheme. Both algorithms placed the target in the correct position and had similar

point spread functions.

Chapter 5
Conclusions

In the introduction chapter the motivation behind the research presented in this thesis was discussed and the aims of the research stated. In this chapter the aims of the work will be reviewed based on the work presented in the previous chapters and the main acheivements of the research presented will be restated.

The rest of this chapter will be organised as follows, the first section will review the aims of the research as discussed in the introductory chapter of the thesis. The major achievements of the research will be discussed, identifying the achievement of the goals set as stated at the beginning of the research. In the second section of this chapter the limitations of the work as presented are discussed and how the work is still relevent in spite of these limitations. The last section of this chapter will discuss possible future directions of the research presented in this thesis.

5.1 Aims and achievements of the project

The motivations behind the research presented in this thesis were to provide the ability to form SAR images from manoeuvring platforms, due to the added survivability this would provide in military applications. Due to the potential for improved survivability by pairing a passive receiving platform with a transmitting platform at a safe stand-off range, bistatic SAR provides improved survivability over traditional monostatic SAR.

The observation was made that the conventional keystone resampling method used as part of the PFA made use of the assumption that the slow time resampling operation can be considered locally uniform, allowing use of the same interpolation function. However for manoeuvring radar platforms this approximation becomes less valid with increasing along track platform acceleration. The samples in the slow time direction are increasingly nonuniformly spaced. Therefore the first aim of the work presented in this thesis was to develop nonlinear mapping techniques to provide a simple and accurate method for performing resampling of the irregularly sampled data typically generated by bistatic and manoeuvring radar platforms. Three

mapping methods were developed in chapter 3 of this thesis, a Volterra series based mapping algorithm, an analytic mapping algorithm and a semi-analytic mapping algorithm.

A Volterra series mapping algorithm consisting of a 2D affine mapping and calculation of mapping coefficients of a limited order Volterra series, which are used to map the known samples to a domain where they are uniformly sampled on an integer spaced rectangular grid, by a least squares estimate is performed. These mapping coefficients are then used to map a grid of desired sample positions surrounding the data, with sample density equal to the estimated maximum sample density in each of the k_x and k_y dimensions, to the same domain. The objective of performing this mapping operation is to allow a simpler resampling process. In this mapped domain the resampling can be performed using the same interpolation function at all sample points in the data, where this was not possible in the k-space domain. This interpolation function can easily be made to go through zero at all the other known sample points. In addition, due to the mapping operation the 2D interpolation is separable into two 1D interpolations. This method was performed on several simulated bistatic and monostatic SAR data-sets. These results showed that no additional benefit in terms of mapping accuracy was achieved by using higher than third order terms in the Volterra series used. In addition, by calculating the rms error involved in the mapping operation the results showed that the Volterra mapping algorithm is capable of performing accurate mapping for data collected in many SAR geometries. However, a computational cost analysis showed that this mapping operation is computationally intensive due to the requirement to calculate the inverse of a large matrix. This complexity is due to the generality of the algorithm and the fact that it can be used to perform accurate mapping of arbitrarily complex sample grids provided that terms of a high enough order are used in the Volterra series.

A more limited mapping algorithm which makes use of the limited complexity of the collected SAR data was derived. In SAR data the samples lie on lines defined by the look direction vector at each pulse repetition interval, with a bandwidth compression on each pulse based on the particular bistatic geometry. This analytic mapping algorithm is based on inverting the inherent mapping operations in the PFA. The mapping method was shown to be an accurate method for performing the nonlinear 2D mapping operation. In addition the computational cost analysis shows that the analytic mapping method is more compuationally efficient than the Volterra mapping algorithm. However for increasingly complex platform manoeuvres the analytic inversion of the PFA mapping becomes extremely challenging as higher order terms

are required. To avoid the need for accurate description of the platform motion a semi-analytic mapping algorithm was derived. This mapping algorithm uses the look direction vector **u** as an intermediate function, which is interpolated to perform the mapping from k-space to the uniformly sampled grid. This algorithm was shown to be a robust method for performing the mapping operation. Although the overall accuracy achieved was not as good as the analytic mapping, this algorithm could be applied to an arbitrarily complex platform motion without the need to perform another anayltic inversion of the PFA mapping.

The image quality achieved using the semi-analytic mapping method and the output centred or inverse interpolation procedure to perform the PFA resampling operation was compared to that achieved using the keystone resampling method for simulated SAR data from manoeuvring platforms. These results showed that the image quality of images formed using the keystone method was significantly poorer than that of images formed using the semi-analytic mapping algorithm. This is one of the major achievements of the research presented in this thesis. A robust method of forming SAR images from manoeuvring bistatic SAR geometries has been developed and demonstrated to achieve better performance than the conventional method presented in the literature.

With increased platform survivability providing the motivation for the majority of the research presented in this thesis, the ability to obtain information about the height of targets in a scene using a single SAR data collection period instead of requiring multiple passes of the scene is a useful capability. The second aim of this research was to develop a method of forming 3D SAR images from a single SAR data collection flight path using Fourier imaging techniques instead of the more computationally complex CBP algorithm considered in the literature.

As part of the development of a Fourier based 3D SAR image formation processor a 2D example which has the same properties as the 3D resampling problem was developed. Using this 2D example the 3D SAR problem was demonstrated, the ability to resolve targets using data sampled on an orthogonal 2D aperture was demonstrated. Images formed in this way show the raised point spread function sidelobes as described in the literature. A semi-analytic mapping method similar to that developed in Chapter 3 was developed, using the radius and angle to samples on the data collection surface to perform the mapping. Results of image formation using this algorithm were presented and compared to results from applying the CBP algorithm and a nearest neighbour interpolation Fourier algorithm. These results showed that the semi-analytic mapping method was able to resolve targets with comparable resolution to that achieved using

the CBP algorithm as well as the nearest neighbour interpolation algorithm. Targets are placed in the correct position within the resulting image using all three algorithms. Results were presented for all three image formation algorithms for data sampled on circular and semi-circular surfaces and the resulting point spread functions compared. The Fourier methods were shown to approximate the CBP result, however with a more irregular point spread function, in particular the point spread function achieved using the nearest neighbour method was shown to have an irregular structure and high sidelobes. These results demonstrated that it is possible to perform interpolation off the data collection surface as required in the 3D SAR case, this interpolation is not extrapolation since the interpolation consists of the weighted sum of the contributions from several nearby samples due to the aperture shape.

After proving this concept using the 2D example a 3D SAR simulation was developed showing the result of image formation from a 3D orthogonal aperture. This image showed the same point spread function as indicated in the 2D example. A 3D extension of the Volterra mapping algorithm presented in Chapter 3 was derived. In this algorithm the sampled 2D surface is mapped to a plane in a domain where it is regularly sampled on an integer spaced uniform grid. The mapping coefficients used to perform this mapping are then used to map a cube of desired data points surrounding the 2D surface in k-space to the same domain. In this domain the intepolation operation has the same desirable qualities as in the 2D mapping case, the 3D interpolation is separable into three 1D interpolation operations using the same interpolation function at all sample points, which passes through zero at all other known samples. Results of applying this mapping algorithm to simulated 3D SAR data collected from a 3D curved flight path were presented. These results showed that the algorithm was able to place the target in the correct position within the scene and the point spread function achieved was plotted both as a 3D plot and as slices through the target in each of the $x-y$, $x-z$ and $y-z$ planes. This result was compared to the point result of applying the nearest neighbour interpolation algorithm, which achieved a similar result. This result is the second major achievement of the rsearch presented in this thesis, a Fourier method of forming 3D SAR images from a sampled 2D surface of data with extent in all three dimensions in k-space has been developed and demonstrated to localise the energy from a target in the correct location within a 3D image.

5.2 Limitations of the project

One of the limitations of the work presented in this thesis is that none of three 2D mapping algorithms developed in chapter 3 was demonstrated to perform extremely accurate mapping in all of the SAR data collection scenarios considered. However the simulation results presented for the semi-analytic mapping method showed that the algorithm is robust under a large variety of bistatic angles, $\beta = 0^o, 30^o, 60^o, 90^o$, and accelerations, $a_r = 0, 10, 20, 30$ ms^{-1}. Even though the rms error may seem large, the effect of this mapping error on image quality is shown as raised sidelobe levels which results in poorer image contrast instead of appearing as image artefacts, as demonstrated in images with the keystone resampling.

A second limitation of the work presented is that results from the 2D example of the 3D SAR problem show that for large target displacements from the scene centre, images formed using the semi-analytic mapping method are poor, placing targets in the wrong position and with a large amount of blurring. This problem may also affect the 3D Volterra mapping algorithm, however it appears that the nearest neighbour interpolation is robust in these cases. As in the 2D PFA there will be a limit on the scene size that can be imaged using the 3D version of the PFA, while minimising phase errors. What this limit is has not been determined. However it is assumed that the extent of the scene that is of interest in the z-direction will be an order of magnitude less than in the x and y directions. Since it is typical for spotlight SAR scenes to be approximately 1km in each of the x and y directions, however most targets of interest will be much smaller than this in the z direction, more likely a few tens of metres.

5.3 Implementation issues

It is pertinent at this stage to consider the possible issues surrounding implementation of the algorithms developed in this thesis in real radar systems. However to some extent this is a difficult topic to provide definite answers to, since the solution used in any real system should be the one which best meets the requirements of that particular radar system. Without any strict system requirements to work to the discussion contained in this section will consider the implementation of the algorithms developed in this thesis to a general radar system and try to cover the issues involved in the selecting which algorithms are best suited to implementation in a real radar system.

The general 2D mapping method of performing the interpolation required by the PFA for SAR image formation would provide a simple solution to the irregular to regular data resampling problem, which is often performed using the keystone resampling method. As such the 2D mapping algorithms could be implemented in a relatively straight forward manner simply by replacing the keystone resampling software with software designed to perform the interpolation using the 2D mapping method. For a general implementation of the 2D mapping method the analytic mapping algorithm is the least simple to implement directly since this algorithm requires an accurate mathematical description of the radar platform flight path, as discussed in chapter 3. However the Volterra series and the semi-analytic mapping algorithms both provide a general solution to the 2D mapping problem and as discussed in chapter 3 the choice of which of these algorithms is best suited to implementation in a real radar system is likely to be dependent upon the system requirements. The semi-analytic mapping algorithm is likely to be easy to implement using precomputed look-up tables and hence would most likely provide a faster implementation than the Volterra series mapping which involves the calculation of the inverse of a large matrix.

The 3D mapping algorithm developed in chapter 4 is more speculative than the 2D mapping algorithms, since at present it is unclear if 3D SAR image formation from nonlinear flight paths has been implemented in production radar systems. However since curvilinear SAR does provide 3D SAR image formation from only a single pass from a single radar antenna equipped platform it does provide a useful capability in situations where the more conventional interferometric SAR would require multiple passes of the scene. The 3D mapping algorithms developed in this thesis could provide a simple computationally efficient method for 3D SAR image formation. However the most likely difficulty in operating in this mode would be the ability to fly along the prescribed nonlinear flight path. Since the effect of deviation from this flight path has not been considered in this thesis. In addition to this the 3D SAR image is difficult to easily represent in on a conventional radar display, this issue presents a challenging problem in extracting useful image about a target scene from the 3D SAR scene reconstruction.

5.4 Future extension of the work

There are several possible directions that this work could be extended in with further research. The 2D mapping algorithms have been demonstrated for manoeuvring platforms in a bistatic geomtery, however as suggested in Chapter 3 these mapping algorithms could be applied to

other irregular sampling problems in SAR. For example in military applications it is known that SAR systems utilise pulse 'jitter', where the pulse repetition interval is deliberately varied to make it more difficult for the enemy to use sophisticated jamming techniques. For instance, sampling the transmitted pulse waveform and transmitting it back to the imaging radar delayed to place false targets in the scene or to conceal targets. Deliberate variation of the pulse repetition interval in this way will mean the sampled area of k-space collected will be even more irregularly sampled than in the accelerating platform case. Application of the mapping methods to the interpolation used to form images from this pulse 'jitter' would be an interesting area of further work.

Another potential application of the 2D mapping work would be in image formation from interrupted or discontinuous SAR data, for instance from multistatic SAR systems or multiple passes of the same scene by a single platform. In these situations a simple method for forming an image by combining the data from several discontinuous sampled areas of k-space would be an attractive capability. Images formed in this way might contain extra information about the scene of interest since some surfaces of the target will reflect more energy from certain viewing angles. Hence, combining the data collected from different platforms may improve performance of ATR algorithms since a more complete picture of targets in the scene is formed. In addition to this it is much less likely that targets in the scene will be occluded by shadowing in the resulting image since the scene has been illuminated from several angles.

The work on 3D SAR image formation could also be extended. For instance, a comparison of computational cost and image quality achieved using the 3D Fourier method developed in this thesis and using 3D CBP would be pertinent. This would help determine the quality of the results achieved using the 3D Fourier method. In addition to this, further investigation into the scene size limit in the z direction using the 3D Fourier method would be relevant in order to determine the range of applicability of the method.

Another area of interesting research for the 3D SAR work would be investigating the effect of platform motion errors in the 3D data collection geometry. In conventional 2D SAR, platform motion errors are exhibited as a blurring of all the targets in the image. However this blurring function can be removed using autofocus algorithms as discussed in Chapter 2. An investigation into how platform motion errors affect 3D SAR images and how these errors can be corrected using data driven autofocus techniques such as the phase gradient algorithm would be an important area of research, since without autofocus SAR images are generally of poor

quality and the ability to correct these errors would make 3D SAR from curved flight paths much more appealing.

References

[1] C.V. Jakowatz Jr, D. Wahl, P. Eichel, D. Ghiglia, and P. Thompson, *Spotlight-Mode Synthetic Aperture Radar: A Signal Processing Approach.* Boston, MA, USA: Kluwer Academic Publishers, 1996.

[2] W. Carrara, R. Goodman, and R. Majewski, *Spotlight Synthetic Aperture Radar Signal Processing Algorithms.* Artech House, 1995.

[3] R. Crochiere and L. Rabiner, "Interpolation and decimation of digital signals a tutorial review," *Proceedings of the IEEE*, vol. 69, pp. 300–331, March 1983.

[4] B. Rigling and R. Moses, "Flight path strategies for 3-d scene reconstruction from bistatic sar," *IEE Proceedings on Radar, Sonar and Navigation*, vol. 151, pp. 149–157, June 2004.

[5] R. James, "A history of radar," *IEEE Transactions on Aerospace and Electronic Systems*, vol. 35, pp. 343–349, October 1989.

[6] M. Skolnik, "Radar in the twentieth century," *IEEE Transactions on Aerospace and Electronic Systems*, vol. 15, pp. 27–46, October 2000.

[7] G. Stimson, *Introduction to Airborne Radar.* Scitech, 1989.

[8] J.T. Johnson, I.J. Gupta and R.J. Burkholder, "Comparison of monostatic and bistatic radar images," in *IEEE Antennas and Propagation Society International Symposium 2001*, vol. 4, pp. 281–284, July 2001.

[9] H. Griffiths, "From a different perspective: Principles, practice and potential of bistatic radar," in *IEEE Radar Conference RADAR 2003*, pp. 3–5, September 2003.

[10] R. Burkholder, I. Gupta, and J. Johnson, "Comparison of monostatic and bistatic radar images," *IEEE Antennas and Propagation Magazine*, vol. 45, pp. 41–50, June 2003.

[11] M. Lowe, "Algorithms for high resolution bistatic sar," in *IEEE Radar Conference RADAR 2002*, pp. 512–515, October 2002.

[12] B. Rigling and R. Moses, "Polar format algorithm for bistatic sar," *IEEE Transactions on Aerospace and Electronic Systems*, vol. 40, pp. 1147–1159, October 2004.

[13] Y. Neo, F. Wong, and I. Cumming, "Focusing bistatic sar images using non-linear chirp scaling," in *IEEE International Radar Conference, RADAR 2004*, 2004.

[14] I. Walterscheid, J.H.G. Ender, A.R, Brenner, and O. Loffeld, "Bistatic sar processing using an omega-k type algorithm," in *Proceeding of the 2005 IEEE International Geoscience and Remote Sensing Symposium, IGARSS-2005*, vol. 2, pp. 1064–1067, July 2005.

[15] I. Graham, "Looking back: Some radar collections," *IEEE Potentials*, vol. 18, pp. 40–42, December 1999.

[16] "IEEE standard radar definitions," *IEEE Standard 686-1997*, 1998.

[17] A. Horne and G. Yates, "Bistatic synthetic aperture radar," in *IEEE Radar Conference RADAR 2002*, pp. 6–10, October 2002.

[18] O. Loffeld, H. Nies, V. Peters, and S. Knedlik, "Models and useful relations for bistatic sar processing," *IEEE Transactions on Geoscience and Remote Sensing*, vol. 42, pp. 2031–2038, October 2004.

[19] F. Comblet, F. Pellen, A. Baussard, and A. Khenchaf, "Bistatic sar: Theory and simulation," in *IEEE Antennas and Propagation Society International Symposium 2005*, vol. 2A, pp. 664–667, July 2005.

[20] G. Yates, A. Horne, A. Blake, and R. Middleton, "Bistatic sar image formation," *IEE Proceedings on Radar, Sonar and Navigation*, vol. 153, pp. 208–213, June 2006.

[21] M. Soumekh, "Bistatic synthetic aperture radar inversion with application in dynamic object imaging," in *IEEE International Conference on Acoustics, Speech and Signal Processing, (ICASSP-91*, vol. 4, pp. 2557–2580, April 1991.

[22] M. Soumekh, "Bistatic synthetic aperture radar inversion with application in dynamic object imaging," *IEEE Transactions on Signal Processing*, vol. 39, pp. 2044–2055, September 1991.

[23] L. Cosart, L. Peregrino, and A. Tambe, "Time domain analysis and its practical application to the measurement of phase noise and jitter," *IEEE Transactions on Instrumentation and Measurement*, vol. 46, pp. 1016–1019, August 1997.

[24] M. Eineder, "Oscillator clock drift compensation in bistatic interferometric sar," in *IEEE International Geoscience and Remote Sensing Symposium, IGARSS-03*, vol. 3, pp. 1449–1451, 2003.

[25] M. Weiß, "Synchronisation of bistatic radar systems," in *IEEE International Geoscience and Remote Sensing Symposium, IGARSS-04*, vol. 3, pp. 1750–1753, 2004.

[26] M. Jahangir, "Moving target detection for synthetic aperture radar via shadow detection," in *IET International Conference on Radar Systems Radar 2007*, October 2007.

[27] M. Pettersson, "Extraction of moving ground targets by a bistatic ultra-wideband sar," *IEE Proceedings on Radar, Sonar and Navigation*, vol. 148, pp. 35–40, February 2001.

[28] M. Cheney, "A mathematical tutorial on synthetic aperture radar," *Society for Industrial and Applied Mathematics Review*, vol. 43, no. 2, pp. 301–312, 2001.

[29] D. Ausherman, A. Kozma, J. Walker, H. Jones, and E. Poggio, "Developments in radar imaging," *IEEE Transactions on Aerospace and Electronic Systems*, vol. 20, pp. 363–396, July 1984.

[30] D.C. Munson Jr, J.D. O'Brien and W.K. Jenkins, "A tomographic formulation of spotlight-mode synthetic aperture radar," *Proceedings of the IEEE*, vol. 71, August 1983.

[31] C. Oliver, "Synthetic aperture radar imaging," *Journal of Physics. D: Applied Physics*, vol. 22, pp. 871–890, 1989.

[32] J.H.G Ender, "Invited lecture - the meaning of k-space for classical and advanced sar techniques," in *Physics in Signal and Image Processing, PSIP 2001*, pp. 23–38, January 2001.

[33] Y. Yuan, J. Sun, and S. Mao, "Pfa algorithm for airborne spotlight sar imaging with non-ideal motions," *IEE Proceedings on Radar, Sonar and Navigation*, vol. 149, pp. 174–182, August 2002.

[34] H. Schomberg and J. Timmer, "The gridding method for image reconstruction by fourier transformation," *IEEE Transactions on Medical Imaging*, vol. 14, pp. 596–607, September 1995.

[35] Q. Liu and N. Nguyen, "An accurate algorithm for nonuniform fast fourier transforms (nufft's)," in *IEEE Microwave and Guided Wave Letters*, vol. 8, pp. 18–20, January 1998.

[36] B. Subiza, E. Gimeno-Nieves, J. Lopez-Sanchez, and J. Fortuny-Gausch, "An approach to sar imaging by means of non-uniform fft's," in *IEEE International Geoscience and Remote Sensing Symposium, IGARSS-03*, vol. 6, pp. 4089–4091, July 2003.

[37] N. Stacy, "Range cell migration in the spotlight sar polar format algorithm," in *IEEE International Geoscience and Remote Sensing Symposium*, vol. 5, pp. 2275–2277, July 2000.

[38] G. Lu and Z. Bao, "Compensation of scatterer migration through resolution cell in inverse synthetic aperture radar imaging," *IEE Proceedings on Radar, Sonar and Navigation*, vol. 147, pp. 80–85, April 2000.

[39] B. Rigling and R. Moses, "Taylor expansion of the differential range for monostatic sar," *IEEE Transactions on Aerospace and Electronic Systems*, vol. 41, pp. 60–64, January 2005.

[40] N. Doren, C. Jakowatz, D. Wahl, and P. Thompson, "General formulation for wavefront curvature correction in polar-formatted spotlight-mode sar images using space-variant post-filtering," in *IEEE Transactions on Image Processing*, vol. 1, pp. 861–864, October 1997.

[41] M. Preiss, D. Gray, and N. Stacy, "Space variant filtering of polar format spotlight sar images for wavefront curvature correction and interferometric processing," in *IEEE International Geoscience and Remote Sensing Symposium 2002, IGARSS '02*, vol. 1, pp. 179–181, June 2002.

[42] W. Carrara, R. Goodman, and M. Ricoy, "New algorithms for widefield sar image formation," in *Proceedings of the IEEE Radar Conference 2004*, pp. 38–43, April 2004.

[43] M. Soumekh, *Synthetic Aperture Radar Signal Processing*. John Wiley & Sons, 1999.

[44] C. Caffori, C. Prati, and E. Rocca, "Sar data focusing using seismic migration techniques," *IEEE Transactions on Aerospace and Electronic Systems*, vol. 27, pp. 194–207, March 1991.

[45] M. Soumekh, "A system model and inversion for synthetic aperture radar imaging," *IEEE Transactions on Image Processing*, vol. 1, pp. 64–76, January 1992.

[46] R. Raney, H. Runge, I. Cumming, and F. Wong, "Precision sar processing using chirp scaling," *IEEE Transactions on Geoscience and Remote Sensing*, vol. 32, pp. 786–799, July 1994.

[47] J. Bauck and W. Jenkins, "Convolution-backprojection image reconstruction for bistatic synthetic aperture radar," in *International Symposium on Circuits and Systems, ISCAS-89*, pp. 1512–1515, 1989.

[48] M. Desai and W. Jenkins, "Convolution backprojection image reconstruction for spotlight mode synthetic aperture radar," *IEEE Transactions on Image Processing*, vol. 1, pp. 505–517, October 1992.

[49] Y. Ding and D. Munson, "A fast back-projection algorithm for bistatic sar imaging," in *IEEE International Conference on Image Processing 2002*, vol. 2, pp. 449–452, September 2002.

[50] L. Ulander, H. Hellsten, and G. Stenstrom, "Synthetic-aperture radar processing using fast factorised back-projection," *IEEE Transactions on Aerospace and Electronic Systems*, vol. 39, pp. 760–776, July 2003.

[51] C. Shannon, "Communication in the presence of noise," *Proceedings of the IRE*, vol. 37, pp. 10–21, January 1949.

[52] R. Schafer and L. Rabiner, "A digital signal processing approach to interpolation," *Proceedings of the IEEE*, vol. 61, pp. 692–702, June 1973.

[53] T. Ramstad, "Digital methods for conversion between arbitrary sampling frequencies," *IEEE Transactions on Acoustics, Speech and Signal Processing*, vol. 32, pp. 577–591, June 1984.

[54] W. Brown, "Sar resolution in the presence of phase errors," *IEEE Transactions on Aerospace and Electronic Systems*, vol. 24, pp. 808–814, November 1988.

[55] N. Marechal, "High frequency phase errors in sar imagery and implications for autofocus," in *IEEE International Geoscience and Remote Sensing Symposium '96*, vol. 2, pp. 1233–1240, May 1996.

[56] T. Galloway and G. Donohoe, "Sub-aperture autofocus for synthetic aperture radar," *IEEE Transactions on Aerospace and Electronic Systems*, vol. 30, April 1994.

[57] L. Xi, L. Guosui, and J. Ni, "Autofocusing of isar images based on entropy minimisation," *IEEE Transactions on Aerospace and Electronic Systems*, vol. 35, pp. 1240–1252, October 1999.

[58] R.L. Morrison Jr and D.C. Munson Jr, "An experimental study of a new entropy-based sar autofocus technique," in *IEEE Transactions on Image Processing*, vol. 2, pp. 441–444, September 2002.

[59] J. Wang and X. Liu, "Sar minimum-entropy autofocus," in *IEEE International Radar Conference, RADAR 2004*, 2004.

[60] D. Wahl, P. Eichel, D. Ghiglia, and C.V. Jakowatz. Jr, "Phase-gradient autofocus - a robust tool for high resolution sar phase correction," *IEEE Transactions on Aerospace and Electronic Systems*, vol. 30, pp. 827–835, July 1994.

[61] D. Thompson, J. Bates, D. Arnold, and D. Long, "Range dependent phase gradient autofocus," in *IEEE International IGeoscience and Remote Sensing Symposium, (IGARSS-98)*, vol. 5, pp. 2634–2636, July 1998.

[62] M. Preiss, D. Gray, and N. Stacy, "The effect of polar format resampling on uncompensated motion phase errors and the phase gradient autofocus algorithm," in *IEEE 2001 International Geoscience and Remote Sensing Symposium, 2001 (IGARSS '01)*, vol. 3, pp. 1442–1444, July 2001 2001.

[63] C. Hain-Lim and Y. T. Soon, "Noniterative spotlight sar autofocusing using a modified phase gradient approach," in *IEEE International Geoscience and Remote Sensing Symposium, (IGARSS-97)*, vol. 1, pp. 484–486, August 1997.

[64] C. Hain-Lim and Y. T. Soon, "Non-iterative quality phase-gradient autofocus (qpga) algorithm for spotlight sar imagery," *IEEE Transactions on Geoscience and Remote Sensing*, vol. 36, pp. 1531–1539, September 1998.

[65] B. Rigling and R. Moses, "Motion measurement errors and autofocus in bistatic sar," *IEEE Transactions on Image Processing*, vol. 15, pp. 1008–1016, April 2003.

[66] T. Flynn, "Wavenumber-domain sar focusing from a nonuniform synthetic aperture," in *IEEE International Conference on Acoustics, Speech and Signal Processing, (ICASSP-92)*, vol. 3, pp. 1–4, March 1992.

[67] B. Yazici and M. Cheney, "Synthetic aperture inversion for arbitrary flight paths in the presence of noise and clutter," in *IEEE International Radar Conference, RADAR 2005*, pp. 806–810, May 2005.

[68] C.V. Jakowatz Jr and P.A. Thompson, "A new look at spotlight mode synthetic aperture radar as tomography: Imaging 3d targets," *IEEE Transactions on Image Processing*, vol. 4, pp. 699–703, May 1995.

[69] L. Novak, S. Halversen, G. Owirka, and M. Hiett, "Effects of polarisation and resolution on sar atr," *IEEE Transactions on Aerospace and Electronic Systems*, vol. 33, no. 1, pp. 102–115, 1997.

[70] R. Bamler and P. Hartl, "Synthetic aperture radar interferometry," *Inverse Problems*, vol. 14, pp. R1–54, August 1998.

[71] J. Homer, I. Longstaff, Z. She, and D. Gray, "High resolution 3-d imaging via multi-pass sar," in *IEE Proceedings on Radar, Sonar and Navigation*, pp. 45–50, February 2002.

[72] M. Richards, "A beginners guide to interferometric sar concepts and signal processing," *IEEE Aerospace and Electronic Systems Magazine*, vol. 22, pp. 5 – 29, September 2007.

[73] M. Desai, "Spotlight mode sar stereo technique for height computation," *IEEE Transactions on Image Processing*, vol. 6, pp. 1400–1411, October 1997.

[74] C.V. Jakowatz Jr, D.E. Wahl and P.A. Thompson, "Three-dimensional sar imaging using cross-track coherent stereo collections," in *Conference Record of the Thirty-First Asilomar Conference on Signals, Systems & Computers*, vol. 2, pp. 1199–1203, November 1997.

[75] O. Bezvesilny, Y. Dukhopelnykova, V. Vynogradov, and D. Varviv, "Retreiving 3d relief by using a single-antenna, squint-mode airborne sar," in *Proceedings of the 3rd European Radar Conference*, pp. 288–291, September 2006.

[76] J. Lopez-Sanchez and J. Fortuny-Guasch, "3-d radar imaging using range migration techniques," *IEEE Transactions on Antennas and Propagation*, vol. 48, pp. 728–737, May 2000.

[77] J. Fortuny-Gausch and J. Lopez-Sanchez, "Extention of the 3-d range migration algorithm to cylindrical and spherical scanning geometries," *IEEE Transactions on Antennas and Propagation*, vol. 49, pp. 1434–1444, October 2001.

[78] C. Beaudoin, A. Gatesman, R. Giles, J. Waldman, and W. Nixon, "A 3d polar processing algorithm for scale model uhf isar imaging," in *Proceedings of SPIE - The International Society for Optical Engineering - Algorithms for Synthetic Aperture Radar Imagery XIII*, vol. 6237, April 2006.

[79] J. Burki and C. Barnes, "Sar with two-dimensional aperture synthesis," in *IEEE Radar Conference RADAR 2007*, pp. 590–595, April 2007.

[80] F. Meglio, G. Panariello, and G. Schirinzi, "Three dimensional sar image focusing from non-uniform samples," in *IEEE International Geoscience and Remote Sensing Symposium*, pp. 528–531, 2007.

[81] M. Weiß, and J.H.G. Ender, "A 3d imaging radar for small unmanned airplanes - artino," in *European Radar Conference 2005, EURAD 2005*, pp. 45–48, October 2005.

[82] J. Klare, M. Weiß, O. Peters, A.R. Brenner, and J.H.G. Ender, "Artino: a new high resolution 3d imaging radar system on an autonomous airborne platform," in *IEEE International Geoscience and Remote Sensing Symposium 2006, IGARSS 2006*, pp. 3842 – 3845, July 2006.

[83] K. Knaell, "Three-dimensional sar from curvilinear apertures," in *Proceedings of the 1996 IEEE National Radar Conference 1996*, pp. 220–225, May 1996.

[84] M. Soumekh, "Reconnaissance with slant place circular sar imaging," *IEEE Transactions on Image Processing*, vol. 5, pp. 1252–1265, August 1996.

[85] J. Li, Z. Bi, Z. Liu, and K. Knaell, "Use of curvilinear sar for three-dimensional target feature extraction," *IEE Proceedings on Radar, Sonar and Navigation*, vol. 144, pp. 275–283, October 1997.

[86] Z. Su, Y. Peng, and X. Wang, "Non-iterative imaging algorithm for clsar," in *Proceedings IEEE International Conference on Acoustics, Speech, and Signal Processing (ICASSP '05)*, vol. 2, pp. 577–580, March 2005.

[87] Z. Su, Y. Peng, and X. Wang, "Fast non-iterative algorithm for clsar," in *IEEE International Radar Conference 2005, RADAR 2005*, pp. 778–782, May 2005.

[88] Z. Su, Y. Peng, and Z. Wang, "Three-dimensional target features extraction method in curvilinear sar with aperture errors," in *IEEE International Symposium on Communications and Information Technology, ISCIT 2005*, vol. 2, pp. 1227–1230, October 2005.

[89] Z. Su, G. Liu, Y. Peng, R. Wu and R. Liu, "Rcb-based imaging method for 3d target via curvilinear sar," in *9th International Conference on Signal Processing, ICSP 2008*, pp. 2638 – 2371, October 2008.

[90] Z. Su, Y. Peng, and X. Wang, "Feature-independent aperture evaluator for curvilinear sar," *IEEE Geoscience and Remote Sensing Letters*, vol. 4, pp. 191–195, April 2007.

[91] C. Austin and R. Moses, "Wide-angle sparse 3d synthetic aperture radar imaging for nonlinear flight paths," in *IEEE National Aerospace and Electronics Conference 2008, NAECON 2008*, pp. 330 – 336, July 2008.

[92] L. Xiangle and Y. Ruliang, "Study of composite mode curvilinear sar," in *International Conference on Radar 2006, CIE 2006*, pp. 1 – 4, October 2006.

Appendix A
Binomial expansion of differential range term

From chapter 2 the differential range term is approximated using a binomial expansion where l_1 and l_0 are given by

$$\begin{aligned} l_1 &= r_t + r_r \\ l_0 &= r_{0t} + r_{0r} \end{aligned}$$

where

$$\begin{aligned} r_t &= |\mathbf{x}_t - \mathbf{r}_n| \\ r_r &= |\mathbf{x}_r - \mathbf{r}_n| \end{aligned}$$

and

$$\begin{aligned} r_t &= |\mathbf{x}_t| \\ r_r &= |\mathbf{x}_r| \end{aligned}$$

where $\mathbf{x}_t$ and $\mathbf{x}_r$ are the position vectors for the transmitter and receiver platforms respectively and $\mathbf{r}_n$ is the position vector of the nth scatterer in the scene of interest.

Therefore the differential range term can be written as

$$\begin{aligned} l_1 - l_0 &= (r_t + r_r) - (r_{0t} + r_{0r}) \\ &= (r_t - r_{0t}) + (r_r - r_{0r}) \\ &= (|\mathbf{x}_t - \mathbf{r}_n| - |\mathbf{x}_t|) + (|\mathbf{x}_r - \mathbf{r}_n| - |\mathbf{x}_r|) \end{aligned} \tag{A.1}$$

considering the first term of equation (A.1) for simplicity, performing a binomial expansion

gives

$$\begin{aligned}(|\mathbf{x}_t - \mathbf{r}_n| - |\mathbf{x}_t|) &= \sqrt{(\mathbf{x}_t - \mathbf{r}_n)^2} - \sqrt{\mathbf{x}_t^2} \\ &= \sqrt{\mathbf{x}_t^2 - 2\mathbf{x}_t\mathbf{r}_n + \mathbf{r}_n^2} - \sqrt{\mathbf{x}_t^2} \\ &= |\mathbf{x}_t|\sqrt{1 - \frac{2\mathbf{x}_t\mathbf{r}_n}{|\mathbf{x}_t^2|} + \frac{\mathbf{r}_n^2}{|\mathbf{x}_t^2|}} - \sqrt{\mathbf{x}_t^2} \\ &= |\mathbf{x}_t|\left(1 + \frac{1}{2}\left(\frac{2\mathbf{x}_t\mathbf{r}_n}{|\mathbf{x}_t^2|} + \frac{\mathbf{r}_n^2}{|\mathbf{x}_t^2|}\right) + \left(\frac{\left(\frac{1}{2}\right)\left(\frac{-1}{2}\right)}{2}\frac{\mathbf{r}_n^2}{|\mathbf{x}_t^2|}\right)\right) \\ &\quad -\sqrt{\mathbf{x}_t^2} \end{aligned} \tag{A.2}$$

plus higher order terms. Therefore retaining only the linear terms in this expansion

$$(|\mathbf{x}_t - r_n| - |\mathbf{x}_t|) = \frac{\mathbf{x}_t\mathbf{r}_n}{|\mathbf{x}_t|} \tag{A.3}$$

similarly for the receiver platform

$$(|\mathbf{x}_r - r_n| - |\mathbf{x}_r|) = \frac{\mathbf{x}_r\mathbf{r}_n}{|\mathbf{x}_r|} \tag{A.4}$$

Therefore the differential range term can be approximated as follows

$$\begin{aligned} l_1 - l_0 &\approx \frac{(\mathbf{x}_t + \mathbf{x}_r)\,\mathbf{r}_n}{|\mathbf{x}_t| + |\mathbf{x}_r|} \\ &= \frac{(\mathbf{x}_t + \mathbf{x}_r)\,\mathbf{r}_n}{l_0} \end{aligned} \tag{A.5}$$

Appendix B
Original Publications

The following original publications relating to this work are reprinted as an appendix

- G. Halcrow and B. Mulgrew, "Nonlinear k-space mapping method for SAR Fourier imaging", *IEEE radar conference, RADAR 2006*, pp. 384-387, April 2006.
- G. Halcrow and B. Mulgrew, "SAR 3D Scene Reconstruction Using Fourier Imaging Techniques", *The Institution of Engineering and Technology Seminar on High Resolution Imaging and Target Classification 2006* , pp. 53-60, November 2006.

Nonlinear k-Space Mapping Method for SAR Fourier Imaging

Gavin Halcrow and Bernard Mulgrew
Institute for Digital Communications
School of Engineering and Electronics, The University of Edinburgh
Edinburgh, United Kingdom
Email: g.i.halcrow@sms.ed.ac.uk

Abstract— **A method for nonlinear mapping of k-space amples to facilitate the two-dimensional irregular to regular esampling required by the polar format algorithm (PFA) is resented. Mapping the locations of the collected k-space amples to a uniform rectangular grid and desired locations overing the data region, the interpolation becomes separable in two-dimensions. Resulting PFA images require no rther processing to be displayed in the global X, Y coordinates and use all the collected data. This method of esampling allows PFA image formation from bistatic synthetic aperture radar (SAR) and also data collected from regular flight paths.**

I. Introduction

In Synthetic Aperture Radar (SAR) imaging a moving adar antenna follows a given flight path, emitting pulses f electromagnetic (EM) radiation. The EM pulses are ollected by the antenna after scattering off the terrain nd objects within a scene. The collected signals can be rocessed using signal processing techniques to form an nage of the scene. Fourier imaging provides a method f forming SAR images from collected radar data which oes not demand the same computational load associated ith other imaging methods such as matched filtering and onvolution-back projection [1][2][3]. In particular the polar format algorithm (PFA) provides a simple framework or image formation for spotlight SAR, limited however by he plane wave approximation.

There has been an increase in research in the area of istatic SAR [4][5], where the transmit and receive antenna re on separate platforms, typically with the transmitting latform at a large stand-off range. This increase in interest in bistatic SAR is primarily due to the increased urvivability of the receive platform, which is harder to detect due to it's passive role in the imaging operation. In his mode of operation the locations of the collected phase istory samples in k-space make the two-dimensional interolation required for the PFA image formation more challenging than in the traditional monostatic SAR case.

n addition to this the restriction in existing PFA algorithms that the receiver should fly a straight and level flight ath means that while imaging, aircraft are unable to perorm any evasive maneuvers. If this restriction could be emoved then the survivability of the receiving platform ould be further increased.

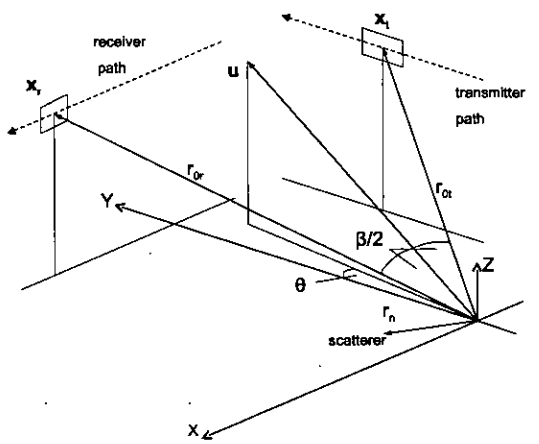

Fig. 1. Bistatic SAR system geometry

II. System Geometry

For the bistatic operation the collected radar signal, used to form the SAR image, is given by [6];

$$s(t,\widehat{t}) = \sum_{n=1}^{N} A(n) e^{-j\phi(n,t,\widehat{t})} \tag{1}$$

where;

$$\phi(n,t,\widehat{t}) = \omega(t,\widehat{t})\mathbf{x(n)} \tag{2}$$

and

$$\omega(t,\widehat{t}) = \frac{2}{c}\left[\omega_0 + 2\alpha\left(\widehat{t} - \left(\frac{r_{0t}(t) + r_{0r}(t)}{c}\right)\right)\right] \tag{3}$$

Where there are N scatterers in the scene, A is the complex reflectivity of the target, $\boldsymbol{x(n)}$ is the displacement of the scatter from the scene centre, t is slow time, $\widehat{t}$ is the fast time, ω_0 is the radar centre frequency and α is the chirp rate, $r_{0t}(t)$ is the distance from the transmit platform to the scene centre, r_{0r} is the distance from the receive platform to the scene centre and c is the speed of light, as shown in Fig. 1.

The samples of this function are located in k-space on a distorted polar raster given by;

$$\mathbf{k} = \omega\left(\frac{\widehat{\mathbf{u}}_\mathbf{T} + \widehat{\mathbf{u}}_\mathbf{R}}{\mathbf{2}}\right) \tag{4}$$

$$\mathbf{k} = \omega\mathbf{u} \tag{5}$$

$$\mathbf{k} = \omega|\mathbf{u}|\widehat{\mathbf{u}} \tag{6}$$

where $\widehat{\mathbf{u}}_T$ is the unit vector in the direction of the transmit platform, $\widehat{\mathbf{u}}_R$ is the unit vector in the direction of the receive platform and $\mathbf{u}$ is the bistatic look vector. Therefore $\widehat{\mathbf{u}}$ is a function of the bistatic look direction, θ given by half the bistatic angle, β.

$$\widehat{\mathbf{u}} = \begin{bmatrix} cos\theta \\ sin\theta \end{bmatrix} \tag{7}$$

PFA imaging requires the phase history data to be resampled from the distorted polar raster onto a uniform rectangular grid, to allow use of the fast Fourier transform (FFT) for the image formation. It has been demonstrated that in the case of bistatic operation better use of the data can be achieved by interpolating to a parallelogram grid rotated by the apparent look direction given by half the bistatic angle [8]. Interpolating to this parallelogram grid allows more of the phase history data to be used in the FFT and retains the fast and slow time identities in the interpolated data. This allows use of the many autofocus algorithms developed for use in monostatic SAR, for example the Phase Gradient Algorithm[7], on bistatic SAR images. However this means that the resulting image needs to be rotated and de-skewed to achieve an image in the global X,Y coordinate set. The proposed method aims to simplify the interpolation process allowing resampling from any set of k-space sample positions to a regular rectangular region that fully encompasses the data.

III. Mapping

To be more explicit the k_x and k_y sample location is given by;

$$\mathbf{k} = \begin{bmatrix} k_x \\ k_y \end{bmatrix} = \omega_j|\mathbf{u}(\theta_i)|\widehat{\mathbf{u}}(\theta_i) \tag{8}$$

where the subscript i indicates the pulse number and the subscript j indicates the frequency sample number. Then the integer pair $[i,j]$ defines a uniform rectangular grid. Equation (8) provides a nonlinear function mapping points on the uniform grid at $[i,j]$ to points in k-space $[k_x,k_y]$, on the distorted polar raster. To form images using the FFT we need to map points on the non-uniform grid in k-space onto the space defined by $[i,j]$, therefore we need to invert the nonlinear mapping function given in (8).

$$\mathbf{k} = f\left(\begin{bmatrix} i \\ j \end{bmatrix}\right) \tag{9}$$

$$\begin{bmatrix} i \\ j \end{bmatrix} = f^{-1}(\mathbf{k}) \tag{10}$$

In some cases, with simple geometry, this mapping function can be inverted to provide a new mapping function that can be used to map the polar raster to a uniform rectangular grid and for the desired rectangular grid to be mapped to the same space. However for complicated flight paths this analytic inversion is not always achievable, but in these cases the inversion can be performed by way of utilizing the intermediate function θ.

$$\theta(t) = tan^{-1}\left(\frac{\widehat{u}_x(t)}{\widehat{u}_y(t)}\right) = tan^{-1}\left(\frac{k_x}{k_y}\right) \tag{11}$$

Where $\widehat{u}_x(t)$ is the x-component of the bistatic look vector and $\widehat{u}_y(t)$ is the y-component of the bistatic look vector. θ provides the mapping from k_x, k_y to pulse number for the original sample locations, if this function is upsampled then it can also be used to perform the mapping operation for the desired sample locations, giving the non-integer pulse number i, for the desired sample locations. The same operation of upsampling the data and interpolating gives the value of the functions $|\mathbf{u}(\theta_i)|$ and $\widehat{\mathbf{u}}(\theta_i)$ for the non-integer values of i. Now using these values;

$$\omega_j = \frac{|\mathbf{k}|}{|\mathbf{u}(\theta_i|} \tag{12}$$

Giving the non-integer frequency sample number j, for the desired sample locations. At this point the mapping is complete and the interpolation can be performed.

IV. Motivation

Interpolation by this method has many advantages; the interpolation function is identical at each sample position unlike on the original irregular sample grid. The interpolation function goes to zero at each of the other original sample positions. The two-dimensional interpolation separates exactly into two one-dimensional interpolation operations and also windowing can be applied in two one dimensional directions, where the window fits the data region exactly. Testing for interpolation points outside of the data region is trivial when the data lies on a uniform rectangular grid. Once the interpolation has been performed in the mapped space, the resampled data is processed as normal using the PFA. The resulting image requires no further processing to be displayed in the global X,Y coordinates, because of the chosen desired grid.

In addition to providing a simple framework for the interpolation required for the PFA, the proposed method also allows interpolation of data on grids which cannot even locally be considered regular. This provides imaging aircraft the opportunity to deviate from the standard straight and level flight path normally required for SAR imaging. Since deviation from this path simply changes the k-space sample density in the PFA. This method could also provide some ability to perform deliberate irregular sampling by alteration of the pulse repetition frequency as well as interrupted SAR, forming images from non-continuous radar data sets.

V. Simulation

The proposed mapping method has been simulated using a discrete point scatterer model in MATLAB. To allow a simple parameter to be used to determine the irregularity of the collected samples on the distorted polar raster, the simulations performed included only accelerating platforms following linear flight paths. However this is by no means the only maneuver that can be simulated. Expressing the start point, radius and accelerations involved in

ven simple circular turns seems unnecessary when the effect on cross range sample density is determined by the long track motion of the platform.

. *Monostatic Operation*

The first simulated case is of an X-band monostatic SAR ystem with approximately $0.25m$ resolution. The radar latform follows a typical broadside path at $15km$ stand-ff range, with the exception that the platform accelerates long this path at $15ms^{-2}$. This acceleration changes the ollected phase history sample density in k-space. The col-ected sample positions in k-space and the desired regular ectangular sample grid that encompasses the entire data egion are shown in Fig. 2(a). The desired grid is obtained y estimating the highest sample density in the collected ata, to determine the highest frequency supported by the ata, and evaluating the extent of the data region in the k_x nd k_y directions. The mapping method described in the revious section was performed. Then the interpolation as performed by summing the result of placing a scaled $inc(x)$ interpolation function with a limited length on each f the known sample positions, then applying a window to he data in two dimensions. This process allows the value f the underlying function to be evaluated at any chosen oint in the two-dimensional space, which for the PFA are he mapped desired sample points. Finally the data was ransformed using one-dimensional FFTs in the k_x and k_y irections.

The resulting image is shown in Fig. 2(c). For compar-son the PFA was implemented using the keystone inter-olation method on the same collected data, the resulting mage is shown in Fig. 2(b). where both figures show image ntensity on a logarithmic scale.

3. *Bistatic Operation*

The second simulated case is of the same X-band SAR ystem however this time operating in a bistatic configu-ation, with the transmitter at $15km$ stand-off range. The eceiver moves on a linear path and accelerates along this irection at $15ms^{-2}$, the bistatic angle, β is approximately 0^o. The collected sample positions in k-space and the de-ired regular rectangular sample grid that encompasses the ntire data region are shown in Fig. 3(a), where the de-ired grid is obtained by the same method. The mapping ethod and interpolation were performed as before. The esulting image is shown in Fig. 3(c), note that no rotation r further processing was required to form the image in the lobal coordinate set. For comparison the bistatic PFA was mplemented using the keystone interpolation method on he same collected data, the resulting image is shown in ig. 3(b).

VI. Analysis

The image formed using the proposed mapping method n the monostatic simulation shows the improved focus of he simple point scatterers across the entire scene that is ypical of the PFA. The level of the scatterer sidelobes is een to be significantly lower when compared to the image

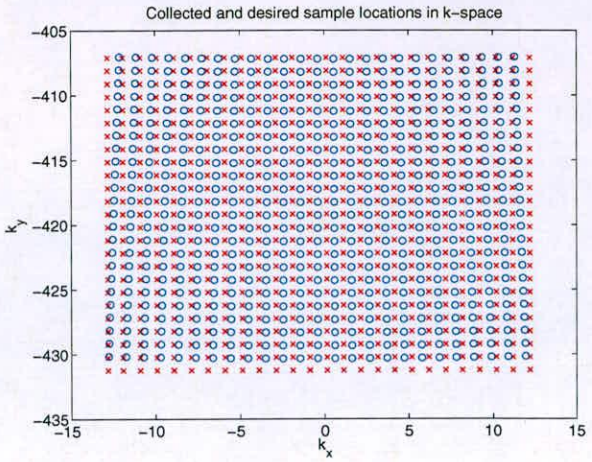

(a) k-space sample locations

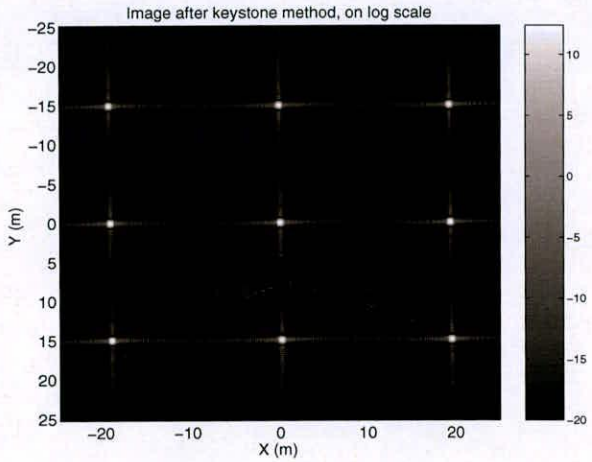

(b) Keystone interpolation image

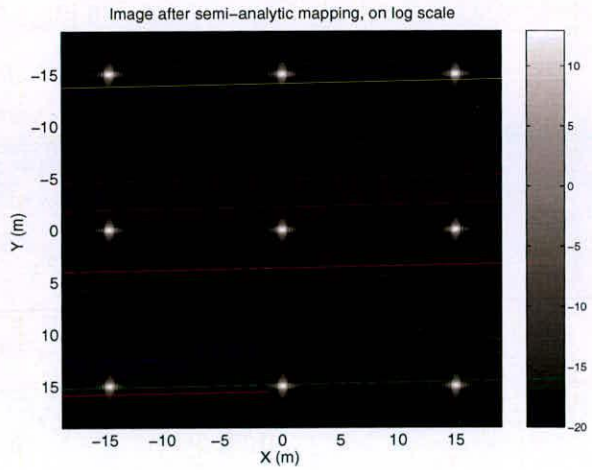

(c) Mapping method image

Fig. 2. Monostatic simulation results

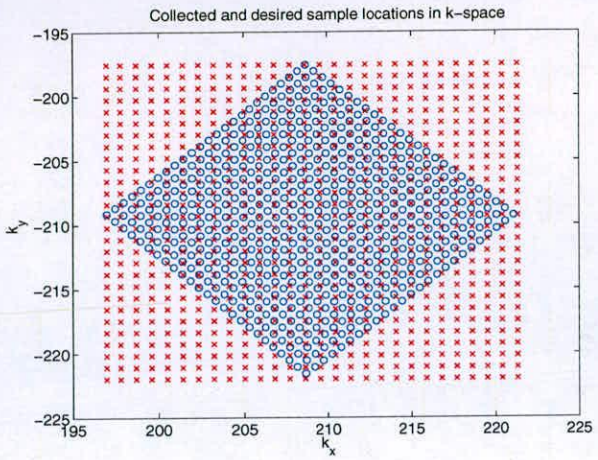

(a) k-space sample locations

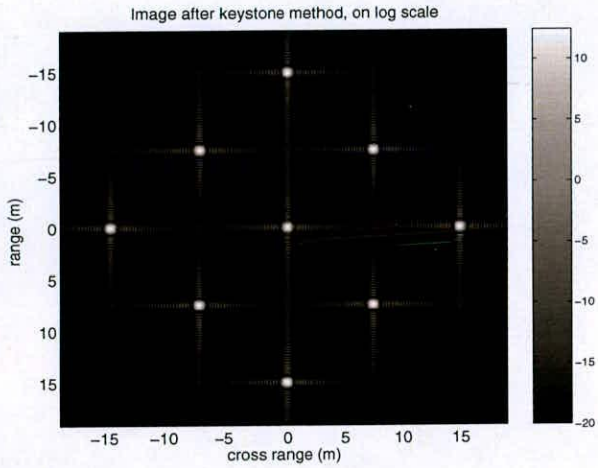

(b) Keystone interpolation image

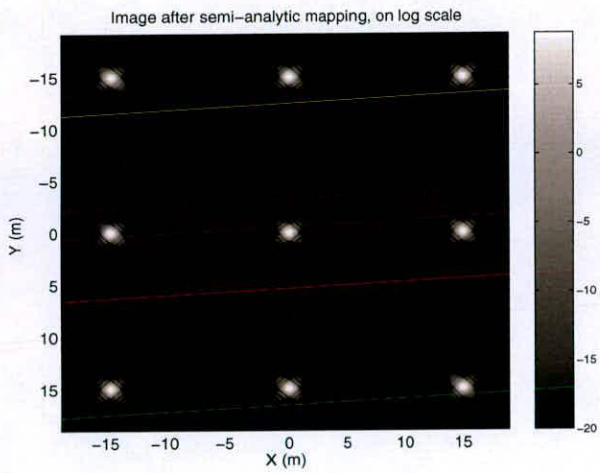

(c) Mapping method image

Fig. 3. Bistatic simulation results

formed using the keystone interpolation method. Using the mapping method the level of the sidelobes is approximately 7dB lower than when using the keystone interpolation method, this performance allows the observation of low reflectivity scatterers in more complicated scenes, where otherwise these scatterers would be obscured.

The image formed using the keystone interpolation method in the bistatic configuration again shows the same sidelobe performance, and the image still requires rotation by the bistatic look angle and lastly a de-skewing of the image is necessary to get a geometrically correct image. However the image formed by the mapping method shows the same performance as in the monostatic simualtion and the image requires no further processing.

VII. Conclusion

This paper has shown that by inverting the mapping function necessary to obtain the distorted polar raster sample positions in the PFA, the collected and desired sample locations necessary to use the FFT can be mapped to a space where the two-dimensional resampling operation becomes simpler. The same interpolation function can be used at all sample points, also windowing and interpolation become separable into two one-dimensional operations. In addition the proposed method allows resampling of irregularly sampled data collected by maneuvering SAR platforms, and other modes of SAR operation. By means of simulation the performance of the proposed mapping method has been demonstrated. When compared to the keystone interpolation method within the PFA, for monostatic and bistatic operations the proposed algorithm shows improved image quality.

Acknowledgment

The authors would like to thank the support of BAE Systems and SELEX Sensors and Airborne Systems Ltd for this work.

References

[1] C.V. Jakowatz, D.E. Wahl, D.C. Ghiglia and P.A. Thompson, *Spotlight-mode Synthetic Aperture Radar: a Signal Processing Approach*, (Kluwer Academic Publishers, 1996)

[2] W.C. Carrara, R.G. Goodman and R.M. Majewski, *Spotlight Synthetic Aperture Radar: Signal Processing Algorithms*, Artech House, Boston 1995

[3] Mita D. Desa and W. Kenneth Jenkins, "Convolution Backprojection Image Reconstruction, for Spotlight Mode Synthetic Aperture Radar", IEEE Transactions on Image Processing, Vol. 1, No. 4, October 1992, pp 505-517

[4] A.M. Horne and G. Yates, "Bistatic Synthetic Aperture Radar", Radar 2002, October 2002, pp 6-10

[5] M. Soumekh, "Bistatic Synthetic Aperture Radar Inversion with Application in Dynamic Object Imaging", IEEE Transactions on Signal Processing, Vol. 39, No. 9, September 1991, pp 2044-2055

[6] M. Lowe, "Algorithms for High Resolution Bistatic SAR", RADAR 2002, Oct.2002, pp 512-515

[7] D.E. Wahl, P.H. Eichel, D.C. Ghiglia and C.V. Jakowatz Jr., "Phase Gradient Autofocus a Robust Tool for High Resolution SAR Phase Correction", IEEE Transactions on Aerospace and Electronic Systems, Vol. 30, No. 3, July 1994, pp 827-835

[8] B.D. Rigling and R.L. Moses, "Polar Format Algorithm for Bistatic SAR", IEEE Transactions on Aerospace and Electronic Systems, Vol.40, Issue 4, Oct. 2004, pp 1147-1159

3D SAR Scene Reconstruction Using Fourier Imaging Techniques

G. Halcrow*, B. Mulgrew

*The University of Edinburgh
Institute for Digital Communications
School of Engineering and Electronics, The University of Edinburgh
Edinburgh, United Kingdom
email: G.I.Halcrow@ed.ac.uk

Keywords: Synthetic Aperture Radar, Fourier Imaging

Abstract

If a nonlinear 3D flight path is followed instead of the typical linear path, for spotlight SAR. The sampled area of k-space obtained is a curved 2D surface in 3D space. Since this surface has extent in all three dimensions, 3D scene reconstruction is possible. This can be performed using convolution back-projection, however due to the extra dimension this is computationally intensive. A method to allow use of the computationally efficient FFT for image formation is presented. By performing a mapping operation to a domain where the interpolation becomes a simpler operation, resampling the data to points on a uniform cube grid allows use of the FFT. Off-surface interpolation is possible due to the shape of the sampled area of k-space. Simulation results are presented to demonstrate the algorithm.

1 Introduction

Spotlight synthetic aperture radar (SAR) images are typically formed from data collected from aircraft following linear constant altitude flight paths. As a result of the chosen flight path the sampled area of frequency or k-space obtained is a 2D plane in 3D space, the 3D information content of the scene projects onto this plane and since it has no extent in the k_z direction altitude information about the scene of interest is lost. The 2D plane is projected onto the ground plane for imaging to form a normal 2D image of the scene of interest.

The properties of the image formed are determined by the sampled area of k-space, the extent of the data in each direction in k-space determines the achievable resolution, and the sample density determines the maximum image size. With these conditions in mind the ideal sampled area of k-space for 3D image formation would be a cube of data, this would allow for good resolution, image size and scatterer point spread function. However collection of this volume of data is impractical and other methods must be used to determine information about the volume of data to allow 3D image formation.

A conventional method of forming a 3D image of a scene is by interferometric SAR (IFSAR). In IFSAR imaging, two independent SAR data sets are used to form two separate 2D images from which a phase difference can be evaluated, this phase difference term can be used to determine the elevation of the features in the 2D images and can be used to form a 3D image of the target scene [2].

By collecting data from a nonlinear 3D flight path the sampled area of k-space becomes a 2D surface instead of a plane, with extent in all three dimensions. From this type of curved surface the 3D information about the scene of interest is retained allowing 3D image formation. In the literature covering 3D imaging of this kind, the image processing has concentrated on the use of convolution back-projection (CBP) methods [3,4]. These imaging algorithms are known to scale poorly with image size, given the extra dimension involved an alternative method is sought. The purpose of this paper is to present a method for 3D image formation using Fourier imaging techniques.

2 System Geometry

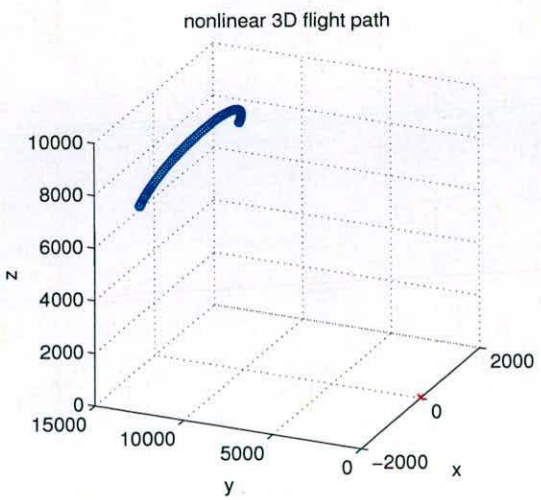

Figure 1: Nonlinear 3D flight path.

For monostatic operation the collected radar signal used to form the SAR image is given by[2];

$$s(t,\hat{t}) = \sum_{n=1}^{N} A(n) e^{-j\phi(n,t,\hat{t})} \quad (1)$$

where;

$$\phi(n,t,\hat{t}) = \omega(t,\hat{t})\mathbf{x}(n) \quad (2)$$

and;

$$\omega(t,\hat{t}) = \frac{2}{c}\left[\omega_0 + 2\alpha\left(\hat{t} - \left(\frac{2r_0(t)}{c}\right)\right)\right] \quad (3)$$

Where there are N scatterers in the scene, A is the complex reflectivity of the target, $\mathbf{x}(n)$ is the displacement of the scatterer from the scene centre, t is slow time, $\hat{t}$ is fast time, ω_0 is the radar centre frequency and α is the chirp rate, $r_0(t)$ is the distance from the platform to the scene centre and c is the speed of light.

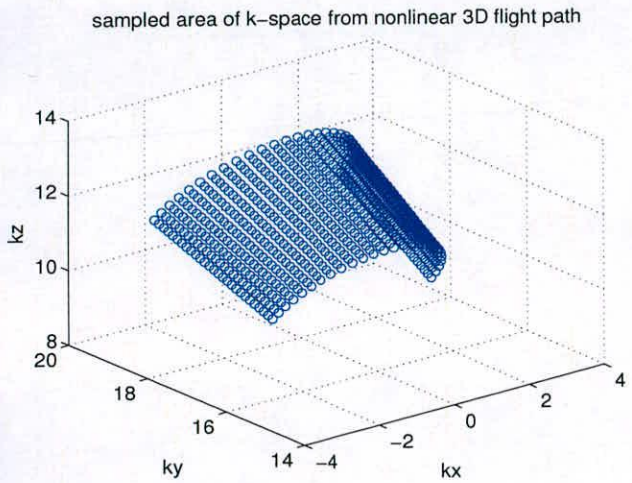

Figure 2: Sampled area of k-space obtained using nonlinear 3D flight path.

The samples of this function are located in k-space on a distorted polar raster, as shown in Figure 2, given by;

$$\mathbf{k} = \omega\mathbf{u} \quad (4)$$

where;

$$\mathbf{k} = \begin{bmatrix}\mathbf{k}_x & \mathbf{k}_y & \mathbf{k}_z\end{bmatrix}^T \quad (5)$$

where $\mathbf{u}$ is the vector in the direction of the platform, therefore $\mathbf{u}$ is a function of the look direction, θ, and the slant angle, ψ.

$$\mathbf{u} = \begin{bmatrix}\sin\theta\cos\psi \\ \cos\theta\cos\psi \\ \sin\psi\end{bmatrix} \quad (6)$$

3 Method

As stated previously coverage in the literature concentrates on image formation using CBP, however computationally this algorithm scales with the target scene size. For scene size D, when working in 3D imaging the scene size is increased from D^2 to D^3 due to the extra dimension. This places a significant limit on the size of scenes that can be imaged using 3D SAR based on the CBP algorithm.

Instead of using CBP for image formation the image formation method used in this paper is based on the polar format algorithm (PFA). Using the PFA image formation is performed using the fast Fourier transform (FFT), however in order to make use of the computationally efficient FFT the collected data needs to be resampled. In 2D the collected data is resampled onto a uniform rectangular grid, therefore in the 3D case the data needs to be resampled onto a uniform cube grid of points.

The method used to perform this 3D resampling operation is based on the method in [1]. The 2D surface of sampled data will be mapped to a 2D plane of uniformly spaced points, a desired cube grid of points surrounding the data will also be mapped to the same domain.

$$\mathbf{k}' = f(\mathbf{k}) \quad (7)$$

where;

$$\mathbf{k}' = \begin{bmatrix}\mathbf{k}'_x & \mathbf{k}'_y & \mathbf{k}'_z\end{bmatrix}^T \quad (8)$$

the target grid $\mathbf{k}'$ is chosen to be uniform and integer spaced for convenience.

After an initial linear affine mapping, a Volterra series is used to perform the mapping operation.

$$\begin{aligned}\mathbf{k}'_x &= a + a_0k_x + a_1k_y + a_2k_z + a_{00}k_x^2 + a_{01}k_y^2 \\ &+ a_{02}k_z^2 + a_{10}k_xk_y + a_{11}k_xk_z + a_{12}k_yk_z \ldots\end{aligned} \quad (7)$$

which can be written as a matrix equation;

$$\mathbf{k}' = \mathbf{K}\mathbf{a} \quad (8)$$

which has a least squares solution;

$$\mathbf{a} = \left[\mathbf{K}^T\mathbf{K}\right]^T\mathbf{K}^T\mathbf{k}'_x \quad (9)$$

Performing the resampling in this domain has many advantages; the interpolation function is identical at each sample position unlike on the original irregular sample grid. The interpolation function goes to zero at each of the other original sample positions. The 3D interpolation separates exactly into three 1D interpolation operations and also windowing can be applied in three 1D directions. Once the interpolation has been performed in the mapped space, the resampled data is processed as normal using the PFA to form a 3D image of the scene of interest.

4 Simulation Details

The mapping method described has been simulated using a discrete point scatterer based model in MATLAB. The simulated system has approximately 1m resolution in each

direction, imaging a scene 80m in each direction, with 1 GHz radar centre frequency and 0.15 MHz bandwidth. The simulation was performed to demonstrate the ability to form a 3D image from two different data surfaces, firstly from an orthogonal data surface and then from a curved data surface obtained from a nonlinear flight path.

4.1 Orthogonal Aperture

As collection of a cube of data in k-space is impractical the natural choice for a data surface would have the same extent in each direction, this can be achieved with an orthogonal data surface. The surface is essentially three sides of the ideal cube of data. The orthogonal aperture should allow good resolution and image extent in all three dimensions.

In order for fair comparison between images formed from data collected from a nonlinear flight path, like the one shown in Figure 1 the orthogonal aperture is selected to have nominally the same extent in each dimension as the sampled area of k-space shown in Figure 2. This is determined simply by projecting the curved aperture onto each of the x-y, x-z and y-z planes. The orthogonal aperture used is shown in Figure 3.

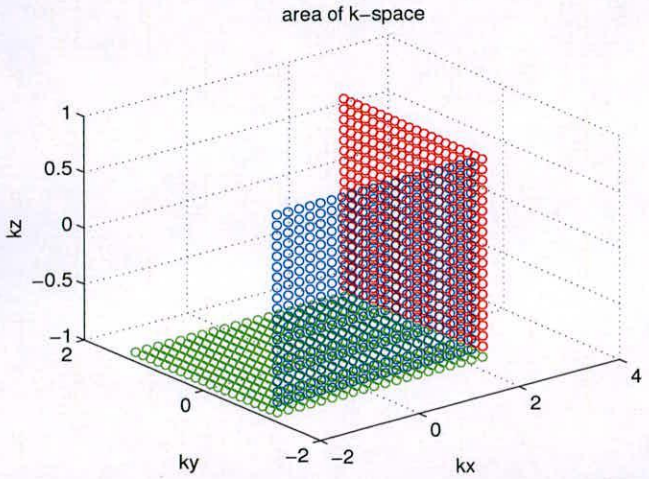

Figure 3: Orthogonal aperture sampled area of k-space.

The values of the data on the surface are determined by;

$$s(t,\hat{t}) = \mathbf{k}.\mathbf{x} \qquad (7)$$

For image formation these samples are then loaded into a matrix of zeros and Fourier transformed in all three dimensions using the FFT. The resulting image is shown in Figure 4.

4.1 Nonlinear 3D Flight Path

The simulation was performed using the monostatic flight path shown in Figure 1 this gives the sampled area of k-space shown in Figure 2. The extent of the surface was determined and the maximum sample density in each dimension estimated, these parameters were used to determine the desired cube grid of points to which resampling was performed, as is shown in Figure 5.

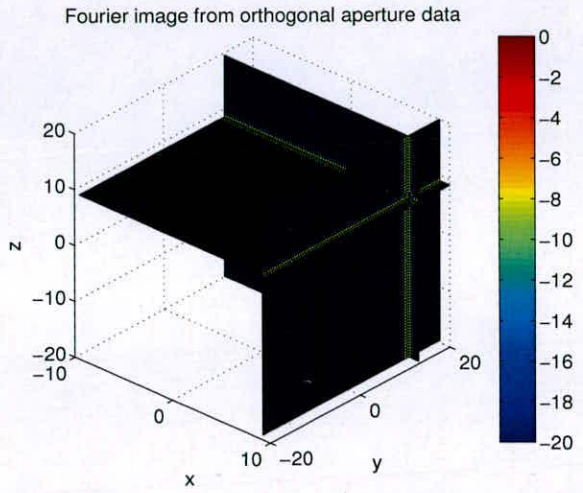

Figure 4: Result of image formation from orthogonal aperture using FFT.

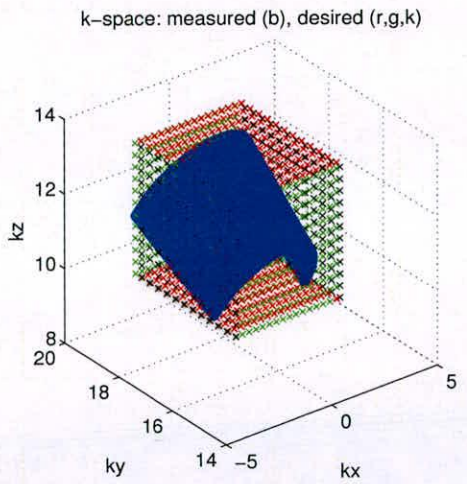

Figure 5: Sampled area of k-space, and desired sample grid. Red sample points show the top and bottom surface of the desired sample grid, with green and black showing opposite sides of the cube grid.

The affine and Volterra mapping stages were applied to the known data points to determine the mapping coefficients used to move from the data collection domain, to the domain in which the sampled data lies on a integer surface in the x-y plane. These mapping coefficients were then applied to the desired cube of points to bring them to the same domain. The result of the mapping operation is shown in Figure 6.

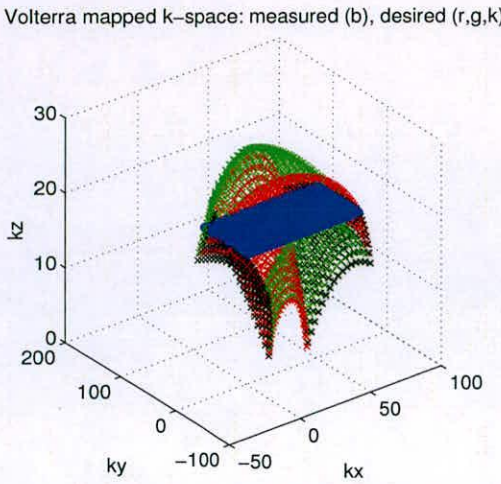

Figure 6: Sampled area of k-space, and desired sample grid after affine and Volterra mapping stages. Red, green and black points show distortion of the desired cube grid.

In this space the interpolation is performed by evaluating the sum of *sinc(x)* functions in each direction, scaled by the value of the sampled data at a given point. This interpolation is only performed for sample points close to the data surface, all other points are assumed to be zero valued. No windowing has been applied to the data before or after interpolation. The resampled data is then Fourier transformed in all three dimensions using the FFT. The result of this image formation process is shown in Figure 7.

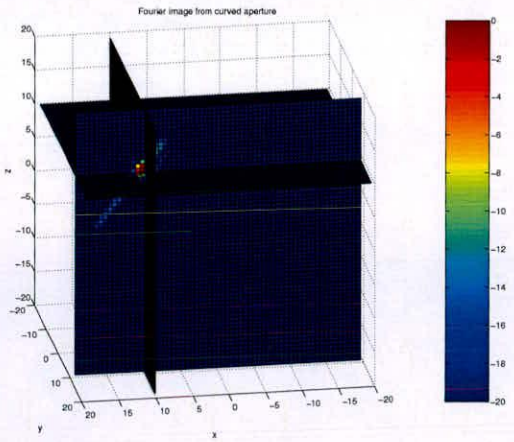

Figure 7: Result of image formation by FFT after Volterra mapping based resampling operation. Value of data is shown at slices through the 3D volume of data.

5 Analysis

The result of image formation from the orthogonal aperture, shown in Figure 4 shows that 3D image formation using the FFT is possible, when only a data surface is available instead of the whole volume. The point spread function of the scatterer in the scene is roughly a *sinc(x)* function, due to the square surfaces of the aperture. However the scatterer in the image does have very high sidelobes, this is a consequence of not having the full volume of data available.

The result of image formation from the curved data surface produced by a nonlinear flight path shows that the off-surface interpolation performed using the Volterra mapping method is interpolation and not extrapolation. The scatterer is located correctly in the 3D image and although the point spread function is irregular this is due to the shape of the sampled data surface.

6 Conclusions

The simulation results from using the Volterra mapping method to interpolate off the sampled data surface from a 3D nonlinear flight path show that interpolation in this way is possible. This method allows interpolation to be performed off the sampled data surface in an attempt to evaluate the function at some of the uniform cube grid points closest to the surface.

This interpolation is only possible due to the curved nature of the data surface. The curvature means that more information about the full volume of data is retained than just a simple slice through it. This enables 3D images to be formed using the computationally efficient FFT, rather than having to use the CBP algorithm.

Acknowledgements

The authors would like to thank the support of BAE Systems and SELEX Sensors and Airborne Systems Ltd for this work.

References

[1] G. Halcrow and B. Mulgrew, "Nonlinear k-Space Mapping Method for SAR Fourier Imaging", IEEE RADAR 2006 Conference, (April 2006).

[2] C.V. Jakowatz, D.E. Wahl, D.C. Ghiglia and P.A. Thompson, *Spotlight-mode Synthetic Aperture Radar: a Signal Processing Approach*, Kluwer Academic Publishers, (1996).

[3] J. Li, Z. Bi, Z.S. Liu and K. Knaell; "Use of Curvilinear SAR for Three-Dimensional Target Feature Extraction", *IEE Proceedings on Radar, Sonar and Navigation.*, Vol. 144, Issue 5, (October 1997).

[4] B.D. Rigling and R.L. Moses, "Flight Path Strategies for 3D Scene Reconstruction From Bistatic SAR", *IEE Proceedings on Radar, Sonar and Navigation,* Vol. 151, No. 3, pp 149-157, (June 2004).